PHYSIK - DEPARTMENT

The neutrinoless double beta decay experiment GERDA Phase II: A novel ultra-low background contacting technique for germanium detectors and first background data

DISSERTATION
VON

TOBIAS BODE

TECHNISCHE UNIVERSITÄT
MÜNCHEN

TECHNISCHE UNIVERSITÄT MÜNCHEN
Physik-Department
Lehrstuhl für Experimentalphysik und Astroteilchenphysik

The neutrinoless double beta decay experiment GERDA Phase II: A novel ultra-low background contacting technique for germanium detectors and first background data

Tobias Bode

Vollständiger Abdruck der von der Fakultät für Physik der Technischen Universität München zur Erlangung des akademischen Grades eines

Doktors der Naturwissenschaften (Dr. rer. nat.)

genehmigten Dissertation.

Vorsitzender: Prof. Dr. Björn Garbrecht

Prüfer der Dissertation:
1. Prof. Dr. Stefan Schönert
2. Priv. Doz. Dr. Béla Majorovits

Die Dissertation wurde am 18.05.2016 bei der Technischen Universität München eingereicht und durch die Fakultät für Physik am 07.06.2016 angenommen.

Abstract

The lepton number violating neutrinoless double beta ($0\nu\beta\beta$) decay is a nuclear transition predicted by numerous extensions of the Standard Model. A detection of this decay would prove the Majorana nature of the neutrino and the existence of a Majorana mass component. The $0\nu\beta\beta$ decay has not yet been observed, and current half-life limits are in the 10^{25} range which lead to upper bounds on the effective Majorana mass of 200 meV. The GERDA experiment searches for this process, using HPGe detectors, enriched in the $\beta\beta$-isotope ^{76}Ge. A novel shielding technique with cryogenic liquid argon is employed. GERDA Phase I has set a world leading lower limit of $T_{1/2}^{0\nu} > 2.1 \times 10^{25}$ yr, achieving an unprecedented ultra low background in the $0\nu\beta\beta$ region of interest of 10^{-2} cts/(keV·kg·yr). To reach a half-life sensitivity of 10^{26} yr with GERDA Phase II a doubling of the target mass and a reduction of background down to 10^{-3} cts/(keV·kg·yr) were required, leading to extensive upgrades of the experimental apparatus.

A change of the detector contacting method was called for to allow for the use of ultra radio-pure, but mechanically unfavorable, materials in the detector holder structure. The chosen method was wire bonding which prior to this work had not been commonly used on large volume germanium diode detectors. Aluminium thin films were chosen as bond substrates for a reliable contacting. The required metallization process was developed and extensively tested on Ge samples and prototype detectors. The behaviour under thermal cycling, the adhesion strength and possible damage to the detector were investigated. After a successful evaluation, all 40 GERDA detectors were processed at the manufacturer.

The commissioning of the complete GERDA array commenced in July 2015 after detector mounting and application of the wire bond connection. A 99.7 % (758 of 760) bond survival rate was one of the excellent results of these runs. Since December 2015 GERDA Phase II is successfully running with the developed contacting technique. In the final immersion no faulty electrical connection occurred signifying again the robustness of the developed bonding process. Physics and commissioning data, with a total exposure of 6 kg·yr were used to determine the intensities of the γ-lines present in the Phase II spectrum. In addition, α events were examined for their rate in different detectors and types as well as for the dominant contamination, determined to be ^{210}Po as in Phase I. No indication of an additional contamination due to the detector processing and wire bonding was found. According to material screening measurements and Monte-Carlo simulations the contacting technique is estimated to have a background contribution of the order of 10^{-6} cts/(keV·kg·yr). Making this technique suitable for next-generation experiments dedicated to probe the inverted hierarchy.

Zusammenfassung

Viele Erweiterungen des Standardmodells sagen die Verletzung der Leptonenzahlerhaltung durch den neutrinolosen Doppel-Beta Zerfall ($0\nu\beta\beta$) voraus. Ein Nachweis würde den Majorana-Charakter des Neutrinos sowie die Existenz einer entsprechenden Massenkomponente beweisen. Der $0\nu\beta\beta$ Zerfall ist noch nicht beobachtet worden. Halbwertszeiten von bis zu 10^{25} a, was einer effektiven Majorana Masse von 200 meV entspricht, sind bis jetzt ausgeschlossen. Das GERDA Experiment sucht nach diesem Prozess mittels HPGe Detektoren, die mit dem $\beta\beta$-Isotop ^{76}Ge angereichert sind und einer neuartigen Abschirmung mit flüssigem kryogenem Argon. GERDA Phase I konnte ein untere Grenze von $T_{1/2}^{0\nu} > 2.1 \times 10^{25}$ a setzen, wobei gleichzeitig ein beispiellos niedriger Untergrund von 10^{-2} cts/(keV·kg·yr) erreicht wurde. GERDA Phase II verdoppelt mit einem Upgrade des Aufbaus die sensitive Masse, bei einer gleichzeitigen Reduktion des Untergrunds auf 10^{-3} cts/(keV·kg·yr) um auf eine Halbwertszeit von bis zu 10^{26} a sensitiv zu sein.

Die erforderliche Detektor-Kontaktierung musste geändert werden, da ultra reine, aber mechanisch schwache, Materialen in der Detektorhalterung benutzt werden sollten. Die gewählte Methode, Drahtbonden, wird gewöhnlich nicht für die Kontaktierung von großvolumigen Germanium Detektoren benutzt. Für eine verlässliche Bond-Verbindung wurde ein Aluminiumfilm direkt auf den Detektor aufgebracht, wobei der benötigte Metallisierungsprozess eigens entwickelt und ausführlich an Proben und Prototypen getestet wurde. Die Metallisierung wurde auf ihr Verhalten bei thermischen Zyklieren, die Haftung und mögliche Schäden am Detektor untersucht. Nach erfolgreicher Evaluation wurden alle 40 GERDA Detektoren beim Hersteller prozessiert. Das GERDA Array wurde im July 2015 in Betrieb genommen, nachdem die Detektoren montiert wurden und die Drahtbond-Verbindung durchgeführt wurde. Eines der hervorragenden Ergebnisse war eine Überlebenswahrscheinlichkeit der Bonds von 99,7 % (758 von 760). GERDA Phase II läuft erfolgreich mit der entwickelten Kontaktierung seit Dezember 2015. In dieser finalen Einbringung des Arrays wurden keine gestörten elektrischen Verbindungen festgestellt, was wieder die Verlässlichkeit des Bondprozesses beweist. Die ersten genommenen Daten wurden auf γ-Linien und α Ereignisraten analysiert. Keine zusätzliche Kontamination durch die Kontaktierung der Detektoren konnte festgestellt werden. Nur die bereits in Phase I beobachtete ^{210}Po Kontamination. Eine Abschätzung des Untergrundbeitrags mittels Monte-Carlo Simulationen und Radioaktivitätsmessungen der benutzten Materialen ergibt eine Größenordnung von 10^{-6} cts/(keV·kg·yr). Die verwendete Kontaktierungsmethode ist also geeignet für die nächste Generation von Experimenten, die die invertierte Neutrinomassenhierarchie prüfen werden.

Contents

Chapter 1

Introduction

Historically, neutrinos are among the earliest postulated elementary particles. They were suggested by Pauli already in 1930 in his famous letter to the "Radioaktiven Damen und Herren" [1]. But due to their small interaction cross-section they were only discovered in 1956 by Cowan and Reines [2]. Still this was many years before quarks, W- and Z-Bosons, τs or the Brout-Englert-Higgs-particle were postulated or discovered. Nevertheless fundamental properties (like mass) of neutrinos remained largely unknown until a few years ago when measurements by the Super-Kamiokande [3] and the SNO-Experiment [4] showed that neutrinos can change their flavor and must thus be massive particles, contrary to assumptions in the Standard Model. The Nobel Prize winning verification that neutrinos are indeed massive particles renewed the scientific interest in their fundamental properties in the last years. One now possible phenomenon is the neutrinoless double beta decay whose observation would prove the Majorana nature of the neutrino.

1.1 Neutrino properties

In this section a short overview of the known and presently unknown properties of neutrinos is given. It will be described why neutrinos were postulated and how they were finally discovered (Section 1.1.1). The technical difficulties of neutrino detection made and make measurements about their properties and origins very challenging, nevertheless over the last 85 years a steady increase in knowledge about neutrinos has been achieved.

1.1.1 Postulation and discovery

Wolfgang Pauli postulated the neutrino (then called neutron) to explain the continuous electron energy energy spectrum of the β-decay measured by Meitner and Hahn in 1911 [5]. A two-body decay into daughter nucleus and electron was in conflict with energy and angular momentum conservation. The process of

$$^{A}_{Z}X \rightarrow ^{A}_{Z-1} X + e + \bar{\nu}_e \tag{1.1}$$

with the added neutral particle $\bar{\nu}_e$ solved this problem on the expense that according to Pauli this particle apparently could never be found [1]. In Fermi's V-A theory, who coined the name neutrino, it was implemented as a weakly interacting, massless particle [6]. According to this theory MeV neutrinos, scattering on electrons, would have a cross-section of $\sigma \approx 10^{-42}\,\mathrm{cm}^{-2}$.

Finally in 1956, neutrinos (electron-antineutrinos, $\bar{\nu}_e$) were measured by Reines and Cowan in the "Poltergeist" experiment at the Savannah-River nuclear reactor [2] via the inverse β-decay

$$\bar{\nu}_e + p \rightarrow n + e \tag{1.2}$$

A second flavour state, the muon neutrino $\bar{\nu}_\mu$, was found in 1962 at the AGS Neutrino experiment at Brookhaven National Lab by Ledermann, Schwartz and Steinberger [7]. The tau flavour state of the neutrino was finally measured by the DONUT- Collaboration at the Tevatron accelerator in 2000, completing the discovery of all Standard Model neutrinos [8]. A fourth light active neutrino state interacting via the weak force is excluded with high certainty by decay width measurements of the Z_0 Boson at LEP [9]. Further sterile states are, however, not excluded and are actively searched for (see [10, 11]).

1.1.2 Massive neutrinos

Phenomenology of massive neutrinos

The discovery that neutrinos are massive particles is strongly connected to the so-called "solar-neutrino problem". The flux of electron neutrinos originating from fusion processes in the sun can be calculated according to the Standard Solar model [12]. The netto reaction of the pp-chain is

$$4p \rightarrow {}^{4}He + 2e + 2\nu_e \tag{1.3}$$

where the neutrinos carry away a few MeV of energy ($E_{\nu,max} = 20\,\mathrm{MeV}$). Many experiments, e.g., [13, 14], had measured smaller ν_e fluxes than predicted. A possible solution was that neutrinos produced in the electron flavor changed their flavor during their flight to the earth and were thus not detectable with the methods used. This flavor change is called neutrino oscillation. Indeed, these oscillations were measured independently by the Super-Kamiokande experiment for atmospheric neutrinos [3] and by the Sudbury Neutrino Observatory (SNO) for solar neutrinos [4]. In the last 15 year neutrino oscillations have been measured also for reactor $\bar{\nu}_e$ [15], accelerator-produced $\bar{\nu}_\mu$ [16] and ν_τ [17].

The basic mechanism of neutrino-oscillations is the following: The flavour eigenstates of massive neutrinos $|\nu_\alpha\rangle$ = $|\nu_e\rangle$, $|\nu_\mu\rangle$, $|\nu_\tau\rangle$ are superpositions of the mass eigenstates $|\nu_i\rangle$ = $|\nu_1\rangle$, $|\nu_2\rangle$, $|\nu_3\rangle$ with masses m_i. The unitary matrix U determines the mixing

$$|\nu_\alpha\rangle = \sum_i U_{\alpha i}|\nu_i\rangle. \tag{1.4}$$

This mixing matrix, called PMNS matrix, after Pontecorvo[1], Maki, Nakagawa and Sakata, is the equivalent to the CKM matrix in the quark sector. For three neutrino generations the matrix can be parametrised with three mixing angles θ_{ij} and three CP violating phases α_1, α_2 & δ_{CP}.

$$\begin{pmatrix} U_{e1} & U_{e2} & U_{e3} \\ U_{\mu 1} & U_{\mu 2} & U_{\mu 3} \\ U_{\tau 1} & U_{\tau 2} & U_{\tau 3} \end{pmatrix} = \tag{1.5}$$

$$\begin{pmatrix} c_{12}c_{13} & s_{12}c_{13} & s_{13}e^{-i\delta_{\mathrm{CP}}} \\ -s_{12}c_{23} - c_{12}s_{13}s_{23}e^{i\delta_{\mathrm{CP}}} & c_{12}c_{23} - s_{12}s_{13}s_{23}e^{i\delta_{\mathrm{CP}}} & c_{13}s_{23} \\ s_{12}s_{23} - c_{12}s_{13}c_{23}e^{i\delta_{\mathrm{CP}}} & -c_{12}s_{23} - s_{12}s_{13}c_{23}e^{i\delta_{\mathrm{CP}}} & c_{13}c_{23} \end{pmatrix} \begin{pmatrix} e^{i\alpha_1} & 0 & 0 \\ 0 & e^{i\alpha_2} & 0 \\ 0 & 0 & 1 \end{pmatrix} \tag{1.6}$$

where $s_{ij} = \sin\theta_{ij}$ and $c_{ij} = \cos\theta_{ij}$. The phases α_1 and α_2 are called Majorana phases and only exist if the neutrino is a Majorana particle. This specific parametrisation was taken from [18]. Any flavor eigenstate $|\nu_\alpha\rangle$ with energy E produced in a weak interaction, propagates as the sum of all mass eigenstates $|\nu_i\rangle$. Due to their different masses these states have different velocities and there is a non-vanishing probability P

$$P(\alpha \to \beta; L, E) = |\sum_k U_{\alpha k}U^*_{\beta k}e^{-\frac{m_k^2}{2}\cdot\frac{L}{E}}|^2 = \sum_{kl} U_{\alpha k}U^*_{\alpha l}U^*_{\beta k}U_{\beta l}e^{\frac{\Delta m_{kl}^2}{2E}L} \tag{1.7}$$

---

[1] Pontecorvo actually proposed $\nu \leftrightarrow \bar{\nu}$ oscillations even before the other neutrino flavors were known

Parameter	Ordering	Best fit value $\pm 1\sigma$
Δm^2_{21} $[10^{-5}\,\mathrm{eV}^2]$	NO or IO	$7.50^{+0.19}_{-0.17}$
Δm^2_{31} $[10^{-3}\,\mathrm{eV}^2]$	NO	$2.457^{+0.047}_{-0.047}$
Δm^2_{32} $[10^{-3}\,\mathrm{eV}^2]$	IO	$-2.449^{+0.048}_{-0.047}$
$\sin^2\theta_{12}$	NO or IO	$0.304^{+0.013}_{-0.012}$
$\sin^2\theta_{13}$	NO	$0.0218^{+0.0010}_{-0.0010}$
	IO	$0.0219^{+0.0011}_{-0.0010}$
$\sin^2\theta_{23}$	NO	$0.452^{+0.052}_{-0.028}$
	IO	$0.579^{+0.025}_{-0.037}$
δ	NO	306^{+39}_{-70}
	IO	354^{+63}_{-62}

Table 1.1: Neutrino flavour oscillation parameters taken from [18]. Best fit values and corresponding 1σ uncertainties are reported. Where applicable the values for inverted ordering (IO) and normal ordering (NO) are given. For a definition of IO and NO see the main text. The convention to choose Δm^2_{31} as positive and Δm^2_{23} as negative is adopted from the reference.

that a neutrino after a certain pathlength L is found in a different flavor eigenstate β. For a derivation of this formula see for example [19]. For a reactor antineutrino at long baselines $\bar{\nu}_e$ the approximate probability to be detected in the same flavor state for example is the following:

$$P(\bar{\nu}_e \to \bar{\nu}_e) \approx 1 - \sin^2 2\theta_{12} \cdot \sin^2 \Delta m^2_{12} \frac{L}{4E} \tag{1.8}$$

where θ_{12} determines the oscillation amplitude and $\Delta m^2_{12}\frac{L}{4E}$ the oscillation frequency. In the last years a rather complete picture of neutrino oscillations has emerged. All three mixing angles and the two mass squared differences ($\Delta m^2_{kl} = m^2_k - m^2_l$) have been measured in several different experiments with neutrinos from various sources (e.g., solar, atmospheric, reactor, accelerators). The measured oscillation parameters are shown in Table 1.1 taken from [18].

Any experiment measuring oscillations is only sensitive to the mass squared differences and not to the absolute mass scale. To address this questions different kind of experiments have to be conducted. Until now the mass of the lightest mass state is not known. Different spectra of the neutrino mass eigenstates (also called ordering or hierarchies) are thus possible. There are three cases that can be considered, one where $m_1 \approx m_2 \approx m_3$ which is called quasi-degenerate mass spectrum, the normal ordering (NO) case where $m_1 < m_2 < m_3$ and the inverted ordering (IO) where $m_3 < m_1 < m_2$. The sign of Δm^2_{21}, dominant for solar neutrino oscillations, can be measured through the MSW effect (a matter resonance effect in the Sun [20]). The sign of the mass-square difference dominant in oscillations on the earth scale has not been measured yet since the matter effects are much smaller but is actively investigated [21]. Inverted ordering would imply a negative sign.

The mass of $\bar{\nu}_e$ can be directly probed in precise measurements of the β-decay spectrum close to the end-point by measuring the spectral distortion by a small but finite neutrino rest mass. The measured quantity m_β is the following superposition of mass eigenstates:

$$\langle m_\beta \rangle = \sqrt{\sum_i |U_{ei}|^2 m_i^2} = \sqrt{c_{12}^2 c_{13}^2 m_1^2 + s_{12}^2 c_{13}^2 m_2^2 + s_{13}^2 m_3^2} \tag{1.9}$$

The current best limit are from the Mainz and Troitsk experiments with a mean upper limit of $m_\beta < 2\,\text{eV}$ [22, 23]. The KATRIN experiment [24], with an expected ten-times higher sensitivity, is currently in the commissioning phase.

Cosmological and astrophysical observations are also being used to determine the absolute neutrino mass scale, to be precise, to the sum of all mass states:

$$\Sigma = \sum_i m_i \tag{1.10}$$

With data from the Planck satellite mission, measuring the cosmic microwave background (CMB) and other astrophysical surveys (WiggleZ Dark Energy Survey, Sloan Digital Sky Survey) the yet most stringent but model-dependent limit can be set with $\Sigma < 0.13\,\text{eV}$ (95% C.L.) [25]. Other combinations of astrophysical data give much less stringent limits or results in tension with each other.

In recent years the finite but very small mass of neutrinos has been established. However, the question remains if and how such a small mass can be theoretically explained. In the current Standard Model there is no possibility to generate a massive neutrino. But if the neutrino is a so-called Majorana particle a massive neutrino is possible. In the following section the Majorana theory is briefly presented.

Majorana theory of the neutrino

Shortly after Fermi's V-A theory Majorana published "an essentially new theory for particles without electric charge (neutrons and hypothetical neutrinos)" [26]. The complex field

$\psi(x)$ can be written as

$$\psi(x) = \frac{\chi_1 + i\chi_2}{\sqrt{2}}, \tag{1.11}$$

where

$$\chi_1(x) = \frac{\psi(x) + \psi^c(x)}{\sqrt{2}}; \quad \chi_2(x) = \frac{\psi(x) - \psi^c(x)}{\sqrt{2}i} \tag{1.12}$$

satisfy the Dirac equations

$$(i\gamma^\alpha \partial_\alpha - m)\, \chi_{1,2}(x) = 0. \tag{1.13}$$

The fields $\chi_{1,2}(x)$ satisfy also the additional Majorana conditions

$$\chi_{1,2}(x) = \chi^c_{1,2}(x) = C\bar{\chi}^T_{1,2}(x) \tag{1.14}$$

where C is the charge conjugate operator. With this condition for the fields one can show (e.g., [27]) that the creation operator for particle (neutrino) and antiparticle (anti-neutrino) are identical and thus there is “no notion of particles and antiparticles in the case of the Majorana field” [27]. The Majorana conditions are important for the construction of possible mass terms in the Standard Model Lagrangian (or extensions thereof) which will be briefly discussed in the next section.

Possible neutrino mass terms

The smallness of the neutrino mass compared with all other SM fermions has lead to the assumption in the Standard Model that they would be massless which is now disproven by the existence of neutrino oscillations. The Standard Model must be modified in order to generate massive neutrinos. A minimal change would be to allow for a mass term in the form of

$$\mathscr{L}^{\mathrm{M}} = -\frac{1}{2}\,\bar{\nu}_L M^{\mathrm{M}}_L (\nu_L)^c + \mathrm{h.c.}, \tag{1.15}$$

where the neutrino field ν_L must satisfy the Majorana condition (see above) and M^{M} is a complex 3×3 matrix. This mass term is called *Majorana mass term.* A more general extension would be to introduce right-handed fields ν_R. The usual Higgs-mechanism is then possible. The general mass term

$$\mathscr{L}^{\mathrm{D+M}} = -\frac{1}{2}\,\bar{\nu}_L M^{\mathrm{M}}_L (\nu_L)^c - \bar{\nu}_L M^{\mathrm{D}}\,\nu_R - \frac{1}{2}\,\overline{(\nu_R)^c}\, M^{\mathrm{M}}_R \nu_R + \mathrm{h.c.}, \tag{1.16}$$

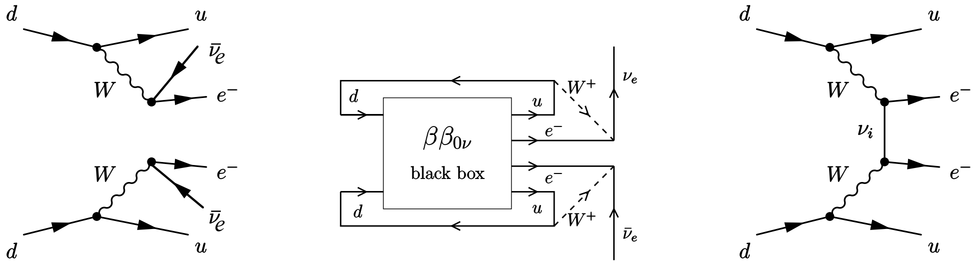

(a) Feynmann diagram of $2\nu\beta\beta$

(b) Blackbox diagram adapted from [33].

(c) $0\nu\beta\beta$ diagram with light Majorana neutrino exchange

is usually called *Dirac and Majorana mass term*. This mass term gives the possibility to explain the very small mass of the active neutrinos e.g., through the *Seesaw mechanism*. For further information see for example [27, 28]. The Majorana nature of the neutrino would allow for an exotic, nuclear decay called neutrinoless double beta decay.

1.2 The neutrinoless double beta decay ($0\nu\beta\beta$)

In general a double beta decay is a second order weak process which is possible in even - even nuclei (due to the pairing term) and observable if the single beta decay is at the same time forbidden. The two neutrino double beta decay ($2\nu\beta\beta$)

$$ {}^A_Z X \rightarrow {}^A_{Z+2} X + 2e + 2\bar{\nu}_e \tag{1.17}$$

was first proposed by Wigner and calculated by Maria Göppert-Mayer in 1935 [29] with very long half-lives $T^{2\nu}_{1/2}$ between $10^{18} - 10^{21}$ yr which is why it was only directly measured in 1987 [30] and has been detected in 11 of 35 possible isotopes until now [31, 32]. The corresponding Feynman diagram is shown in Figure 1.1a.

The neutrinoless double beta decay ($0\nu\beta\beta$)

$$ {}^A_Z X \rightarrow {}^A_{Z+2} X + 2e \tag{1.18}$$

on the other hand is only possible in extensions of the Standard Model since it violates the lepton number conservation[1] by two units (ΔL=2). The SM could be extended in the following way:

If the SM is only a low-energy effective theory, additional Lagrangian terms may be

---

[1] L is only accidentally conserved in the SM

introduced which are non-renormalizable with dimension larger than four. These would be suppressed by a factor Λ^{4-N} where Λ is the scale of new physics and N is the dimension of the additional terms (see. e.g., [28]). Such extensions lead quite naturally to Lepton number violation. As the authors of [28] put it: “It is remarkable that there is only one dimension-5 field product that can be constructed with Standard Model fields and this term violates the total lepton number L.” The $0\nu\beta\beta$ decay was suggested by Racah [34] and calculated by Furry in 1939 [35] after Majorana published his theory of the neutrino (see Section 1.1.2). Indeed it was proven by Schechter and Valle that diagrams leading to the neutrinoless double beta decay are only possible if the neutrino is a Majorana particle (a self-conjugated particle) [33]. This is depicted in Figure 1.1b. Possible mediators of this decay which differ in the various extensions of the SM, could be, among others, right-handed weak currents, supersymmetric particles or massive neutrinos. But since the observation of neutrino oscillations it is clear that massive neutrinos do exists and thus the light Majorana neutrino exchange as the leading term in the Feynman diagrams (Figure 1.1c) is particularly well motivated. As can be derived from the weak interaction hamiltonian the transition probability is proportional to the so-called effective Majorana neutrino mass (see [36], [28])

$$\langle m_{\beta\beta}\rangle = |\sum_k U_{ek}^2 m_k| = |\sum_k |U_{ek}|^2 m_k e^{i\alpha_k}| \tag{1.19}$$

where U is the PMNS mixing matrix, m_k is the mass of the k-th neutrino mass eigenstate, the sum is taken over all states contributing to the electron-neutrino mass and α_k are the respective unknown Majorana phases (for a more detailed description of neutrino mixing parameters see Section 1.1.2). The decay rate can then be written as [36]

$$[T_{1/2}^{0\nu}]^{-1} = G_{0\nu}(Q_{\beta\beta}, Z)|M_{0\nu}|^2\langle m_{\beta\beta}\rangle^2, \tag{1.20}$$

where $Q_{\beta\beta} = E_i - E_f$ (the Q-value of the decay), $|M_{0\nu}|$ is the nuclear matrix element (NME) of the decay and $G_{0\nu}(Q_{\beta\beta}, Z)$ is the Q-value and atomic number dependent phase-space factor. $G_{0\nu}$ can be calculated with high accuracy for all $\beta\beta$-isotopes but the NMEs have proven to be notoriously difficult to calculate and are an active topic of research (a review can be found in [37]). The NME predictions for most of the relevant isotopes agree within a factor of two. This leads to an added uncertainty in the conversion from measured half-lives to $m_{\beta\beta}$.

In this way an observation of the neutrinoless double beta decay can give information about the effective Majorana neutrino mass and also about the mass of the lightest neutrino

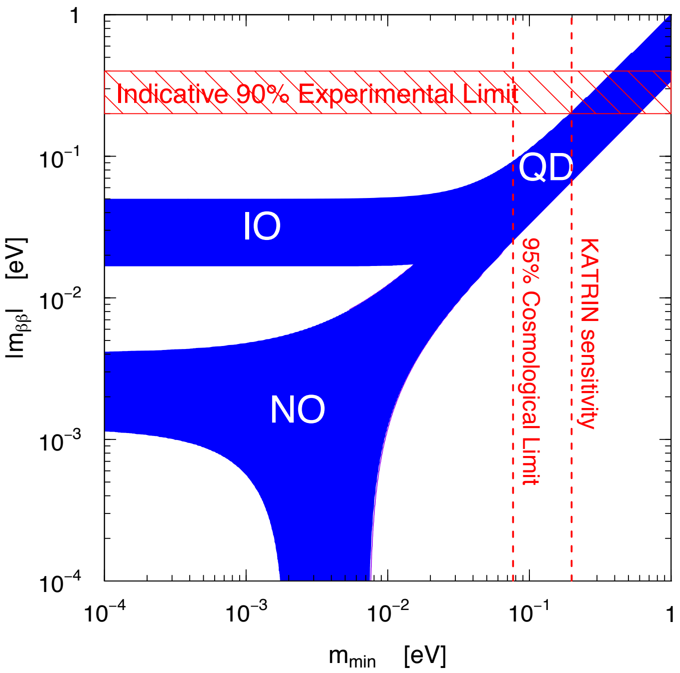

Figure 1.2: Relation between $m_{\beta\beta}$ and the lightest neutrino mass state, m_1 (NO) or m_3 (IO). KATRIN can probe $m_{\min}$ down to 0.2 eV. Current $0\nu\beta\beta$ limits for ^{76}Ge (and other isotopes) are in the $m_{\beta\beta}< 0.2$ eV range. The bands are due to the unknown Majorana phases. Adapted from [28].

state or in other words the neutrino mass spectrum (see Figure 1.2). Regardless if the massive neutrino exchange is indeed the leading term in the decay an observation of $0\nu\beta\beta$ would be the first interaction where the total lepton number conservation is violated and the Majorana nature of the neutrino would be proven. In the next section a short review of past, present and future experiments will be given.

1.2.1 Experimental search for $0\nu\beta\beta$

The experimental signature of $0\nu\beta\beta$ is a peak in the summed electron energy spectrum at the Q-value of the decay. Due to the expected extremely long half-lives ($T^{0\nu}_{1/2} \gg 10^{25}$ yr) the expected signal counts per year λ_{sig} in one mol of an "average" $\beta\beta$-isotope is $\ll 1$. This is why several 100 moles of isotope are used for current experiments. For future experiments an increase to kmols and several 100 kg isotope mass will be required to reach $T^{0\nu}_{1/2} > 10^{28}$ yr (see [38]). These small signal event rates make an extremely low background event rate λ_{bkg} in the region of interest paramount. The number of signal events λ_{sig} expected from

$0\nu\beta\beta$ (via neutrino exchange) in an experiment with mass M after a livetime of t is

$$\lambda_{sig} = \ln 2 \cdot N_A \cdot \varepsilon \cdot \eta \cdot M \cdot t / m_{mol} \cdot T_{1/2}^{0\nu}. \tag{1.21}$$

Here N_A is the Avogadro number, ε the detection efficiency for the decay-electrons, η and m_{mol} are the $\beta\beta$-isotope mass fraction and the molar mass, respectively. A figure of merit F is widely used in the $0\nu\beta\beta$ community to estimate and compare the sensitivity of given experiments on $T_{1/2}^{0\nu}$. In the usual case where the expected number of background events during the livetime (λ_{bkg}) is > 0 and assuming that it scales according to

$$\lambda_{bkg} = M \cdot t \cdot B \cdot \Delta E \tag{1.22}$$

with B as the so-called background index normalised to mass, time and energy (usually $\frac{1}{keV \cdot kg \cdot yr}$) and ΔE as the FWHM energy resolution around the Q-value, the figure of merit F can be written as

$$F \propto \ln 2 \cdot \frac{N_A}{m_{mol}} \cdot \varepsilon \cdot \eta \cdot \sqrt{\frac{M \cdot t}{B \cdot \Delta E}}. \tag{1.23}$$

This is an approximation (gaussian distribution of background and proportional scaling of background with mass) but nevertheless gives a figure which can be well used to compare experiments with different tradeoffs, increasing mass but losing energy resolution or low mass experiments with high mass fraction, etc. The figure of merit can also be estimated in the case of a quasi-background free experiment[1]

$$F_0 \propto \ln 2 \cdot \frac{N_A}{m_{mol}} \cdot \varepsilon \cdot \eta \cdot M \cdot t. \tag{1.24}$$

Since the increase of sensitivity with livetime is quickly saturated in the case with considerable background, many running and upcoming experiments, including the GERDA experiment, aim to be quasi-background free for the first years of measurement [39]. A non-reducible source of background can be the much faster $2\nu\beta\beta$. Experiments with only "moderate" energy resolution ($\gtrsim 2\%$) will have non-negligible probability that $2\nu\beta\beta$ events "leak" into the $0\nu\beta\beta$ region of interest [40]

A design of a $0\nu\beta\beta$ experiment depends on the choice of the used $\beta\beta$-isotope and on the corresponding detection technique suited best for this isotope. Table 1.2 gives an overview of the characteristics of the most prominent $\beta\beta$-isotopes.

Desired properties in a $\beta\beta$-isotope are

---

[1] where the probability for $\lambda_{\mathrm{bkg}} = 1$ during the livetime is $\ll 1$

Isotope	$G^{0\nu}$ $[\frac{10^{-14}}{yr}]$	$Q_{\beta\beta}$ [keV]	Natural abundance [%]	$T_{1/2}^{2\nu}$ [10^{20} yr]	Experiments
^{48}Ca	6.3	4273.7	0.187	0.44	CANDLES
^{76}Ge	0.63	2039.1	7.8	15	GERDA, MAJORANADem.
^{82}Se	2.7	2995.5	9.2	0.92	SuperNEMO , LUCIFER
^{100}Mo	4.4	3035.0	9.6	0.07	MOON, AMORE
^{116}Cd	4.6	2809.1	7.6	0.29	COBRA
^{130}Te	4.1	2530.3	34.5	9.1	CUORE, SNO+
^{136}Xe	4.3	2457.8	8.9	21	EXO, NEXT, KAMLAND-Zen

Table 1.2: Comparison of relevant $\beta\beta$-isotopes for past, current and future experiments (from [31]).

- a high Q-value since this gives a large phase space factor and the region of interest will be above the natural occurring γ background from ^{208}Tl at 2.6 MeV or even above the β-endpoint of ^{214}Bi at 3.3 MeV.
- high natural abundance of the $\beta\beta$-isotope and/or easy and cheap enrichment possibility
- a viable detection technique associated with the isotope

$0\nu\beta\beta$ detection techniques

Unfortunately, no isotope matches in a perfect way all these requirements and therefore, experimentalists have to make certain tradeoffs to build a sensitive $0\nu\beta\beta$ experiment. The most restrictive property is to find a viable detection technique for the specific isotope. An overview of current and future techniques is given here. First of all a distinction between so-called calorimetric (source volume = detector volume) and external source experiments must be made. An advantage of the external source technique is the possibility to tailor the detector properties independently of the isotope material. This allows to use the best and most reliable detector technologies for track reconstruction (event topology). A severe disadvantage is the small measurement efficiency for β electrons which is made worse by the fact that only small isotope masses can be manufactured into source material. The sources must be produced into thin foils since otherwise the βs will lose too much energy via scattering in the source material itself, thus broadening the expected $0\nu\beta\beta$ peak. The current best experiment with this approach is NEMO-3. It used seven $\beta\beta$-isotopes (^{82}Se, ^{96}Zr, ^{100}Mo, ^{116}Cd, ^{130}Te & ^{150}Nd) and measured the $2\nu\beta\beta$-decay for all of them. The best limit (90% C.L.) for $0\nu\beta\beta$ was obtained for ^{100}Mo with $T_{1/2}^{0\nu} > 1.1 \times 10^{24}$ yr [41]. Future external source experiments will face the severe problem of the limited isotope mass.

The calorimetric approach on the other hand is employed by several quite different techniques using the detection channels offered by the specific isotope/element. These are for instance:

- Time projection chambers (TPC) filled with liquid or gas
- Liquid scintillator doped with $\beta\beta$-isotope
- Cryogenic bolometers made from scintillating $\beta\beta$-isotope crystals
- Solid state detectors

Time projection chambers

TPCs filled with liquid gas (usually xenon, enriched in ^{136}Xe) detect the prompt scintillation light signal of an interaction via photosensors (e.g., PMTs, APDs), the created charge clouds are drifted through an electric field and thus the amplified primary ionisation is measured. Interactions can be reconstructed with a spatial resolution of ca. one centimetre allowing to perform a fiducial volume cut to reduce external background. Due to the high self-shielding of the dense liquid rare gas background indices of $\mathcal{O}(10^{-3}$ cts/(keV·kg·yr)) have been achieved [42]. Although large masses (several 100 kg) have already been used, a significant fraction of precious isotope mass is lost in this fiducial volume cut. Liquid TPCs feature a good energy resolution ($< 2\%$ at $Q_{\beta\beta}$) and some event topology reconstruction (distinction of single site events, the $\beta\beta$-signal, from multiple site events, e.g., γs). The EXO experiment uses this approach with a detector mass of 200 kg (active $\beta\beta$-isotope 650 mol) and has reported for ^{136}Xe a limit (90% C.L) of $T_{1/2}^{0\nu} > 1.1 \times 10^{25}$ yr [43]. An increase in mass (together with a larger TPC) up to 5 t is proposed.

Another possibility which is pursued by the NEXT collaboration is to fill the TPC with pressurised gaseous xenon. In this less dense detector the electrons will show an extended track in contrast with a point-like interaction in liquid or solids. The advantage of gaseous xenon is an excellent event topology reconstruction of the two electron tracks, allowing rejection of pair-produced single electrons from external γs and the very good energy resolution of $< 1\%$ at $Q_{\beta\beta}$. The self-shielding is reduced due to the smaller density, making material selection even more important. The planned sensitivity for this project is $\approx 6 \times 10^{25}$ yr [44].

Doped liquid scintillator

An approach which uses already in the present experiments very large isotope masses is the doping of a liquid scintillator with a $\beta\beta$-isotope and detection of the emitted scintillation light. In the case of the KAMLAND-Zen[1] project approx. 300 kg of ^{136}Xe were solved in 13 t of liquid scintillator which was filled in a radio-pure nylon balloon. For shielding this balloon was surrounded by 1000 t of undoped scintillator. The detection of scintillation light by PMTs gives a reasonable spatial resolution and allows a fiducial volume cut with 130 kg ^{136}Xe remaining. The biggest advantage of this kind of experiment is the large isotope mass deployable and relatively easy scalability. A distinct disadvantage is the low energy resolution of $\approx 10\,\%$ which leads to a high leakage of $2\nu\beta\beta$ events into the region of interest. Additionally, no active background rejection is possible, the only signal is a deviation from the expected background spectrum. In the past run of KAMLAND-Zen an unexpected high background component was found. Purification of the liquid scintillator was performed and the resulting half-life limit of $T^{0\nu}_{1/2} > 2.6 \times 10^{25}$ yr is very competitive at present [45].

SNO+ similarly is planning to use the infrastructure of the SNO experiment and will dissolve 780 kg of ^{130}Te in liquid scintillator. [46]

In contrast to the single volume detectors discussed before, several other experiments are using modular detectors which have in common the advantage of an excellent energy resolution. Usually they can also use additional information about the detected events apart from the energy.

Crogenic bolometers

One type of such modular detectors are cryogenic bolometers. Small crystals (hundreds of gram) consisting partly or completely of an $\beta\beta$-isotope are equipped with very sensitive phonon sensors (e.g., Neutron Transmutation Doped Germanium Thermistors or superconductive Transition Edge Sensors) which measure lattice vibrations (phonons) induced by particle interactions in the crystal..

The CUORE experiment which is currently in the commissioning phase will use 988 crystals made from tellurium (with a natural ^{130}Te abundance of $\approx 30\%$) with a planned sensitivity of $T^{0\nu}_{1/2} > 1 \times 10^{26}$ yr [47]. A first stage (CUORE-0) with 52 crystals gave a half-life limit of $T^{0\nu}_{1/2} > 2.7 \times 10^{24}$ yr. [48] Other experiments are in the planning or prototype phase such as LUCIFER [49], LUMINEU [50] and AMoRE [51] which will use scintillating

---

[1] Reusing much if the radio-pure infrastructure of the previous KAMLAND experiment

crystals made from compounds of Ca, Mo, Cd or Se (with ^{48}Ca, ^{82}Se, ^{100}Mo, ^{116}Cd). A dangerous source of background for this type of experiment are αs located on the detector surface [52]. Scintillating crystals have the added advantage of the scintillation light read-out channel which can be used to suppress surface αs since the amount of light from an α interaction is quenched (or increased in case of ZnSe) with respect to β/γ interactions [38]. In principle α background in the case of non-scintillating crystals can be suppressed by detection of Cherenkov light where αs would not make any light (due to their high mass/low velocity) and β/γ interactions would produce such light. The feasibility of detecting such low intensity light was shown recently [53].

Solid state detectors

Another widely used modular detector type are high-purity germanium (HPGe) solid state detectors well known from γ-ray spectroscopy. In this case only the ionisation signal of an particle interaction is read-out, to identify e.g., the interaction site or the particle type additional information like the pulse shape has to be recorded as well. The only possible $\beta\beta$-isotope is ^{76}Ge which has a rather low Q-value of 2.039 MeV resulting in an unfavourable small phase space factor. But due to the well established detection technique HPGe detector experiments have been and are still today very competitive and among the leading $0\nu\beta\beta$ experiment.

The usual experimental setup consists of a vacuum cryostat, made from radio-pure copper, housing individual or multiple detector crystals and several layers of high purity copper and lead to shield against external radiation. This arrangement is typically surrounded by a plastic muon veto.

Until recently the leading experiment in the $0\nu\beta\beta$ field was the germanium based Heidelberg-Moscow (HDM) experiment which was operated from 1990 to 2003 in the Gran Sasso Underground Laboratory, Italy. It accumulated a total of 71.7 kg·yr exposure and in 2001 (with an exposure of 47.7 kg·yr) set a limit of $T^{0\nu}_{1/2} > 1.9 \times 10^{25}$ yr [54]. A subgroup of this collaboration claims a positive signal after further event selection via a neural network of $T^{0\nu}_{1/2} = 1.19 \times 10^{25}$ yr corresponding to a range of $m_{\beta\beta} = 100 - 900$ meV [55, 56]. This claim has been under intense discussion and several critical remarks have been published since (e.g., [31, 57]). An unambiguous investigation can only be achieved by an experiment using the same isotope (^{76}Ge). In Table 1.3 a selection of past, current and future experiment with corresponding isotope masses, results or sensitivities can be found.

At the moment two germanium experiments are set-up and take physics data. The

Experiment	Isotope	Isot. amount [mol]	Detection technique	$T_{1/2}^{0\nu}$ [10^{25} yr]
Past experiments				
HDM	^{76}Ge	130	Ge-diode	1.9
IGEX	^{76}Ge	70	Ge-diode	1.6
CUORICINO	^{130}Te	85	cryo. bolometer	0.28
NEMO-3	^{100}Mo	70	Track. & calorim.	0.11
Current experiments				
EXO-200	^{136}Xe	650	Liquid TPC	1.1
KAMLAND-Zen	^{136}Xe	660	Liquid scint.	2.6
CUORE-0/CUORE	^{130}Te	90/1600	cryo. bolometer	0.27/10
GERDA-I/GERDA-II	^{76}Ge	210/360	Ge-diode	2.1/20
MAJORANA-Demo.	^{76}Ge	340	Ge-diode	20
CANDLES	^{48}Ca	13	Scint. crystal	-
Under construction				
NEXT	^{136}Xe	660	Gas TPC	6
SuperNEMO-Dem.	^{82}Se	85	Track. & calorim.	0.7
SNO+	^{130}Te	4500	Liquid scint.	9
Proposal/Prototypes				
AMORE	^{100}Mo	-	cryo. scint. bolom.	-
COBRA	^{116}Cd	-	crystalline TPC	-
LUCIFER	^{82}Se/^{100}Mo	-	cryo. scint. bolom.	-

Table 1.3: Comparison of active amount of isotope and sensitivities of past, current and future experiments (adapted from [31]). For the past experiments, EXO-200, KAMLAND-Zen, CUORE-0 and GERDA-I final results are given, otherwise projected sensitivities.

MAJORANA-DEMONSTRATOR is currently in the commissioning phase and will use ~26 kg of isotope mass [58]. This approach employs underground-grown copper with ultra-low levels of radioactive contaminations ($< 0.2\,\mu$ Bq/kg of ^{238}U/^{232}Th) for the cryostat housing and shielding. Its projected sensitivity is 2×10^{26} yr [59]. A different shielding approach is used by the GERDA (GERmanium Detector Array) experiment which was specifically built to test the claim. In the next chapter the experimental apparatus and the first result, strongly disfavoring the claim, will be shown. An overview of the detector working principle and conducted improvements for the next more sensitive Phase II of the experiment is given as well.

Chapter 2

The GERDA experiment

The GERDA (Germanium Detector Array) experiment searches for the neutrinoless double beta decay ($0\nu\beta\beta$) of ^{76}Ge. It uses a novel experimental approach where the detectors are shielded from external radiation through immersion in a liquid argon volume. This technique was suggested in [60] and adopted by the GERDA collaboration [61]. In GERDA Phase I the already mentioned (Section 1.2.1) claim by a subgroup of the HDM experiment was scrutinized . The experimental apparatus and service facilities are located in the INFN Laboratori Nazionali del Gran Sasso (LNGS) shielded by 3500 m.w.e of rock. The goal was to build an experiment which during its measurement phase and corresponding exposure would be quasi-background free according to the definition given in Section 1.2.1 and Formula 1.24. In the following two sections an overview of the experimental apparatus and the working principle of germanium detectors is given. GERDA Phase I has already been completed and its setup and results are discussed in Section 2.3. GERDA Phase II will be used to investigate $0\nu\beta\beta$ half-lives of about 10^{26} yr. This work was conducted in the context of this next phase of GERDA. The modified setup of Phase II is described in Section 2.4. Modifications include the extensive use of a new type of detectors which are introduced in Section 2.5 and the reduction of background in the ROI via, amongst others, a new even more radio-pure detector mount (Section 2.6). Testing and covering the inverted mass hierarchy region (see Section 1.1) will require half-life sensitivities of 10^{27}-10^{28} yr. In this regard GERDA Phase II and its developed methods for increasing the sensitivity can be seen as a viability test for reaching and covering the inverted mass hierarchy region via germanium based $0\nu\beta\beta$ experiments.

2.1 Experimental apparatus

The centerpiece of GERDA are the high-purity germanium diodes made from germanium enriched in ^{76}Ge ($^{\text{enr}}$Ge). The decay source volume is identical to the detector volume (source = detector geometry) as described in Section 1.2.1. These diodes are assembled into strings and are held by an ultra radio-pure, low-mass copper structure (see Figure 2.3a). The diodes are read-out via custom-made charge-sensitive amplifiers which are placed between 50-80 cm from the diodes to reduce the background contribution from this component. A schematic view of the GERDA setup is shown in Figure 2.1. The complete assembly is immersed into the liquid argon (LAr) volume by a stainless steel chain accommodating also all the necessary cabling. Access is made through a lock structure housed in an argon-flushed glove-box. The stainless steel cryostat volume is 63 m^3 and holds 70 t of liquid argon. Apart from shielding the detectors from external radiation, the cryogenic (89 K) liquid argon serves also as cooling medium for the proper detector operation. The cryostat is surrounded by a 590 m^3 water-filled tank acting as neutron shield and muon veto. It is equipped with PMTs to detect the Cherenkov light caused by traversing muons. On top of the tank sits a Class 100 clean room containing lock structure, glove-box and preparation clean-benches. For further detailed information about the experimental apparatus see [39]. The working principle of high-purity germanium detectors is presented in detail in the next section.

2.2 High-purity germanium detectors

The detectors used by GERDA are germanium detectors supplied by CANBERRA Semiconductor NV. They are made from mono-crystalline germanium of very high-purity ($< 10^{11}$ cm^{-3} impurities [1]). For the GERDA detectors p-type material is used. A pn-junction is formed by doping the outer surfaces with n-material, e.g., lithium, phosphorus or arsenic. The active volume of the detector is the depletion zone, formed by applying a reverse bias voltage. This zone is then devoid of free charge carriers. An incident radiation particle (alpha, electron or photon) creates electrons and corresponding holes which travel along the present electric field lines to the positively/negatively charged electrodes. These moving charges induce a charge build-up in the electrodes which is amplified and read out. The readout necessitates a physical metal-semiconductor contact. To avoid injection of minority charge carriers (in p-type electrons) from the metal a highly doped p-type (p$^+$) region

---

[1] Only electrically active impurities which donate or accept electrons are considered here

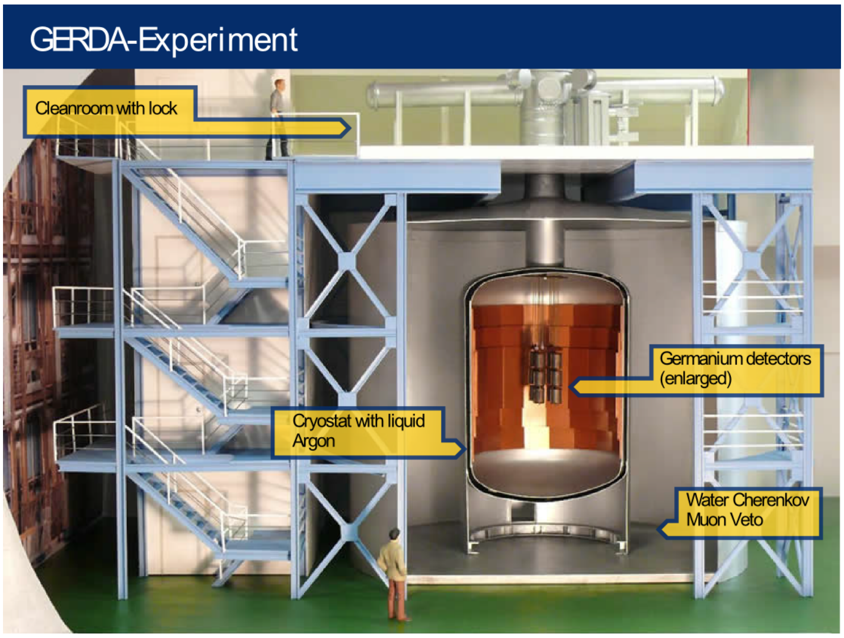

Figure 2.1: Artist's view of the GERDA experiment.

is formed by implanting boron atoms in the germanium. Diffused lithium is used to form the n^+- electrode where the bias voltage is usually applied. Various germanium detector geometries with different specifications and advantages exist. In Figure 2.2 two typical detector geometries are shown. For Phase I p-type semi-coaxial diodes were used. For Phase II a new type will be used in addition (see Section 2.5).

2.2.1 Leakage currents in high-purity germanium diodes

An important operational parameter is the so-called leakage current (LC) of a diode. Originating from the bulk or the surface of the diode it mimics the moving charges produced by ionizing radiation. The bulk LC can be caused by thermally generated electron-hole pairs or by minority carrier injection across the junction [63]. The first is suppressed by usage at cryogenic temperatures $< 100\,\mathrm{K}$ and the latter by an undamaged n^+ and p^+- electrodes. For practical purposes the bulk LC is mostly negligible. Surface LC on the other hand can be significant. As shown in Figure 2.2, at the so-called groove an interface between undoped germanium and the outside environment exists. Surface conductivity of crystalline germanium is strongly dependent on the exposure history of that interface. Oxidation enhanced by humidity in air and other contaminants degrade the interface [64, 65]. Large electric field gradients, present at the edges of the junction in the groove, in combination

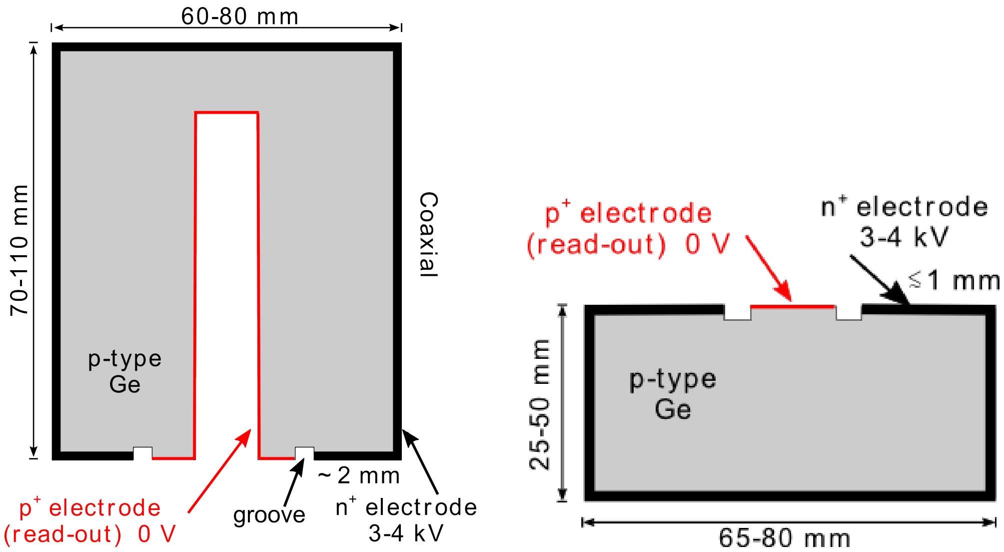

(a) Semi-coaxial p-type geometry

(b) So-called Broad Energy Germanium (BEGe) detector geometry

Figure 2.2: Typical germanium detector varieties used in the GERDA experiment. In both cases the positive high voltage is applied to the n^+- electrode which results in a high electric field gradient across the groove to the p^+- electrode. From [62].

with low surface resistivity lead to LCs in the order of nA. Usually this interface is stabilized or passivated by an additional silicon oxide layer. This LC represents a form of noise and can potentially degrade the detector energy resolution. The proper handling of the diodes, as described in [64] and Section 4.4, is paramount to achieve low LCs. Damage to the electrodes must also be avoided. Implantation of boron atoms usually gives a very thin ($\sim$ 300 nm) and thus sensitive p^+- region, whereas the enveloping n^+- electrode is up to one millimeter thick and quite rugged. These particular properties have consequences for this work and will be discussed in detail in Sections 3.2 and 4.1. Before the physics data taking of Phase I the long-term operation of germanium detectors in liquid argon was verified [64]. Strong γ-radiation (i.e., from calibration sources) induced a non-negligible leakage current in passivated diodes. It was therefore decided to remove this passivation layer whenever possible. The need to remove the diodes' passivation layers complicates the handling procedure further. Oxygen and humidity exposure must be avoided at all cost. This has consequences for bonding, as discussed in Chapter 3.

2.3 GERDA Phase I setup and results

The goal of Phase I was to probe the claimed signal for $0\nu\beta\beta$. To achieve this eight reprocessed semi-coaxial high-purity germanium detectors made from $^{\mathrm{enr}}$Ge already used in the HDM and IGEX experiments were employed. At a later stage five detectors of a new type, so-called Broad Energy Germanium (BEGe) detectors, were added. Details of the individual detector masses and performances are shown in Table 2.1. This performance was reached with low-activity, custom-made charge-sensitive amplifiers located 50 cm far from the diodes. Pictures of this setup can be seen in Figures 2.3a and 2.3b.

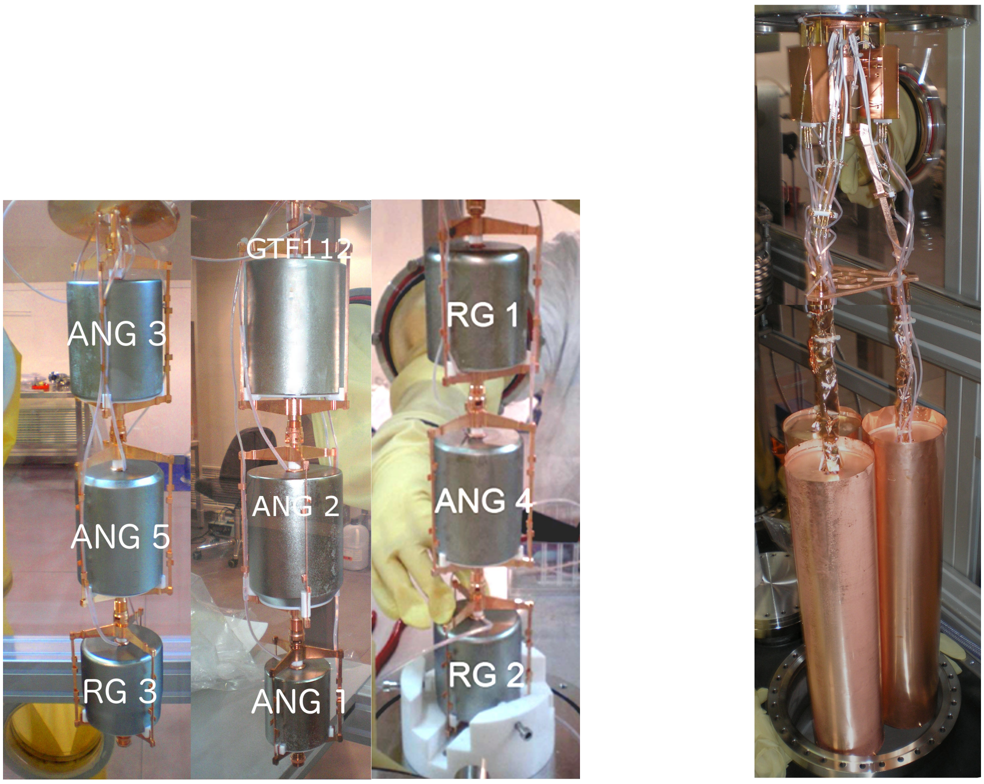

(a) Three detector strings with eight detectors from enriched Germanium and one from natural material

(b) Copper shrouds shielding the detectors against ^{42}Ar and ^{42}K induced background and front-end electronics (upper part)

Figure 2.3: Three string detector arrangement in Phase I

detector	mass [g]	FWHM [keV]	detector	mass [g]	FWHM [keV]
ANG 2	2833	5.8 (3)	GD32B	717	2.6 (1)
ANG 3	2391	4.5 (1)	GD32C	743	2.6 (1)
ANG 4	2372	4.9 (3)	GD32D	723	3.7 (5)
ANG 5	2746	4.2 (1)	GD35B	812	4.0 (1)
RG 1	2110	4.5 (3)			
RG 2	2166	4.9 (3)			
Mean	2436	4.8 (2)	mean	749	3.2 (2)

Table 2.1: Energy resolution (FWHM) at $Q_{\beta\beta}$ and masses of the enriched detectors used in the half-life analysis. The mean energy resolution for BEGe is mass weighted. The uncertainties of the masses is ca. one gram.

2.3.1 Background sources in Phase I

After running Phase I from November 2011 to May 2013 the exposure accumulated by the semi-coaxial detectors was 17.9 kg·yr and for BEGe detectors 2.4 kg·yr respectively. With a slightly smaller dataset (16.7 kg·yr for semi-coaxial detectors) a comprehensive background model was developed [62]. A short overview of the most important components relevant for this work is presented here (see Figure 2.4).

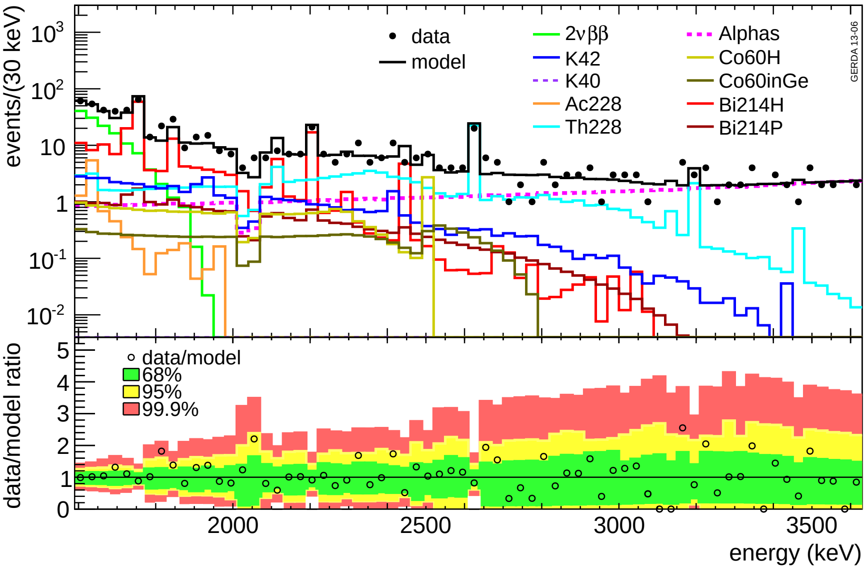

Figure 2.4: GERDA Phase I background spectrum and corresponding Monte-Carlo model around $Q_{\beta\beta}$. From [62].

Component	Location	Coax		BEGe		From screening
		BI 10^{-3} cts/(keV·kg·yr)				
^{42}K	LAr hom.	3.0	[2.9, 3.1]	2.0	[1.8, 2.3]	–
^{42}K	p^+ surface	4.6	[1.2, 7.4]			–
^{42}K	n^+ surface	0.2	[0.1, 0.4]	20.8	[6.8, 23.7]	–
^{60}Co	close to diodes	0.9	[0.3, 1.4]		<4.7	–
^{60}Co	germanium	0.6	>0.1	1.0	[0.3, 1.0]	–
^{214}Bi	close to diodes	5.2	[4.7, 5.9]	5.1	[3.1, 6.9]	$\approx$2.8
^{214}Bi	p^+ surface	1.4	[1.0, 1.8]	0.7	[0.1, 1.3]	–
^{228}Th	close to diodes	4.5	[3.9, 5.4]	4.2	[1.8, 8.4]	<0.3
α model	p^+ surface	2.4	[2.4, 2.5]	1.5	[1.2, 1.8]	–
Total		18.5	[17.6, 19.3]	38.1	[37.5, 38.7]	

Table 2.2: The total background index (BI) and individual contributions in 10 keV (8 keV for BEGes) energy window around $Q_{\beta\beta}$. Given are the values due to the global mode together with the uncertainty intervals obtained as the smallest 68 % interval of the marginalized distributions. Limits are given with 90 % C.L. For details see [62].

Table 2.2 adapted from [62] shows a more detailed list of backgrounds, locations, contributions to the background index (BI) and the individual expected BIs from screening.

As can be seen in this table the BIs due to the individual screened components do not match well with the BIs derived from the background model, indicating that unidentified close-by ^{214}Bi and ^{228}Th sources could be present.

Already during commissioning of Phase I an unexpected high background originating from ^{42}Ar and its progeny ^{42}K was found. ^{42}Ar decays homogeneously in LAr with a half-life of 32.9 yr via β-decay to ionized ^{42}K. These ions are drifted along electrical field lines generated by the bias-voltage and decay, under the emission of a β ($T_{1/2}$=12.4 h, Q=3.5 MeV), close the detectors with an accompanying 1525 keV γ. Consequently shielding the detectors from this constant aggregation of ^{42}K ions very much reduces the background at $Q_{\beta\beta}$. This shielding was performed by enclosing the detector strings with a copper foil, called mini-shroud, see Figure 2.3b. This mini-shroud accounts for nearly the entire background index from ^{214}Bi identified by screening [66]. Additionally surface contaminations, especially from the ^{226}Ra chain, are notoriously hard to assay and remove. Due to the large surface of such a foil this problem is amplified.

Another cause for the higher background could be the detector mounting structure (detector assembly) itself. Comparing the measured BI contribution from ^{228}Th, one roughly finds a factor of 10 with respect to the expected one from screening. Although this source of contamination was not conclusively determined it was decided to design a new detector mounting structure for Phase II which would be even more radio-pure and use even less mass per kilogram detector mass. In conjunction, a new contacting solution for the signal and high-voltage connections was developed and tested whose results are presented in this work (see Chapters 3 and 4). In Section 2.6 the detector mount design, materials, radio-purity and its design's implications for the contacting solution are discussed.

A significant background contribution (for coaxial detectors) stems from contaminations which are located on the surface of the diodes (α model). These are mostly α emitting isotopes from the ^{226}Ra chain. Although α usually have higher energies than the $Q_{\beta\beta}$ they lose energy while traveling through the diode dead layers. The n^+- layer is thicker than the α penetration depth, but the p^+-electrode and the groove region dead layers are so thin that α -particles have a continuous contribution to the energy spectrum around $Q_{\beta\beta}$.[1] A clean p^+- electrode is therefore very important to be kept during all handling of the diodes. This surface area is much reduced ($\sim 10\times$) in the BEGe type diodes used in Phase II. Nevertheless every new contacting method must pay attention not to introduce more α background through contaminated materials in direct contact with the p^+- electrode (see Sections 4.1.2 and 8.2.2).

2.3.2 Half-life limit of neutrinoless double beta decay of ^{76}Ge

A total exposure of 21.6 kg·yr of germanium enriched to 86% in ^{76}Ge was accumulated for the $0\nu\beta\beta$ half-life analysis. As can be seen in Table 2.1 the interpolated energy resolution at $Q_{\beta\beta}$ varies for different diodes and detector types. The exposure-averaged FWHM is (4.8 ± 0.2) for semi-coaxial and (3.2 ± 0.2) for BEGe detectors. A blind analysis was performed, meaning events in the $Q_{\beta\beta}\pm 20$ keV region were initially not processed to avoid biased event selection. The energy region between 1930-2190 keV (excluding the ROI at $Q_{\beta\beta}$ and known ^{208}Tl and ^{214}Bi γ lines) with a net width of 230 keV was used to monitor the background index around $Q_{\beta\beta}$. The accumulated data were divided into three data sets. 1) Golden coaxial data with low background. 2) Silver coaxial data with higher background. 3) The BEGe data set. After finalizing energy calibration, quality and pulse-shape discrimination (PSD) cuts the events around $Q_{\beta\beta}$ were processed. In Table 2.3 the number of found events and surviving events after PSD cut and other important parameters for the half-life analysis can be found (adapted from [67]).

The combined spectrum with- and without PSD is shown in Figure 2.5. In total only

---

[1] Due to the isotropic emission the pathlengths into the active volume vary significantly

data set	exposure	BI		expected cts		observed cts	
	[kg·yr]	10^{-3} cts/(keV·kg·yr)		($Q_{\beta\beta}\pm5$ keV)		($Q_{\beta\beta}\pm5$ keV)	
golden	17.9	18^{+2}_{-2}	11^{+2}_{-2}	3.3	2.0	5	2
silver	1.3	63^{+16}_{-14}	30^{+11}_{-9}	0.8	0.4	1	1
BEGe	2.4	42^{+10}_{-8}	5^{+4}_{-3}	1.0	0.1	1	0

Table 2.3: Parameters for the three data sets with and without the pulse shape discrimination (PSD) applied. "BI" the background index in 230 keV window. "Expected cts" is the number of counts in the ROI ($Q_{\beta\beta}\pm5$ keV) extrapolated from the BI. "Observed cts" is the number of counts observed in the ROI.

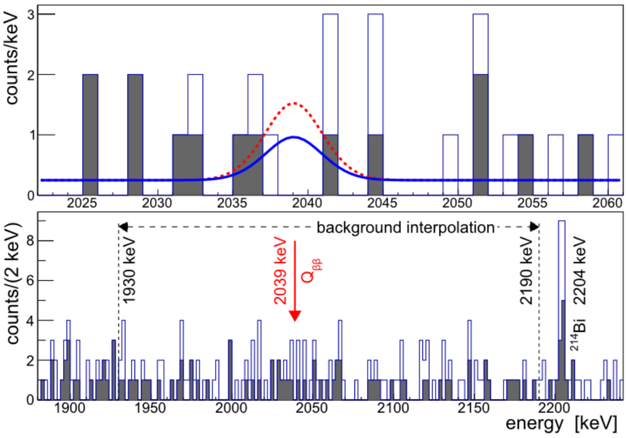

Figure 2.5: Combined energy spectrum of all ^{76}Ge detectors 230 keV around the ROI (below) and 40 keV around the ROI (top) at 2039 keV. Filled bar histogram is with PSD cut applied, non-filled without PSD cut applied. From [67].

three events survive all cuts which is well compatible with the expectation from the a priori analyzed background. The pulse-shape discrimination method used is explained in great detail in [68] and briefly in Section 2.5.1. A profile likelihood fit was performed to determine the counts due to $0\nu\beta\beta$ ($N_{0\nu\beta\beta}$) and the frequentist coverage interval. The best fit result is $N_{0\nu\beta\beta} = 0$ which corresponds to a half-life limit of

$$T^{0\nu}_{1/2} > 2.1 \cdot 10^{25}\ \text{yr} \quad (90\,\%\ \text{C.L.}) \tag{2.1}$$

More details and a Bayesian analysis can be found in [67]. The GERDA Phase I data show no peak at $Q_{\beta\beta}$ and thus the afore mentioned claim is strongly disfavored. From the claimed half-life ($T^{0\nu}_{1/2}= 1.19\times10^{25}$ yr) 5.9 ± 1.4 events from $0\nu\beta\beta$ decays would be expected over a background of 2.0 ± 0.3 events. A Bayesian hypothesis test with a background + signal model(H_1) against a background-only model (H_0) leads to a small Bayes factor $p(H_1)/p(H_0) = 0.024$. The (frequentist) p-value is $\mathrm{P}(N_{0\nu\beta\beta} = 0|H_1) = 0.01$. GERDA Phase I thus reached its goal to probe the claim and strongly disfavor it. A combination with the IGEX and HDM data gives an even stronger limit of

$$T^{0\nu}_{1/2} > 3.0 \cdot 10^{25}\ \mathrm{yr}\quad (90\%\ \ \mathrm{C.L.}) \tag{2.2}$$

The corresponding range for the upper limit on the effective neutrino mass $m_{\beta\beta}$ is 0.2-0.4 eV. To reach the allowed inverted hierarchy interval $0.02 < m_{\beta\beta} < 0.05$ eV (see Section 1.1) the sensitivity must be $\mathscr{O}(10^{27}$ yr). That is why an upgrade (Phase II) was envisaged from very beginning of the GERDA project. This Phase II will have a sensitivity $\mathscr{O}(10^{26}$ yr) and is at the same time a technology test bed for future large-scale double beta experiments.

2.4 GERDA Phase II setup

After completion of Phase I the apparatus was significantly upgraded. The available target mass was increased by 20 kg of detectors. Due to the increased target mass a larger lock structure was needed to be constructed inside the existing glove box. To remain in the quasi-background free regime (see Formula 1.24) with this increased target mass the background around the ROI needs to be reduced by one order of magnitude to 10^{-3} cts/(keV·kg·yr). This can be achieved by using even radio-purer materials close to the diodes, for example in the detector mount as will be discussed in detail in Section 2.6.

In addition, there is the active reduction (rejection) of backgrounds. Either by identifying events that originate outside the diodes, e.g., from the detector mount or electronics, and can thus be considered not to be a signal event. Or by identifying particles via analysis of the pulse shape that have a different interaction pattern in the detectors than the electrons emitted during double beta decay. The latter method is discussed in the next Section 2.5.

Radiation particles that originate from outside the diodes produce with high probability scintillation light in the LAr. This light can be wavelength-shifted and then detected by photo-sensors and used as an anti-coincidence veto. In GERDA Phase II a combination of low background conventional PMTs and a optical fiber curtain read out with small SiPMs is used to detect the scintillation light with high probability. The copper shrouds against ^{42}K background need to be replaced by transparent ones for high efficiency detection of scintillation light. The design of the liquid argon veto system is shown in Figure 2.6.

A total of forty detectors are being used in Phase II. By arranging these into seven closely packed strings the probability of detecting Compton scattered γs in multiple detec-

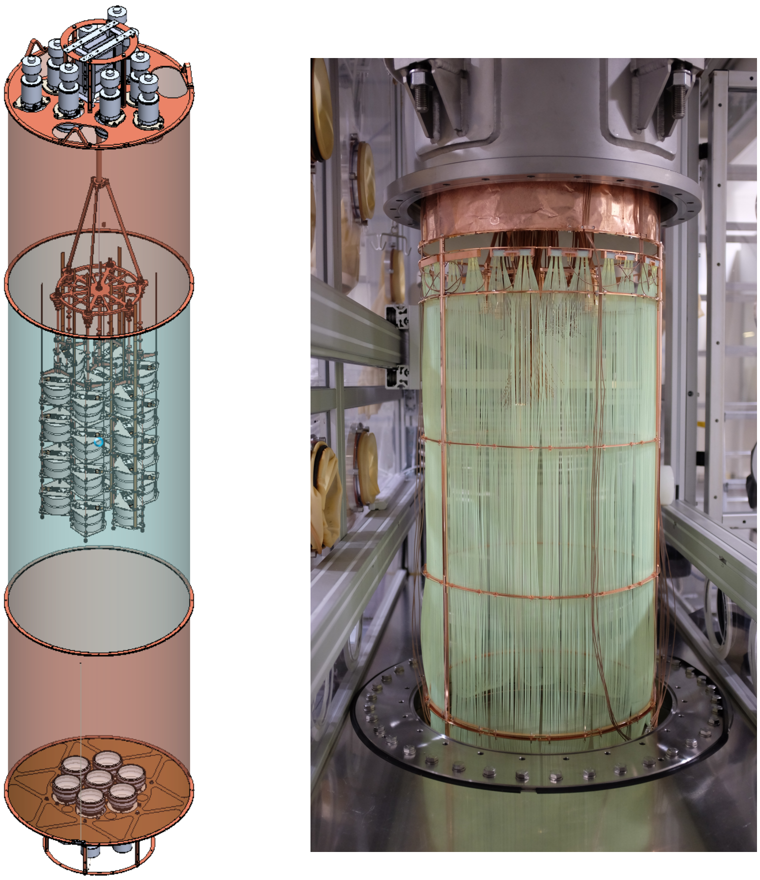

Figure 2.6: Liquid Argon veto design drawing (left) and realized hardware setup (right).

tors (detector-coincidence) is much increased. Identifying these events again reduces the background since only internal electrons (from the $0\nu\beta\beta$ decay) represent a true signal event. In Figure 2.7 a detailed description of the array structure can be found.

2.5 BEGe detectors

Broad Energy Germanium detectors (BEGe) exhibit several features which make them a very good alternative to the usually used semi-coaxial detectors.

- excellent energy resolution of $\sim$0.1 % at $Q_{\beta\beta}$,
- low input capacitance and resulting low noise at low energies,

Figure 2.7: String array of 40 Germanium detectors in Phase II. Left) CAD drawing. Right) 5 of 7 strings assembled and surrounded by transparent shrouds. BEGe diodes are mounted in pairs, four per string and semi-coaxial diodes three per string in the final configuration.

- superior pulse-shape discrimination capabilities due to particular electric field shape.

The mass of the individual diode however is much reduced from more than 2 kg to roughly 700 g. This increases the number of read-out channels and the corresponding electronics significantly per unit target mass. This type of diodes is a customized detector variety available from CANBERRA Semiconductor NV, developed and tested in close cooperation with the GERDA collaboration. It features similar properties as the so-called point-contact detectors, put forward in [69] and used in the MAJORANA experiment.

2.5.1 Design

The dimensions and the mass of a BEGe diode are constrained by the particular electric field required inside the diode after depletion. The electrical field shape in general is determined by the superposition of the space charge in the depletion zone (from the electrical

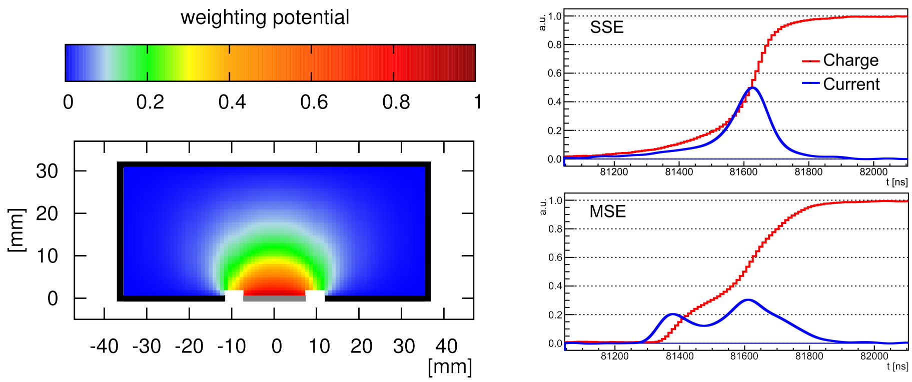

(a) **(b)**

Figure 2.8: a) Broad Energy Germanium detector with calculated weighting potential. **b)** Charge and current pulses resulting from different interaction patterns. Single site events exhibit one peak in the current pulse and multi site events show multiple peaks separated by the respective drift times. From [68].

active impurities) and the chosen electrode geometry. Shown in Figure 2.8a is the resulting potential (weighting potential[1]) peaking sharply close to the read-out electrode. Hole and electron clusters created by an incident particle move along the electrical field lines to the respective electrodes. The charge induced on the read-out electrode by the moving charge carriers is largest in the region with the largest weighting potential according to the well known Shockley-Ramo-Theorem as described in [70] and is given by

$$Q(\vec{r}(t)) = q_{tot}\,\phi_w(\vec{r}(t)). \tag{2.3}$$

Where $Q(\vec{r}(t))$ is the induced charge on an electrode, $\phi_w(\vec{r}(t)$ is the weighting potential of the respective electrode configuration and q_{tot} the total charge.

In p-type detectors mostly holes will contribute to the generation of the signal pulse since electrons travel only through regions of small weighting potential on their way to the outer n^+- electrode. The holes on the other hand always move through a similar weighting potential close to the read-out electrode. Leading to similar signal pulses regardless of the radiation particle's interaction point. Only the drift time of the holes until they reach the high weighting potential region will differ. This results in clearly distinguishable signals when comparing multiple and single interactions as seen in Figure 2.8b.

Due to the small area read-out electrode the capacitance of the BEGe diode is much

---

[1] The so-called weighting potential is constructed such as if one electrode is set to unit potential and no charges are present in the active volume. This potential is unitless.

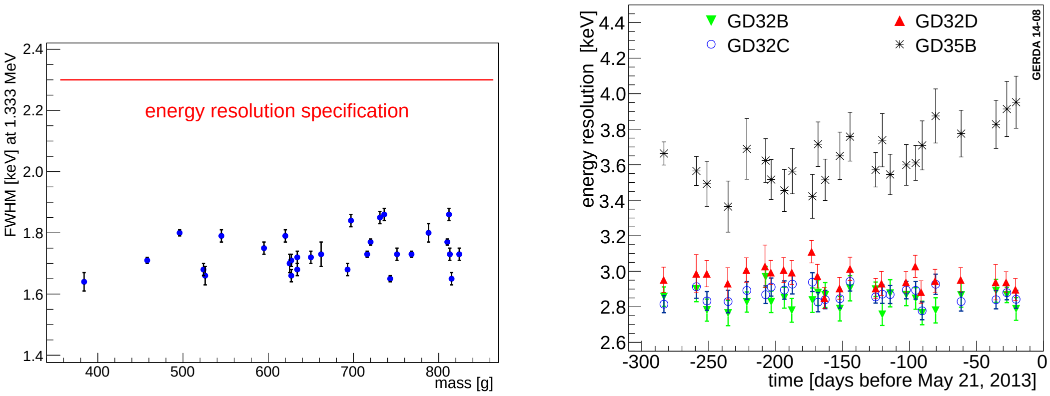

(a) Energy resolution in dependence of detector mass at 1333 keV of all 30 BEGe as measured by the manufacturer.

(b) Energy resolution at 2615 keV in dependence of time for four BEGe detectors used in GERDA Phase I.

Figure 2.9: Energy resolution (FWHM) of BEGe detectors (from [71]).

reduced compared to semi-coaxial diodes. A small detector capacitance (< 1 pF) and comparable amplifier capacitance result in a very low electrical noise level. This is favorable for the energy resolution especially at low energies (see next Section 2.5.2).

2.5.2 Performance

After extensive pre-testing of several prototype detectors (see [72–74]), 30 BEGe detectors, made from HPGe enriched in ^{76}Ge, were produced by the manufacturer. The production and the performance of a detector subset is presented in detail in [71]. Here only a summary is given. As acceptance criteria an energy resolution (FWHM) of < 2.3 keV at 1333 keV, operational voltage ≤ 4 kV and a leakage current of < 50 pA at the depletion voltage were required. Figure 2.9a depicts the individual energy resolutions of all detectors at 1333 keV in dependence of their mass with no correlation observed. Except for one detector, with a deviant impurity distribution, the criteria were met by all 30 detectors. After delivery the detectors were tested underground in vacuum cryostats to gather knowledge about their individual performance, e.g., energy resolution, active volume and pulse-shape. A selection of the performance data of the seven detector subset is given here. The average energy resolution was determined to be 1.73 ± 0.05 keV at 1333 keV and 2.47 ± 0.05 keV at 2615 keV. The active volume, determined by Am measurements, is > 91 % in all seven cases. As mentioned in Section 2.3 five of these detector have been used in Phase I with the energy resolution behavior in time shown in Figure 2.9b. The BEGe detectors show a ~ 30 % better resolution compared to the coaxial detectors. The performance in the GERDA array is worse than in the vacuum cryostats as expected from the electronics configuration (distance) and other noise influences present. The pulse-shape performance also suffers from these influences as described in detail in [68, 71].

2.6 Detector mount

The basic concept of the GERDA experiment is to use liquid argon as shielding material and at the same time minimize the amount of material close to the detectors. Obviously a detector needs cabling, connections to electronics and high voltage and holder structure for mounting. This complete assembly is called detector holder or mounting structure.

In Phase I most of the detector holder was made from radio-pure OHFC copper and PTFE. The materials and its properties used in Phase I and in Phase II will be compared in the next section (2.6.1). As pointed out in Section 2.3.1 a higher than expected contamination of ^{228}Th and ^{214}Bi of unknown origin was found in Phase I. As a preemptive measure a new holder design with new even cleaner materials was designed. Since the individual BEGe diodes also have a smaller mass a decrease of contamination per detector mount was needed to at least keep the same radioactivity per unit detector mass.

To reduce the amount of material per unit detector mass the design features a pair of diodes in one mounting structure. In Figure 2.10 the basic design, its components and used materials are presented. The detector holder consists of three major components: two silicon plates for vertical fixation, three copper rods (legs) for balancing the pair and connection to adjacent detector pairs as well as silicon spacers for fixation against relative motion between silicon plate and diode.

2.6.1 Materials, radiopurity and background contribution

The ansatz for the design was to replace as much copper with the even cleaner silicon. Mono-crystalline silicon is well known to be extremely radio-pure from Neutron Activation Analysis (NAA) [75]. This method is not directly sensitive to the important isotopes ^{228}Th and ^{226}Ra but only to ^{238}U and ^{232}Th. To infer the abundance of the former from the latter secular equilibrium must be assumed. With the heavy processing of the crystalline silicon a breaking of this equilibrium is possible by removal of extremely long lived isotopes or introduction of volatile (radon) isotopes. To constrain this equilibrium breaking an additional γ-spectroscopy measurement (with less sensitivity) is often done.

Silicon does not have very favorable mechanical properties, it is very hard and stiff, very hard to machine and thus cannot compensate for any unintended forces applied to it.

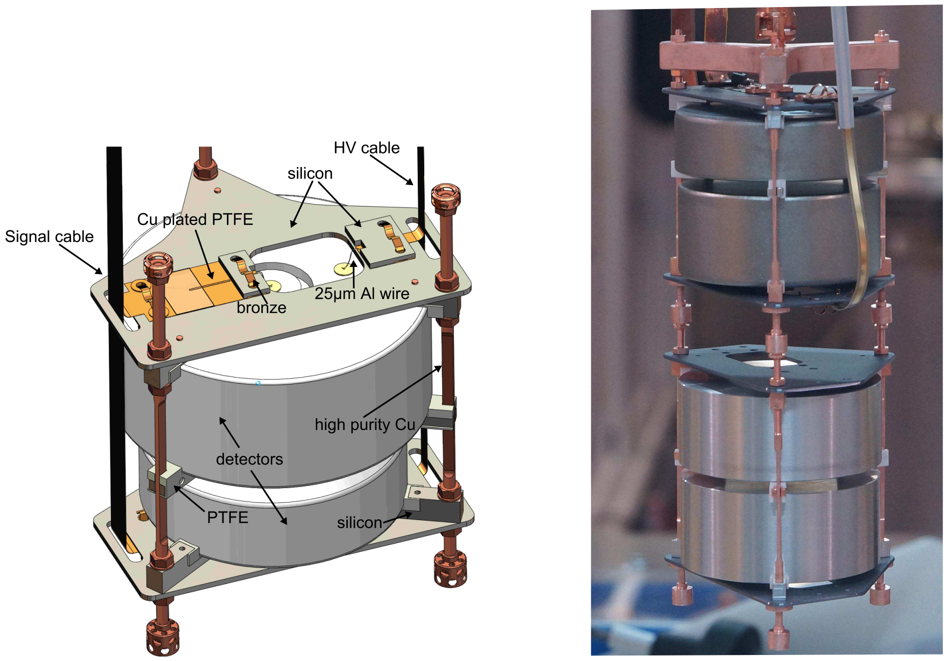

Figure 2.10: **a)** CAD drawing of detector mount. In addition signal and HV cables are drawn here. Two diodes are held in place by silicon spacers lined with PTFE for insulation. Two silicon plates from top and bottom, roughly 5 mm away from the diode, are fixed by three copper rods, or legs, and respective copper nuts. Signal and HV cables are fixed by small silicon bars and bronze springs. **b)** Two pairs of diodes (bottom one are dummies), connected to each other, representing half a string.

The parts where this could happen, e.g., the “legs” and screws, are still made from copper. PTFE was used only where it is needed for electrical insulation. Custom-made bronze from screened copper and 7N tin (usual bronze is often contaminated) was used only in small amounts for the spring fixation of the HV and signal-readout cables. In Table 2.4 the masses, activities and the induced background of the complete detector holder in Phase I and in Phase II are shown.

As can be seen in this table the computed background index (for a coaxial detector) for a Phase I holder is below the Phase II background index goal of 10^{-3} cts/(keV·kg·yr). For one BEGe diode of smaller mass this would have been marginal, so a new holder design optimized for BEGe dimensions was produced. Furthermore the use of silicon plates gives the option to place clean front-end electronics (the resistive feedback part) very close to the diodes, as indicated in Figure 2.10.

The usage of these very radio-pure but mechanically unfavorable materials, especially silicon, made a change of the contacting scheme (signal read-out and HV connection) necessary. A low-activity, reliable contacting scheme was needed and found in the form of ultrasonic wire bonding.

	Material	mass[g]	spec. activity [Bq/kg]		tot. activity [μBq]		BI [cts/(keV·kg·yr)]	
			^{228}Th	^{226}Ra	^{228}Th	^{226}Ra	^{228}Th	^{226}Ra
Phase I	Copper	84	$< 2 \cdot 10^{-5}$	$< 2 \cdot 10^{-5}$	< 1.6	< 1.3	$< 5 \cdot 10^{-4}$	$< 2 \cdot 10^{-4}$
	PTFE	7	$< 2 \cdot 10^{-5}$	$< 2 \cdot 10^{-5}$	< 0.15	< 0.14	$< 5 \cdot 10^{-5}$	$< 3 \cdot 10^{-5}$
	Silicon[1]	1	$< 10^{-9}$	$< 10^{-10}$	-	-	-	-
Phase II	Copper	26	$< 2 \cdot 10^{-5}$	$< 2 \cdot 10^{-5}$	< 0.5	< 0.4	$< 10^{-5}$	$< 10^{-5}$
	PTFE	2	$4 \cdot 10^{-5}$	$4 \cdot 10^{-5}$	0.08	0.09	$7 \cdot 10^{-7}$	$4 \cdot 10^{-7}$
	Silicon	40	$< 10^{-9}$	$< 10^{-10}$	-	-	-	-
	Bronze	1	$< 3 \cdot 10^{-4}$	$< 3 \cdot 10^{-4}$	< 0.3	< 0.3	$< 3 \cdot 10^{-6}$	$< 1 \cdot 10^{-6}$

Table 2.4: Comparison of masses, induced radioactivity and computed background index in Phase I and Phase II detector mounting structure.

2.6.2 Wirebonding as contacting solution

In Phase I contacting of the diodes was achieved by two different methods. The signal (p^+) electrode was contacted with a silicon spring loaded copper cone. The HV electrode was pressed by a copper screw to have a low resistance connection. A torque of average 60 N·cm was needed to achieve this good connection with an acceptable holder deformation of ~ 1 mm. Less massive copper parts were not able to sustain the applied load. The importance of a good electrical connection for the energy resolution is described in [64].

Wirebonding on the other hand does not apply any load on the holder structure except during the bonding process itself. This allows to significantly reduce the amount of copper in the Phase II holder. It was therefore decided to investigate the possibility of wirebonding the large volume germanium diodes for the usage in Phase II. Questions to be answered were reliability of such contacts in cryogenic liquid, during thermal cycling as well as handling. A reliable, ohmic contact could potentially improve the energy resolution. That this is the case is shown in Section 8.1. Necessary modifications to the diodes were also investigated and conducted. As will be shown in Section 6.1.4 wirebonding is also a radio-pure method because, among other things, it uses tiny amounts of material of the order of μg. An introduction to wirebonding and its requirements in GERDA Phase II is given in Chapter 3. A complete description of the diode modification development and the conducted processing is presented in Chapter 4. At last the performance of such modified and contacted detectors is shown on the basis of extensive Phase II commissioning runs and the subsequent physics data taking (Chapters 7 and 8).

---

[1] activity values from NAA, assumes secular equilibrium

Chapter 3

Wire bonding large volume germanium detectors

The process of wire bonding and its application in the GERDA experiment is presented in this chapter. Although wire bonding has long been used in contacting research and commercial silicon detectors it is not usually used to contact large mass and volume germanium diode detectors. First an introduction of theory of wire bonding and the working principle is given (Section 3.1), then the special requirements on wire bonding in the GERDA environment will be shown (Section 3.2). This is followed by a description of the used bonding equipment (Section 3.3) and possible bond failures modes (Section 3.4). Finally, the design and development of a reliable bonding process is presented in Section 3.5.

3.1 Working principle and bonding theory

A comprehensive overview of the field of wire bonding can be found in [76]. Here, only certain aspects (materials, specific bond process, etc.) important for the further work are presented. Wire bonding can be described as a process where two metals are joined by cold welding. This means no liquid phase is present during the joining process. The bonding process used most widely is ultrasonic (US) wire bonding where an US pulse and pressure is applied to the to-be joined metals. Other varieties use in addition heat (thermosonic, used usually with gold wires only) or only heat and pressure (thermocompression bonding, also usually used with gold wires only). In Figure 3.1 a typical bonding sequence is explained in more detail.

A basic overview of the bond forming with the application of an ultrasonic pulse and

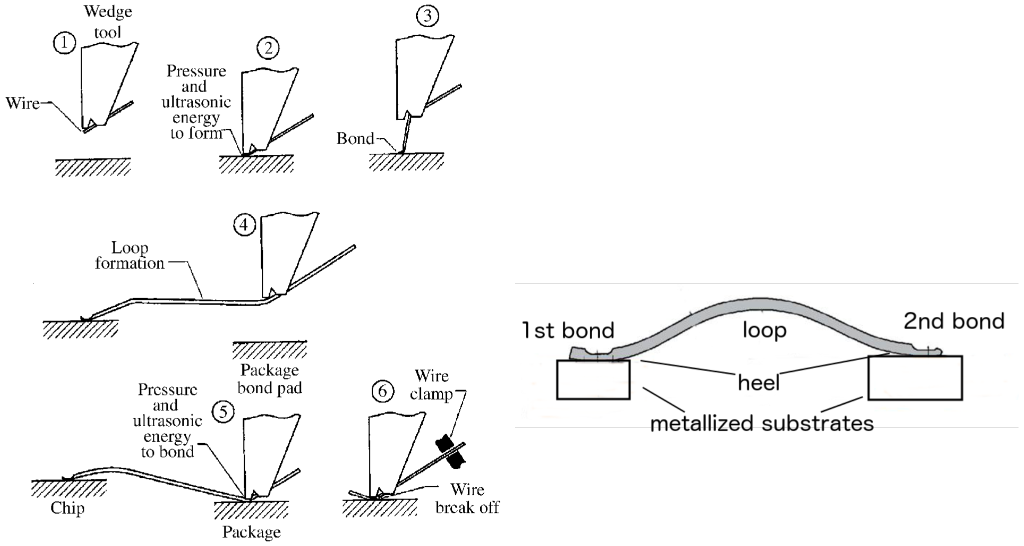

(a) **(b)**

Figure 3.1: a) Ultrasonic wedge bonding process steps. 1. Positioning of tool. 2. Application of pressure and US pulse to form 1st bond. 3. Moving the tool to loop height. 4. Moving towards 2nd bond site while forming specific loop geometry. 5. Making 2nd bond. 6) Fixing wire with respect to tool with clamp while moving tool upwards. Wire breaks at weakest point (behind 2nd bond head). From [77]. **b)** Loop geometry showing selected parts of bond connection.

pressure is given here, for more details see [78]. A combination of an ultrasonic pulse and applied pressure softens the metals (reversible ultrasonic softening [79]) and deforms them. At the same time the relative motion (due to the US pulse) leads to wear of the to-be bonded metals (and contaminants, including the break-up of oxides). This wear is commonly called "fretting". Small tangential forces (due to the US pulse) cause the periphery of the touching metals surfaces to go into the so-called micro-slip regime [78, 80] and a (weak) weld i.e., bond is made. If the tangential forces are larger (corresponding to more US power applied) the entire area of the touching surfaces will go into the gross sliding regime, making a stronger bond with a larger welded area. This dependency on the US power is depicted in Figure 3.2.

A careful selection of the to-be bonded metals is necessary since the individual material hardnesses, oxide thicknesses and elasticities all play an important role in the success of the bonding process. Two examples of how these parameters influence bonding are given in the following. Oxide layers can inhibit the bonding process if they are not broken up and pushed away during the bonding process. Here, the ultrasonic pulse is crucial for the ability

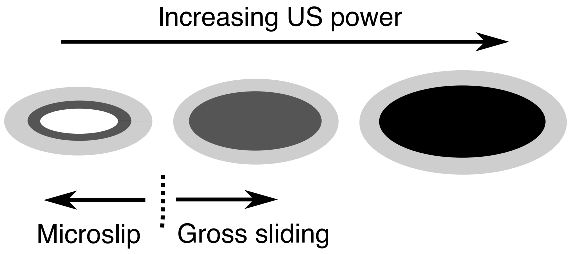

Figure 3.2: Schematic of the evolution in bond footprints with increasing US power (larger tangential force). Shaded areas indicate fretting (start of bond forming) with darker shades meaning stronger bonded areas.

to bond fast oxidising metals such as aluminium or copper. A high elasticity substrate metal will be partly pushed away by a harder wire metal which leads to cratering and form an irregular bond because the pressure is not evenly distributed. Most commonly used are wires from aluminium, gold and recently also copper [76, p.51ff.]. For substrates there is a bigger variety, where also the materials below the metallization play an important role for successful bonding as will be explained in Section 3.4. Here as well, gold and aluminium are most common for the metallization of bond pads [76, p.131ff.] (see also Chapter 4). Different material combinations are used to fulfil the specific requirements on the bonding process, e.g. speed, low costs, pitch, ultimate strength and/or (corrosion) robustness. The specific requirements in the context of GERDA are discussed in the next section.

3.2 Requirements in GERDA Phase II

Unlike industrial wire bonding or the large scale application in silicon detectors for the ATLAS and CMS experiments, speed, pitch (i.e., area needed per bond) and low costs per bond are not relevant for the GERDA experiment. The total number of connections to be made for the complete Phase II setup is on order of 100 which is very small compared to usual applications (see above). The requirements on the bonding process are:

- Survival of handling during mounting and immersion of the detectors in cryogenic liquids this corresponds to a high bonding strength.
- No damage to the extremely sensitive p^+- electrode on the diode during bonding (see Section 2.2.1).
- Small background contribution (i.e., small mass and radio pure materials).

- Bonding in glove box to protect diodes from oxygen (see Section 2.2.1).
- High voltage (up to 4kV) must be applied to diode via bond wires.
- Large looping, long bond wire ($\sim$1 cm) and large height difference ($\sim$5 mm) between 1st and 2nd bond.
- No application of heat during the bonding process since otherwise a change in the doping profile of the detector electrodes is possible.

A small background contribution was one of the most important reasons to use wire bonding as the contacting solution in Phase II. Per detector bond wires (4×1 cm) with a mass of only 50 μg are used. The requirements above lead to design constraints with respect to the chosen bonding technique and materials used. Gold wire is preferably bonded with heat (thermosonically), but however, since heating up the diode is not allowed, gold was not chosen as wire material. Copper bond wires are used only when reducing the material costs is crucial or for high-power applications. Furthermore, its relative hardness and fast oxidation make it less favorable (see [76, p.74]). Aluminium (with 1% addition of silicon, AlSi1%) is used frequently as the wire bond material of choice. It is relatively soft and its thin oxide layer is easily broken up during the application of the US pulse [76, p.9]. Aluminium has been known for decades to produce reliable bonds on aluminium but can be under certain circumstances problematic on gold metallizations (“purple plague”, see [76, p.131ff]). This is why aluminium was chosen as the metallization material. Applying the diode bias voltage through a thin (25 μm) aluminium wire poses no problem since the maximum current flowing is on the order of nanoampere. In addition it was experimentally verified that the bonding process does not damage the p^+- electrode (see Section 4.3). The large height difference and the necessary use of a glove box posed strict restrictions on the bonding equipment used.

3.3 Bonding equipment

The large distance ($\sim$5 mm) between the diode and the read-out cable on the detector holder (see Figures 2.10 and 3.3, note especially the relatively small rectangular access hole) make a long bond wire and large loop necessary which can only be applied in this small space by a so-called deep-access bonder. In such bonders the clamp is located on top of the bond tool[1] and thus allows bonding in deep cavities (see Figure 3.3) . A semiauto-

---

[1] Freeing the space around the tool

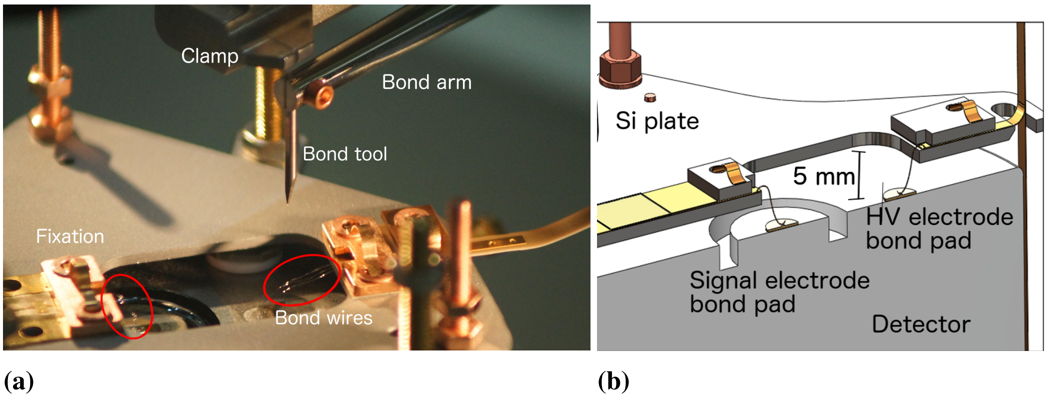

Figure 3.3: Close up of bonding tool, Ge diode, HV cable and bond wires. Note the very long wires and the large height difference.

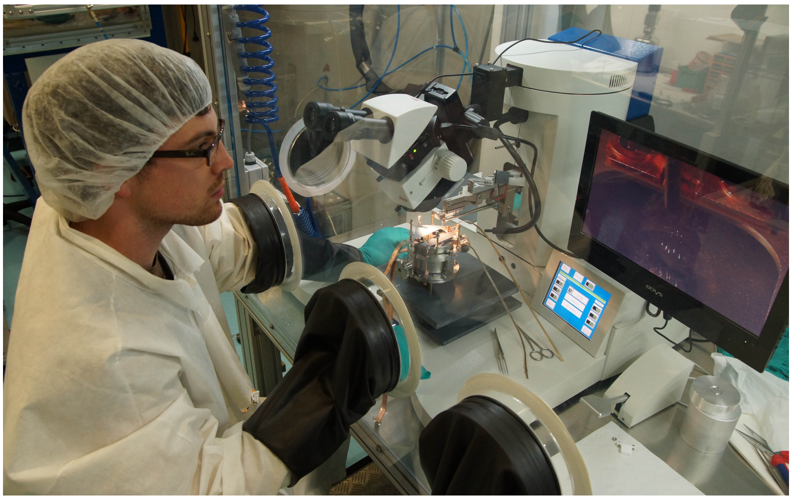

Figure 3.4: Bonding operation in glove box in the Germanium Detector Lab at LNGS

matic, z-axis motorized, deep-access bonder (model HB 10) from tpt Wire Bonder GmbH & Co. KG was selected for bonding. Contrary to usual bonders the movement of that machine's bonding arm are strictly vertical. This as well allows to bond large height differences but leads also to a slightly different bonding behaviour as is explained in Section 3.5. This bonding machine is placed in a glove box constantly flushed with N_2, located in the GERDA Germanium Detector Lab (GDL) at LNGS. It was verified that an operation with thick gloves and limited access to some parts of the machine was possible. A picture of the bonder operation inside the glove box is shown in Figure 3.4.

The wire size was chosen to be a standard 25 μm, made from 99% Al and 1% Si

(AlSi1%), wire with a break load of 15-18 cN procured from the company tpt GmbH. It was screened for radioactive contaminations by ICP-MS and the results are shown in detail in Section 6.1.4 and Appendix A. A negligible background of 10^{-6} cts/(keV·kg·yr) is induced. Thicker bond wire in principle has a higher intrinsic break load but this is partly offset by the significantly higher US power and force required to form the welding. These higher operational parameters could lead in principle to a damage of the p^{+} electrode and thus were not further considered.

3.4 Development and characterization of the bonding process

Assessing the bondability and reliability of the proposed new bond process system was one of the most important tasks in the development of the contacting solution. Since wire bonding provides the (electrical) interface between the germanium diode and the read-out electronics, a reliable bonding process depends strongly on the entire assembly consisting of diode, read-out electronics and holder structure. Changes in one of the individual parts of the assembly can affect the reliability of the total system. Two main issues have to be controlled for a successful wire bonding process: 1) Non-sticking of bonds (low or no bondability) during the bonding itself and 2) Bond failure at any given time. These two are discussed in the following sections.

3.4.1 Bondability

The ability to form a reliable bond consistently is called bondability. If the bondability of the to-be bonded system (i.e., wire, metallization, underlying substrate and support structure) is low (or non-existing) the attempt in forming the bond (i.e., the weld) will fail. The force applied on the bond by moving the wire to the 2nd bond site or by breaking the wire after the 2nd bond is larger than the pull strength of the bond which results in a lift off (see next section). Several factors play a role in bondability. These are, e.g., hardness (matching) of the to-be bonded metal surfaces, oxide (if existing) hardness, contaminations of the surfaces, brittleness or softness of the underlying substrate, and the fixation of the substrate. (For an extensive list see [76, p.8ff.]). A change of one of these factors can significantly influence the bondability of the complete system. Controlling these factors is thus paramount for a successful bonding process. If the system is initially found to be bondable the next aspect to verify is the reliability of the bonds under stress.

3.4.2 Bond failure modes

Bond failures can occur under stress if the forces applied to the bonds are larger than their bonding strength. Usually this strength can be quantified via “pull testing” according to MIL-STD 883 method 2011 [81]. A hook which is connected to a force meter is put under the wire and is pulled upwards until the bond fails. The location (i.e., lift off, heel or wire break) of the failure and the force required are recorded. The minimal pull force a bond should survive is given by the norm MIL-STD 883 and is approx. 3 cN for 25 μm Al wire (with a break load of 15 - 18 cN). Any further specification must be made by the process designer. Bond failures can be characterized into two modes. Wire breaking, either at the bond heel or in the loop, and bond lift off from the metallization.

Bond lift off shows that the weld between the bond wire and substrate metallization is not sufficiently strong or incomplete. As discussed in Figure 3.2 further increase of the bonding parameters might be necessary. If wire breaking occurs above the minimal specified pull force the bonding process passed this test (if the result is reproducible). If the wire breaks at the heels (either at the 1st or 2nd bond) with low forces applied, the wire was very likely deformed to much and weakened by the bonding process (too high US power and/or pressure) itself. Such wide and flat bonds are referred to as “overworked” bonds. The interplay of these two failure modes is visualized in Figure 3.5. The optimal range of bonding parameters (where no lift offs occur and the pull strength is sufficiently high) should be identified for reliable bonding. Preferably this region is not too small in the bonding parameter space (process window). Since otherwise small, uncontrolled changes in the bond system will lead to unreliable bonds and consequently to reproducibility issues.

When designing the bond process the ability to form a bond (without lift off) as well as the resulting bond strength must be balanced.

3.5 Specific design of bonding process

It is well known that AlSi1% wire and Al metallization as substrate match in hardness and that the oxides are brittle and are broken up during the bonding procedure. This results in very good bondability (see [76, p.29 & 37]). For this and several other reasons (see Section 3.2) the Al-Al bond system was chosen.

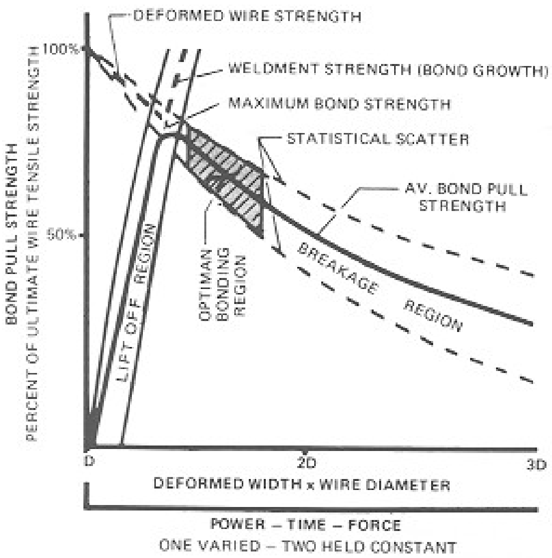

Figure 3.5: Bond pull strength vs. bonding parameters (power, time and force). Two regions according to the failure mode (lift off or breakage) are identified. Maximum pull strength is found at the intersection of the two regions. The optimal region with high pull strength and best reproducibility is located shortly after this point. From [82].

1st bond on electrodes of germanium diode

The next step is to check the bondability of the system including the real substrate, the Ge diode. The diode features two different substrates, the boron implanted p$^+$- electrode and the lithium diffused n$^+$- electrode. As described in Section 4.3.2 the lithium diffused germanium substrate is very brittle and can be broken during bonding leading to so-called "cratering" (see [76, p.249]). This was prevented by polishing the uppermost layer of the lithium doped germanium. In contrast the boron implanted surface showed no problems of such a kind. A detailed description of the metallization process and the tests conducted for its characterization is given in Chapter 4.

2nd bond on flexible cables

The site of the 2nd bond is a flexible cable which connects to either the read-out electronics or to the HV supply. These cables were designed and supplied by the GERDA electronics subgroup with a special attention to ultra-low radioactivity. In Figure 3.6 a picture of such a cable and a schematic of the substrate layer structure are presented. The cable head is fixed by a bronze clamp and a holding piece on the underlying silicon plate.

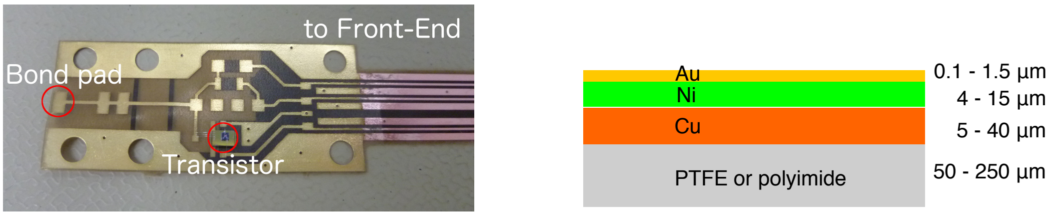

(a) Flex cable head for connection of p^+-(signal) electrode with attached transistor. Golded parts are prepared for bonding.

(b) Flex cable layer structure (crosssection) with materials and various thicknesses used.

Figure 3.6: Flexible cable layout and layer structure.

The base layer is either PTFE or Kapton (polyamide) with a copper layer as trace applied to it. For bonding a plated nickel layer is usually used. Oxidation of this nickel would inhibit bondability and therefore a thin gold layer finishing is made (see [76, p.201]). Several designs were tested which differed in radiopurity, (base) layer thicknesses, finishings, varieties of plating processes and suppliers. The simplest design consists of just a copper trace on a base layer. This was found to be in general radio pure (due to the few processing steps and materials used) but exhibited low bondability and large variation among batches and suppliers. The more complex design described above showed higher background with large variation among base layer materials, batches and suppliers. The bondability was higher but again with a large variation and inconsistencies among the different thicknesses of base layers and suppliers. Several factors could be identified which had an impact on the bondability: Low bondability was accompanied by a small process window, therefore decreasing the reproducibility. Thin, flexible base layers ($< 100\,\mu$m) move (give in) during the application of the bonding force which is worsened by a bad/unreliable fixation of the cable head by the bronze clamps. A thick, stiff base layer prevents this to a certain extent. A thicker nickel layer improves bondability significantly. A likely reason is the higher elastic modulus (compared to copper) which “gives the Ni layer a high potential to resist deflection and absorb energy during the ultrasonic application and downward force applied to the bond pad[..].” [76, p.201]. A similar but less pronounced effect was achieved by the increase of the copper thickness ($> 30\,\mu$m) which then could be bonded even without Ni/Au plating. Lastly some batches of cables were found to have darker gold finishing layer with resulting very low bondability. This behaviour is attributed to a highly porous gold layer through which the nickel diffused and then oxidized. This is a common cause for low bondability (see [76, p.208f.]).

Another factor decreasing the successful bonding rate on the 2nd bond site is related to the type of bonding machine used (see Section 3.3). The deep-access bonder breaks the wire directly behind the 2nd bond by moving the arm and the bond tool strictly vertical. This applies a high vertical pull force on the 2nd bond. If the transition region of bond foot to the wire is not weakened enough the breaking occurs not in this region but between the bond and substrate. This results in an immediate lift off and an apparent low bondability. The requirements on the bonding strength at that time can be higher than during the following use of the bonded detector assembly. Since the deep-access bonder is indispensable in the GERDA specific detector-to-cable bonding system has to be compensated by well bondable cables.

Bond pull strength tests were performed on bond connections made only on the flex cable head to assess the bond quality. High pull strengths up to 15 cN were achieved when the bondability was high which were also accompanied by a large process window. In this case, the force and US energy could be reduced to a minimum while still giving a well formed bond with good welding to the substrate. The bonds failure mode varied between lift off and heel break. Samples with small process windows and low bondability showed lower to non-existent pull strengths with bond failures at the heel, from 0 - 8 cN, depending on the amount of bond over-working.

Due to radio-purity constraints for the final assembly of the GERDA detectors, cables with medium bondability and sufficient pull strength ($\sim$5 - 8 cN) were chosen. As discussed in Section 7.1.2 this pull strength was found to meet the robustness requirements of the contacting solution. During the commissioning detector array immersions only 0.3 % (2 of 760) of the bonds broke while in the final immersion no faulty electrical connection occurred. This shows the reliability of the developed contacting solution. For wire bonding on the detector a well bondable metallization needed to be applied on the detector electrodes. This metallization process and its testing is described in the next chapter.

Chapter 4

Detector metallization

The detector metallization constitutes the interface between the diode and the bond wire. In this capacity it is usually called bond pad. Good quality detector metallization is needed for a strong bonding contact and protection of the sensitive signal electrode. In addition the electrical contact between metallization and the semiconductor surface must be ohmic to neither deteriorate the signal (on the p^{+}- electrode) nor impede the high-voltage applied (on the n^{+}- electrode). A further complication was to prepare a metallic thin film on an already produced commercial detector where the surfaces are not optimized for subsequent metallization. The work was structured in the following way:

Each step will be discussed in the following sections. Several requirements (Section 4.1) are shown in this chapter. Furthermore a typical metallization process is presented (Section 4.2). Prior to the complete metallization processing of the enriched Ge-detectors several tests were performed to ensure the quality of the metallization (see Section 4.3). At the end of this chapter an overview of the metallization processing of the enriched detectors is given (see Section 4.4).

4.1 Requirements

The detector metallization has to meet various requirements to be acceptable for an ultra-low background experiment like GERDA. As described in Section 3.2, aluminium was chosen as bond wire material which consequently is also the preferred material for the metallization according to the literature [76].

4.1.1 Reliability and bondability

The nature of rare event search experiments requires highly reliable detector contacts since failing contacts cannot be repaired during the running experiment without causing significant delays. The metallization and also the wire bonds must exhibit high stability under several thermal cycles and handling. Additionally the metallization process must have a highly reproducible outcome. If a problem in a subset of detectors is found later at the experiment site a partial reprocessing would lead to extensive logistics and possible delays of the entire experiment. The bondability (the ability to form a strong, reproducible bond on a substrate) is strongly influenced by the quality and surface preparation of the metallization. Bondability and reliability are reduced by the following factors (for more details see also Section 3.4):

- Bad adhesion to the underlying surface can inhibit bonding completely or lead to delayed lift-offs.
- Rough and/or dirty surfaces result in incomplete forming of the bond and consequently to a low/non-existent pull strength.
- Rough and brittle underlying surfaces (e.g., the lithium doped n^+-electrode) can break up during bond force and US power application.

Consequently, a well prepared metallization with good film adhesion is needed to ensure reliable bonding.

4.1.2 Radiopurity

Paramount in the context of rare event searches is the use of radio-pure metallization materials and the cleanliness of the deposition technique. Aluminium as a deposition material is available in different purities. For evaporation 6N (99.9999%) material is commonly used. The general level of impurities thus is low. To quantify radioactive impurities a dedicated screening must be performed. Aluminium varieties that are known (screened) to be radiopure, such as Kryal, Highpural [83], used mostly for detector cryostats, are not directly usable as evaporation material since the amount of enclosed oxygen prevents an evaporation with a resulting good quality metallization (i.e., adhesion and ohmic behaviour). Since the amount of aluminium available was only on the order of grams, an ICP-MS measurement (inductively coupled plasma mass spectroscopy [84]) for the isotopes ^{238}U and ^{232}Th was performed with the results shown in Table 4.1. To quantify the amount of

Material	^{232}Th conc.	^{238}U conc.	calc. ^{228}Th activity	calc. ^{226}Ra activity
MaTecK 6N	< 0.5 ppb	< 1 ppb	< 60 pBq/det.	< 320 pBq/det.
Balzers 4N	50 ppb	35 ppb	11 nBq/det.	22 nBq/det.

Table 4.1: ICP-MS results and calculated activities per detector (40μg of material) for two different aluminium qualities. Relative uncertainties are approx. 30 % and limits are 95 %C.L. [84].

background-contributing ^{228}Th and ^{226}Ra secular equilibrium is assumed. This equilibrium can be substantially broken (especially in the ^{238}U chain due to several extremely long-lived daughter isotopes) by material processing steps. An assessment of the activity of the potentially background inducing isotopes ^{26}Al and ^{22}Na was not performed but a value of 1 mBq/kg can be assumed (see [83]). For a background estimation due to these isotopes see Section 6.1.4. In Appendix A a comparison of a γ-spectroscopy measurement and ICP-MS results is given. A conservative limit on the activity of the metallization in the GERDA experiment is presented in Section 8.2.2.

As can be seen in Table 4.1 the activity introduced by the metallization is extremely low. The background index contribution of the entire contact solution (metallization and bond wires) was studied in dedicated Monte-Carlo simulations as described in Section 6.1 and found to be several orders of magnitude lower than required for Phase II.

The chosen deposition technique as well as a clean working procedure play an equally important role for the final radio-purity of the metallization which will be presented in the following sections.

4.2 Metallization process

In this section an overview of the chosen thin film deposition technique and its apparatus is given. A typical process and its parameters are presented as well as how the process was integrated into the production of Ge-diodes at Canberra Semiconductors NV, Olen Belgium.

4.2.1 Film deposition theory

Applying a thin film onto or coating a surface can be performed in several ways. Standard mechanical or galvanic coatings were not considered for use in GERDA since they easily could damage and/or contaminate the diodes. Less intrusive methods are sputtering or evaporation of the thin film material. Thermal evaporation of aluminium via resistive heating tends to have controlling issues due to excessive wettability [85] and was not further considered. Sputtering uses accelerated ions to bring the material into the vapor phase which in turn produces the thin film and has its main advantages in depositing alloys and compounds but uses a working gas (usually argon) which under certain circumstances can be incorporated into the film [86, p. 265]. Evaporation of a single material via an electron-beam produces high quality films with good adhesion when the substrate is properly prepared. Due to the point-like heating a metallurgical reaction between the copper crucible or its co-evaporation is highly unlikely and thus possible contaminations are much reduced [87, p. 344]. The chosen metallization material aluminium can be easily and effectively evaporated since it has a low melting point of 933 K [87, p. 339]. The injection of heat is performed by means of an electron beam. The beam is generated by a glowing cathode, shaped through magnetic and accelerated with electric fields. It is then directed to the material to be evaporated which rests in a crucible. The evaporated material forms an atom cloud with a thermal velocity distribution. The atoms adsorb with a certain probability on all surfaces and over time form the thin film on the substrate. A more detailed description of mechanism of film growth is given in [86, p. 710]

4.2.2 Evaporation machine setup

The evaporation machine used for metallization of the Ge-diodes is a Leybold LAB 500. Its main components are:

- high-vacuum ($p < 10^{-7}$ mbar) chamber,
- electron beam generator Leybold ESV 6,
- material depot in a water-cooled crucible,
- film deposition rate monitor by means of an oscillating quartz,
- low energy argon grid less ion source Commonwealth Mark I.

A schematic sketch (Figure 4.1) shows the arrangement of the various components.

High vacuum is needed so that the evaporated atoms are not obstructed by residual gas atoms and to avoid oxidation of the hot material. The used electron beam generator has a deflection magnetic field guiding the electrons onto the aluminium filled copper crucible. The water cooling is necessary to quickly dissipate the incoming heat.

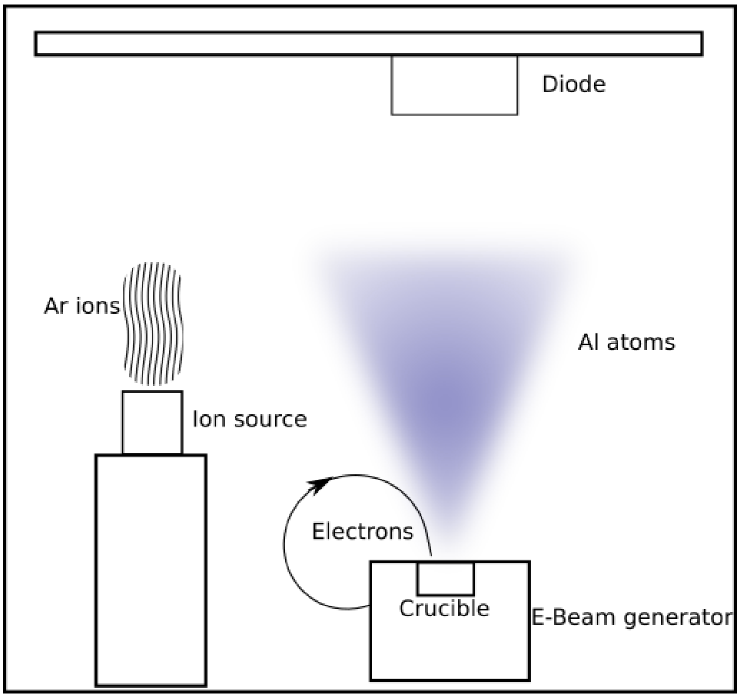

Figure 4.1: The e-beam generator (or gun) sits below the substrate (in this case a diode) and the evaporated atoms form a cloud above the crucible. The electrons are directed via magnetic fields towards the crucible. The diode can rotated such that it is either above the ion source or the e-gun.

The gridless ion source directs ions onto the substrate to “dry-etch”/clean the surface prior to deposition. This low energy sputtering of the surface improves the adhesion of the subsequent deposited film, removes contaminants and decreases possible contact resistances by removing non-conducting surface species [87, p. 422]. An advantage of the gridless feature is that no new contaminants from the grids are sputtered onto the substrate. The low energy of the ions ensures that no damage is done to the crystal structure of the thin p^+- doped signal read-out electrode. Since the cleaning is done in-situ no recontamination takes place. Additionally during the use of ion beam cleaning, in contrast to conventional plasma cleaning, the contaminations are ejected at normal incidence away from the substrate, making recontamination much less likely [88].

The most important parameters of the complete thin-film deposition process are the following: Chamber vacuum, ion energy for sputter cleaning, ion current and sputter time, deposition rate and final film thickness. The chamber vacuum must be below 10^{-5} mbar for the operation of the e-beam. Lower pressure ($< 10^{-6}$ mbar) gives more stable opera-

Pressure [mbar]	ion energy [keV]	film deposition rate [Å/s]	film thickness [nm]
$\approx 5 \cdot 10^{-7}$	40	3	600

Table 4.2: Typical values for the most important evaporation process parameters. The pressure is the background pressure prior to deposition.

tion and less gas incorporation into the thin film. The ion energy should be high enough to sputter off surface impurities [86, p. 117] but not too high as this could damage the diode. The ion current density and the sputter time govern the amount of material removed. The deposition rate and the residual atoms in the vicinity of the substrate influence the regularity, adhesion and contact resistance of the film. A too high rate can potentially result in irregular porous films which can oxidize and influence the contact resistance. A too small rate at normally sufficient vacuum would lead to high incorporation of residual species, e.g., water, oxygen or argon. In general the bondability of the film is influenced by this as well as the final film thickness, which also gives the diode (especially the p^+- electrode) protection against the bonding forces applied. In Table 4.2 a selection of typical values for the most important process parameters is given.

4.2.3 Integration of process at the manufacturer

After the general description of the system and the preferred process parameters in this section the specific developed metallization process, including the diode preparation, is presented. The process itself was carried out in close cooperation with the diode manufacturer, CANBERRA Semiconductor NV.

During prior tests it became apparent that a careful preparation of both the boron implanted p^+ as well as the lithium diffused n^+- surface are necessary (see Section 4.3). The smooth implanted surface needed to be cleaned of organic (glue) residuals of earlier production steps with an acetone wipe. In contrast the lithium diffused germanium surface was found to be very rough as well as brittle and bonding on the untreated n^+ - electrode was not reliable. The remedy is to polish and remove some 100 μm of the lithium diffused surface. Afterwards an etch with a HF:HNO_3 solution was performed for even higher smoothness. The processing time is about three hours for each diode including preparation, pump down and final testing. This short time minimizes exposure times to cosmic rays above ground and fits well with the restricted access times of the underground storage facility.

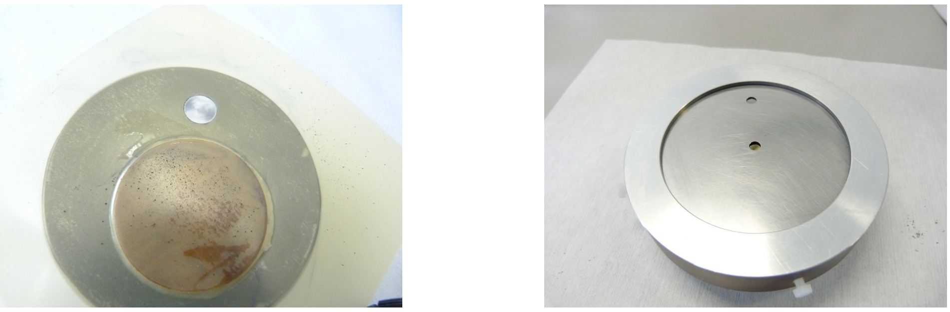

(a) Polished and etched n^+ -surface, while the rest of the diode is protected by adhesive tape.

(b) Diode mounted in evaporation holder and masked by aluminium alloy shadow mask

Figure 4.2: Exemplary steps of diode preparation

Arrival

- Transport of diode from underground storage area.
- Perform a current-voltage measurement (leakage current test).

Preparation

- Remove the passivation layer (see Section 2.2.1) via wet etching.
- Clean p^+-electrode with acetone.
- Polish and etch small part of n^+-surface (see Figure 4.2a).

Metallization

- Mask diode and build into evaporation holder (see Figure 4.2b).
- Pump to vacuum of $< 10^{-6}$ mbar.
- Sputter clean with ion source for $\sim$5 min.
- Evaporate aluminium with a rate of approx. 3 Å/s.

Finalization

- After cool-down, take diode out of machine.
- Wet-etch the groove.
- Perform leakage current test.
- Pack diode into vacuum transport container and return transport.

4.3 Testing the metallization

Since a metallization of the existing highly doped germanium surfaces (boron and lithium as dopant material) had not been performed by the manufacturer prior to this work a detailed feasibility study had to be conducted.

Questions to be addressed were:

1. How good is the adhesion to the underlying surface of either boron implanted (B-Ge) or lithium diffused (Li-Ge) germanium?
2. Does the metallization (as the interface between the bondwire and the doped germanium) constitute an ohmic contact?
3. Does the detector work after the metallization (no damage to sensitive p^+- contact)?

Testing the metallization procedure was performed in several steps. Different germanium test samples allowed to answer questions 1 and 2 (Section 4.3.2). Later a small test diode was used to verify the operational capability (Section 4.3.3). Finally, real diodes of the BEGe type used in GERDA were extensively operated, mounted in the real diode holder structure, in a test cryostat and finally in the GERDA cryostat (Section 4.3.4).

4.3.1 Test procedures

Adhesion of the metallization was directly tested in two ways. First the so-called “sticky-tape test” where a sticky tape is applied to the film and then removed. When adhesion is very bad, already then some parts of the film are removed (see Figure 4.3a). A second test is to check adhesion via bonding. If the metallization lifts from the underlying substrate during bonding or during a bond pull test, film adhesion is not high enough (see 3.4.2). A more indirect indication would be cracking or flaking of the film after repeated immersion in a cryogenic liquid (e.g., LN_2).

Ohmic contact behaviour can be tested by measuring a Current-Voltage curve (IV-curve), similar to a characteristic curve in diode testing (see Figure 4.4). An ohmic contact would show a linear behaviour. The voltage is applied between two evaporated contacts on the highly doped surface of the sample which is held at cryogenic temperatures. On a intrinsic semiconductor this test is not possible.

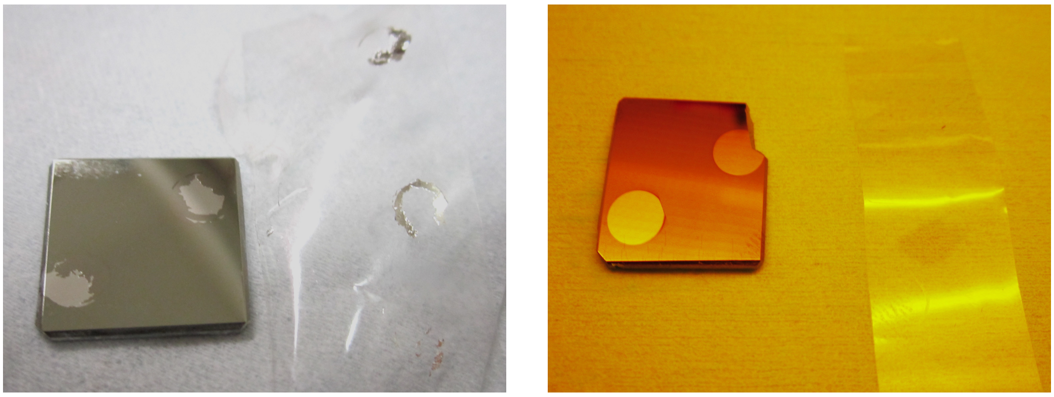

(a) Unsuccessful sticky tape test due to bad edge masking

(b) Result of successful sticky tape test

Figure 4.3: Examples of sticky tape tests

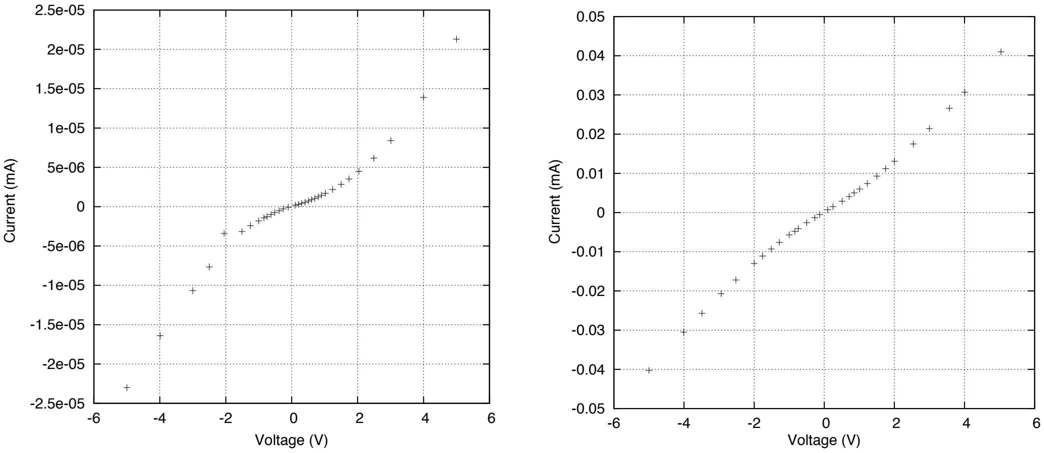

(a) Non-ohmic I-V curve of a Li-Ge sample taken at 77K

(b) Ohmic-like I-V curve of a B-Ge sample taken at 77K

Figure 4.4: I-V curves taken with different samples. When the voltage is applied along the highly doped surface, an ohmic curve should be the result. Deviations from this behaviour imply a problem with the doping or the interface between metallization and doped semiconductor.

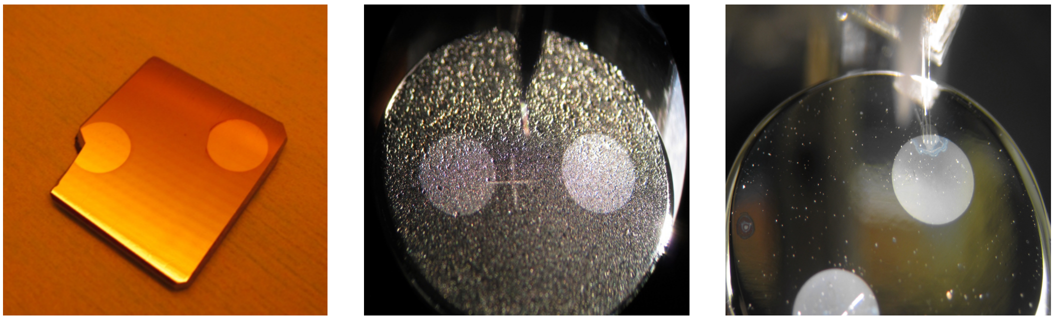
(a) Intrinsic high purity germanium **(b)** Lithium doped sample **(c)** Boron doped sample

Figure 4.5: Three different types of germanium samples used for testing the metallization and bonding behaviour. Aluminium was evaporated on as bond pads on all samples.

4.3.2 Tests with germanium samples

Lithium and boron doped germanium samples were procured directly from Canberra Semiconductor NV which had the same high purity and doping applied as the real diodes. Figure 4.5 shows different samples and their surfaces. As can be seen the as-received lithium doped (Li-Ge) germanium has a very rough surface in contrast to the polished intrinsic[1] or boron doped germanium. A first test metallization on Li-Ge was conducted at CNRS Orsay at the local EDELWEISS group, which usually uses polished intrinsic germanium. The films were prepared by e-beam evaporation. Adhesion to this surface (after short ion sputtering) turned out to be very good and the contact resistance was comparable to the pressing contact as in Phase I.

During this extensive testing non-ohmic behaviour of the interface at liquid nitrogen temperatures was found for these samples (I-V curve in Figure 4.4a). As verified by the manufacturer this was due to insufficient lithium doping of the surface. Consequently new Li-Ge samples were procured. These samples exhibited an rougher and extremely brittle surface. Adhesion was lower and more importantly performing a stable bond was not possible. The brittle and rough surface seemed to break during application of the ultrasonic energy while bonding (see Section 3.1). The solution was to remove a thin layer of Li-Ge by polishing and applying a wet etch afterwards for further smoothening (see Figure 4.6). This removed the rough and brittle surface without affecting the doping profile.

On the boron implanted samples adhesion and bondability were found to be very good without any additional treatment, which otherwise would have been problematic due to the

---

[1] Ultra-high purity p-type germanium without any doping applied

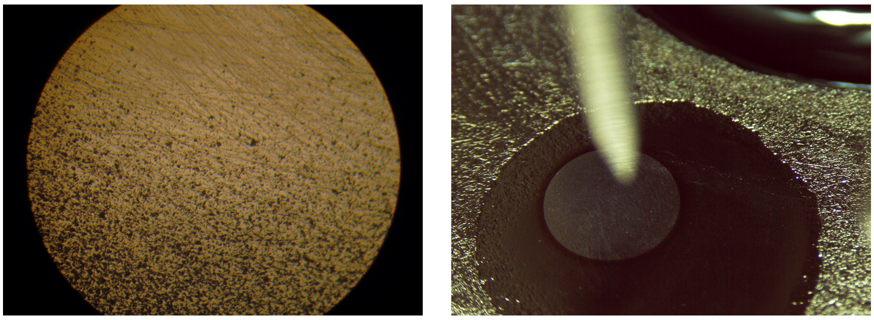

(a) Difference in surface roughness of polished (upper half) and non-polished (lower half) Li-Ge under microscope

(b) Polished and etched Li-Ge surface

Figure 4.6: Smoothening of Li-Ge surfaces for reliable bonding.

thinness of the doped layer. On these samples further tests were conducted to verify the non-damaging nature of the evaporation and bonding procedure. I-V curves (Figure 4.4b) were taken and an ohmic contact behaviour at cryogenic temperatures was found. This was not the final verification but gave confidence for further tests with real diodes.

4.3.3 Tests with a small test detector

In parallel to the tests conducted with the Ge-samples a small but fully functional test diode was procured. The layout of the signal contact region, including the dimensions of the groove, were the same as for real BEGe detectors. A photograph is shown in Figure 4.7a. To be tested, were handling before, during and after evaporation, leakage current after evaporation and bonding and overall functionality as a radiation detector. The preparation and evaporation process of the diode was similar to the evaporation procedure described in Section 4.2.3, except that no polishing and etching of the Li-Ge surface was done since the importance was not known at that time. Another difference was that the passivation layer (allowing handling in air) was not removed. After reception from the manufacturer it was verified that the diode had no increased leakage current (LC) prior to the metallization and bonding procedure. The electrode metallization was performed (see Figure 4.7b) and afterwards the diode was mounted in a custom-made holder with the HV connection made via bonding and the signal connection made at first with a pin (see Figure 4.7c). Again a test for increased LC was negative. As a final test also the sensitive signal electrode (p^+-doped) was bonded and still no increased LC was evident. After this successful tests, the diode was brought (mounted and bonded) to the Germanium Detector Lab (GDL) of the GERDA collaboration at LNGS and operated in a liquid argon test stand (see. Figure 4.7d).

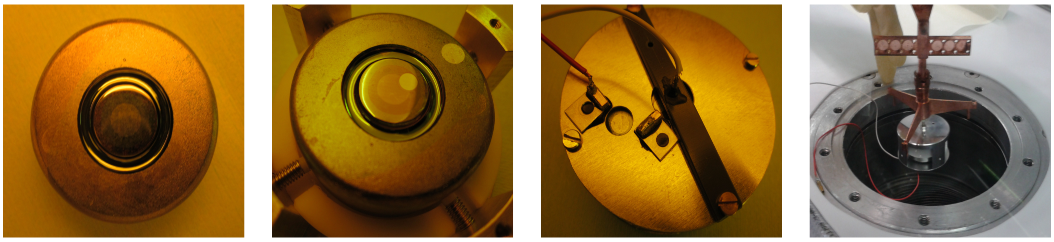

(a) As-received test diode

(b) With bond pads evaporated

(c) Contacted with pin (signal,center) and bond (HV,side)

(d) Submersion in liquid argon

Figure 4.7: Sequence of test diode modification

The first spectrum taken with the bonded large volume germanium detector is presented in Figure 4.8. The energy resolution at 2.6 MeV was determined to be ca. 2.7 keV, showing that the bonding does not worsen the energy resolution. The principal feasibility of the contacting solution was thus proven. The next step was to use this method for a large size BEGe mounted in a GERDA Phase II holder assembly (see Section 2.6).

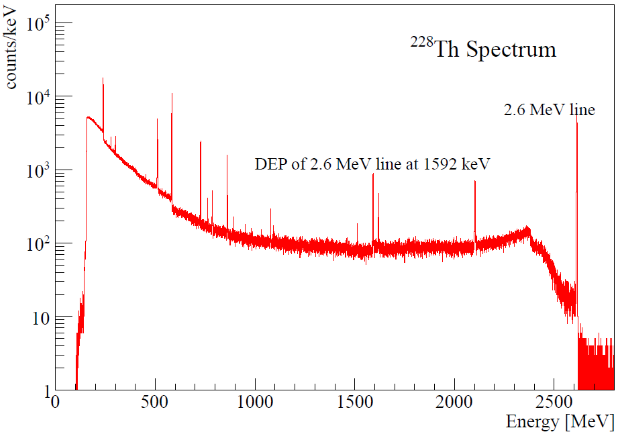

Figure 4.8: ^{228}Th spectrum taken with the bonded test diode

4.3.4 Tests with prototype detectors

After successful pre-testing the evaporation and bonding method on samples and the test detector, the first metallization of BEGe type detectors was performed on-site and in close cooperation with the manufacturer, Canberra Semiconductor NV. First tests showed the need for acetone cleaning of the p^+electrode since otherwise cracking of the film was seen

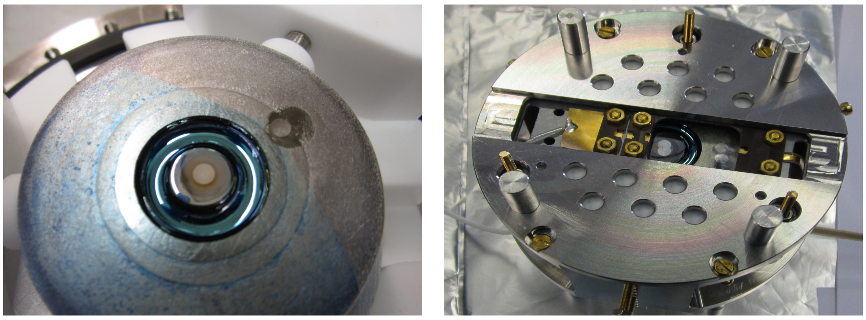

(a) Detector with evaporated bond pads. **(b)** Detector mounted in Phase II prototype holder including massive stainless steel mounting jig

Figure 4.9: Prototype (made from germanium depleted in isotope ^{76}Ge) BEGe detectors used for extensive testing of the evaporation procedure, mounting, bonding and spectroscopic performance.

in liquid nitrogen. This was due to organic residues left beneath the aluminium metallization from prior processing steps. The resulting procedure is reported in Section 4.2.3. For the first metallizations also here the passivation was left on the detector for handling in normal atmosphere during mounting. The detectors used were prototype diodes made from germanium depleted in ^{76}Ge [74], informally called depleted BEGe. In total five detectors of such type were equipped with bond pads. Figure 4.9 shows a metallized prototype detector (depl. BEGe) directly after evaporation and one mounted at the bottom position of a Phase II prototype holder. As a result of this successful metallizations the GERDA collaboration was provided with five working detectors, which were then used in extensive so-called “Integration tests”. These tests were indispensable to gather information about the handling and mounting of the detectors in the new holder assembly and the stability of such a mounted diode during operation. Furthermore different front-end electronics systems were tested for their performance with these detectors [89, 90]. As described in Section 3.4, selecting the proper signal and HV cables was also done in these “Integration tests”

4.4 Processing enriched germanium diodes at Canberra Semiconductors NV

After the successful metallization of the prototype detectors the process was integrated on an industrial scale at the manufacturer such that all 40 germanium diodes (BEGe and coaxial) made from enriched germanium could be modified. Constraints on the procedure were minimized exposure to cosmic rays (CR) above ground, the related logistics and the need for smooth processing without extensive reworking of the diodes. Table 4.3 gives an overview of the complete enriched diode processing. As described in Section 4.2.3 the final acceptance test is a good leakage current curve. This is defined to be less than 100 pA at 1000 V above depletion voltage of the respective diode. There can be two main reasons for a too high leakage current: Particles in the groove or a not well etched groove or a damaged p^+electrode (for more details see Section 2.2.1). These result in distinct LC curves (see Figure 4.10). The remedy for the latter fault is a new doping with boron, causing unwanted extensive rework of the diode. Any groove related LC can be reliably cured by another wet etch. In the complete processing of the 30 enriched germanium BEGe no diode needed a new implantation signifying the safety of the processing methods applied. In Appendix B a full overview of the detector processing and its logistics can be found.

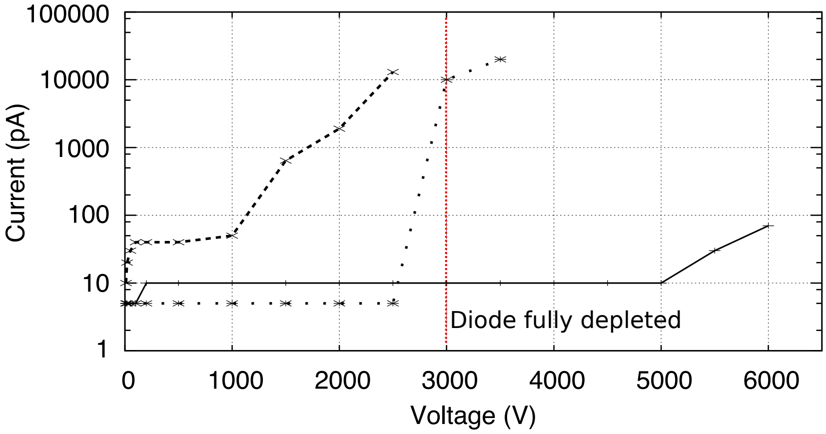

Figure 4.10: IV curves taken at the manufacturer exemplifying different diode behaviours. The dashed curve indicates a not well etched groove. The dotted one hints at a damaged p^+electrode. The solid curve is for a passivated operational detector.

Mean exposure to cosmic rays	Max. exposure	Mean # of re-etches	Max. # of re-etches
14 h	22 h	1.3	3

Table 4.3: Overview of metallization processing of 30 enriched germanium detectors at Canberra Semiconductors, NV.

Chapter 5

Ultra radio-pure components for Front-End electronics

The use of electronic components with ultra high radio-purity is indispensable for low background experiments. In the GERDA experiment custom-made charge-sensitive preamplifiers (CSA) with a cold front-end stage are used [39]. In Phase I the complete front-end (FE) electronics was placed approx. 50 cm far from the diodes, achieving an energy resolution of 3.2-4.8 keV FWHM at $Q_{\beta\beta}$ [67]. For further improvement of the energy resolution by reducing stray input capacitances, pick-up noise and cross-talk, a much closer position of the FE electronics is desired [90].

5.1 Very front-end electronic components

A schematic of the FE electronics can be seen in Figure 5.1. The BEGe type detectors used dominantly in Phase II feature a small ($\mathcal{O}$(pF)) input capacitance which leads to the known excellent energy resolution (see Section 2.5). Comparably small stray capacitances (i.e., from long cables) play in this case a non-negligible role for the resulting noise.

Although high purity materials and components are used (e.g., [84]) placing the entire front-end electronics board just 1-2 centimeters away from the diodes would result in a prohibitive high background contribution. To reduce stray input capacitances, pick-up noise and cross-talk, it is sufficient to bring the resistive feedback circuit part of the FE (in this context called very front-end, VFE) close to the diode. The VFE of the GERDA electronics consists of a high value resistor (several 100 MΩ - few GΩ), a sub-pF capacitor and the preamplifier input Junction-Field-Effect Transistor (JFET). All these components

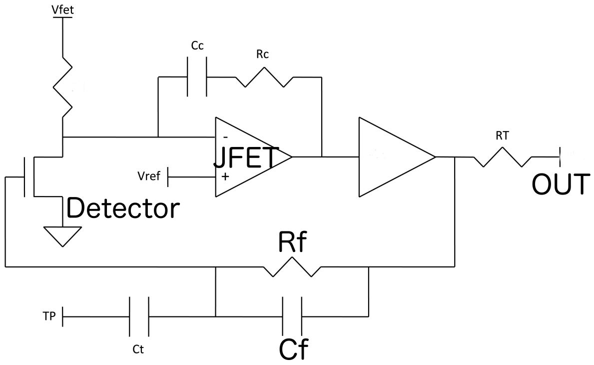

Figure 5.1: Schematic of the FE electronics used in GERDA Phase II. The JFET, R_f and C_f (together called Very Front-End) can be separated from the remaining FE circuit. The VFE should be as close as possible to the detector. From [91].

as well as the printed-circuit board (PCB) for component mounting must fulfil strictest radio-purity constraints. One populated VFE board should have a total activity of $\leq 1\,\mu$Bq in the most relevant isotopes ^{228}Th and ^{226}Ra. The sub-pF capacitor can be realized with the parasitic capacitance between PCB traces and as a separate component it is therefore not further considered. The JFET (Semefab SF291) can be procured in-die (i.e., without any additional chip packaging) and has a specific activity of $< 0.04\,\mu$Bq ^{228}Th and $1.3\pm0.4\,\mu$Bq ^{226}Ra per piece as reported in [92]. The contacting of the JFET is realized via wire-bonding which introduces negligible radioactivity into the system (see Section 6.1.4 and Appendix A). A major challenge is the commercial availability of high value, ohmic, radio-pure resistors.

5.2 Ultra radio-pure high value resistors

An alternative approach to commercially available resistors is the design and fabrication of such devices in a research environment. The deliberate choice of radio-pure materials and a clean production environment can potentially result in ultra radio-pure resistors which meet the requirements of GERDA. The production mechanism of choice is also thin film deposition as in the case of bond pad fabrication (see Chapter 4).

Requirements for a VFE feedback resistor in the GERDA experiment are the following:

- specific activity of $\leq 1\,\mu$Bq/per piece in ^{228}Th & ^{226}Ra
- high resistance ≥ 500 MΩ in liquid argon ($T \approx 89$ K)
- ohmic behaviour for low voltages (< 2 V)

- time stability of resistance

To achieve the low activity intrinsically, clean raw materials must be used. Furthermore, a small footprint is desired to allow for an easy integration on the limited space available on the VFE PCB. The high resistance is advantageous for reaching a low equivalent noise charge (ENC) of the detector-preamplifier system since the thermal noise of a feedback resistor is anti-proportional to its resistance (see, e.g., [93]). A resistance above several GΩ would make the signal decay time ($\tau = C \cdot R_f$) too long during high rate calibration measurements and would lead to significant pile up. Any non-ohmic behaviour at the relevant low voltages could introduce non-linearities in the output signal.

There are numerous materials which are in principle suited for fabrication of such resistors. Many materials (e.g., TiN) have rather low resistivities and have to be fabricated with very thin ($\sim$10 nm) layers. Others (e.g., tungsten) exhibit rapid oxidation and resistance change, and thus require an additional passivation layer. A different ansatz used by the Semiconductor Lab of the Lawrence Berkeley National Laboratory (LBNL) in [94] is the use of amorphous germanium (amGe) as resistor material.

5.2.1 Amorphous semiconductors

Amorphous semiconductors have been studied since the 1960s as the prototypical amorphous material, i.e., featuring random lattice spacings. They have been noted for their high resistivity and large temperature coefficient [95]. The amorphous phase (especially of germanium) is well defined in the sense that most of the optical and electrical properties are measured to be consistent between different preparations and sample histories.

In general all elemental amorphous semiconductors show the following electrical properties: *p*-type conduction due to vacancies acting as acceptor states, much higher resistivity than their crystalline phase and low mobilities ($\sim 10^{-2}\,\mathrm{cm}^2/\mathrm{Vsec}$) [96]. Amorphous germanium in particular has a resistivity ρ of $100\,\Omega\,\mathrm{cm}$ at room temperature and $\sim 10^6\,\Omega\,\mathrm{cm}$ at 77 K, respectively. It exhibits an ohmic behaviour up to electric field strengths of $2 \cdot 10^4\,\mathrm{V/cm}$ [97]. These properties make it ideal for the fabrication of high value, small footprint resistors.

In Figure 5.2 measurements of the temperature-resistance dependence of different sputtered amorphous germanium films are depicted. It is easily seen that the resistance is in the right order of magnitude for the use as a feedback resistor in the GERDA experiment.

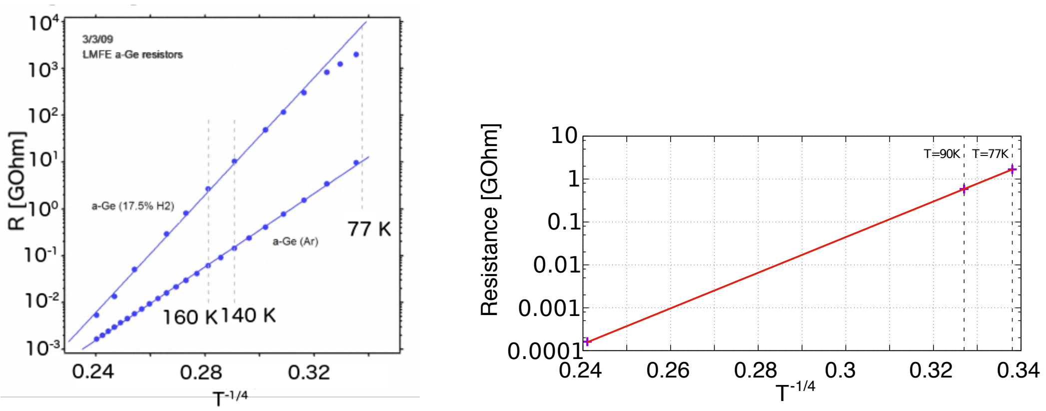

(a) Measurement taken from [94]. ©2011 IEEE

(b) Measurement of resistor made at TUM.

Figure 5.2: Resistance - temperature dependence of amorphous germanium films

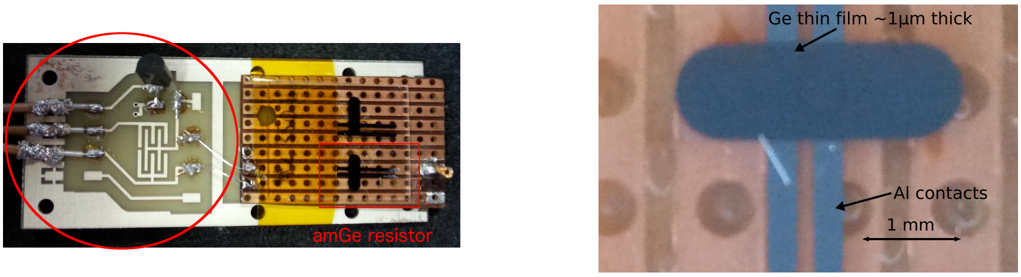

(a) Complete resistor device (including test board, red circle) with aluminium electrodes and underlying copper PCB for electrical connection.

(b) Zoom of the amorphous film and the Al electrodes used for contacting.

Figure 5.3: Amorphous germanium resistor device on a quartz substrate.

5.2.2 Fabrication and testing of amorphous germanium resistors

The fabrication of high resistance sputtered amorphous Ge films was evaluated in view of the excellent results reported in [94]. In contrast to the mentioned publication, a Kaufmann-Robinson Ar-sputtering source [98] was used to produce the thin film. In Table 5.1 the relevant fabrication parameters are presented. Figure 5.3 shows a completed device including aluminium electrodes sputtered on a quartz substrate.

With the given dimensions, resistances of 0.5-10 GΩ in LN_2 are achieved which is in the correct range for a feedback resistor. Due to the temperature dependence (see Figure 5.2b) a slightly smaller resistance is measured at 90 K (liquid argon temperature). The measurement of such high resistances is carried out by taking a current-voltage measure-

Background pressure	Film thickness	Dimensions (length × width)	Resistivity at 77 K
$5\cdot10^{-5}-5\cdot10^{-6}$ mbar	300-1000 nm	0.5 mm × 1-2 mm	$3-5\cdot10^{5}\,\Omega\,\mathrm{cm}$

Table 5.1: Typical fabrication parameters for amorphous germanium resistors. More details on the fabrication and resistance measurements in [99].

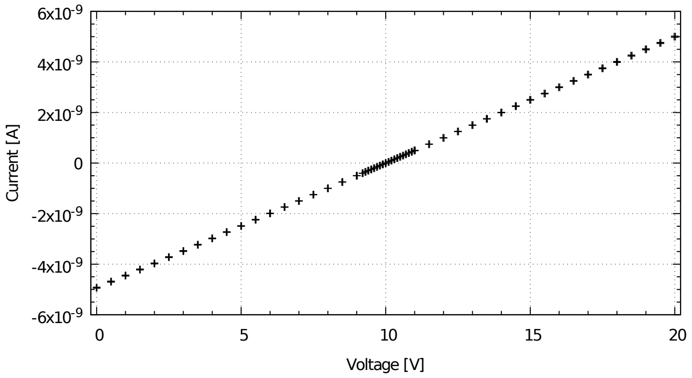

Figure 5.4: Current-voltage measurement of a resistor device to verify the linearity (ohmic behaviour) and to determine the resistance of the device.

ment (IV curve) where the slope of the curve corresponds to the resistance. A simple two-probe measurement is sufficient since the lead resistances are much smaller than the resistances under investigation and thus do not contribute significantly. Figure 5.4 shows a representative IV curve. The linearity (ohmic behaviour) of the device can be verified simultaneously with this measurement.

5.2.3 Increase of device resistance over time

Initial measurements showed very promising results in terms of correct resistance and linearity. However, after subsequent measurements were carried out a steep increase in device resistance was observed after storage in room temperature atmosphere. This behaviour is present in all fabricated resistors. Long term measurements were carried out to study this behaviour. An exemplary measurement is shown in Figure 5.5. An initial fast resistance increase is observed, followed by slower approximately linear increase of resistance.

Simultaneously, amorphous germanium resistors prepared by the authors of [94] were tested for their time stability and also for these devices a continuous slow increase in resistance was found. In Figure 5.6 one such long term measurement is shown. Since the LBNL resistors were not immediately measured after their fabrication, in fact several months

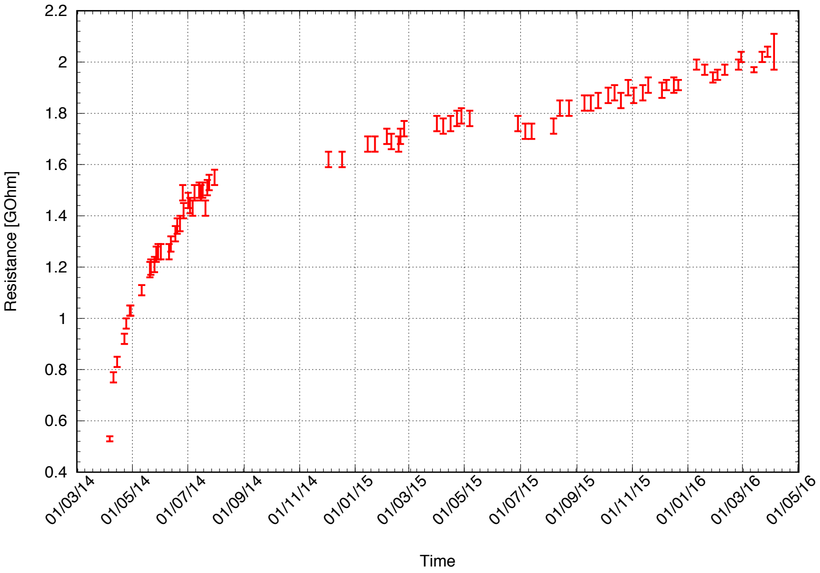

Figure 5.5: Time dependence of resistance with room temperature storage (TUM resistor). An initial fast and later a slow, approx. linear resistance increase can be identified. Storage conditions were not changed.

passed, it is possible that the initial fast resistance increase was not observed. The relative changes of resistance in the approximately linear regions of both measurements agree quite well and also with other measured resistors.

Several treatments were tested to find possible remedies for this behaviour such as different warm-up liquids (e.g., ethanol or methanol), storage in liquid nitrogen or in other cold environments as well as surface passivation. For a detailed description see [99]. Here, only treatments actually affecting the time stability are discussed. It was found that continuous storage in LN_2 stops the resistance increase for the duration of the cryogenic storage (see Figure 5.7). Two plausible mechanism were identified: a) oxidation of the film surface or b) restructuring of the atomic structure as amorphous materials are in a meta-stable state. Both mechanisms are possible since no oxygen is present in LN_2 and restructuring would be energetically much suppressed by the low temperature.

Following these findings, two identical resistors were prepared at the same time and process but subjected to different storage conditions. One device was stored in a freezer ($T \approx 255$ K) and the other was stored in a warm ($T \approx 325$ K) oven. The resulting resistance measurements are shown in Figure 5.8. The cold storage stopped the increase whereas the warm storage resulted in a fast resistance increase. For the warm storage there is a hint

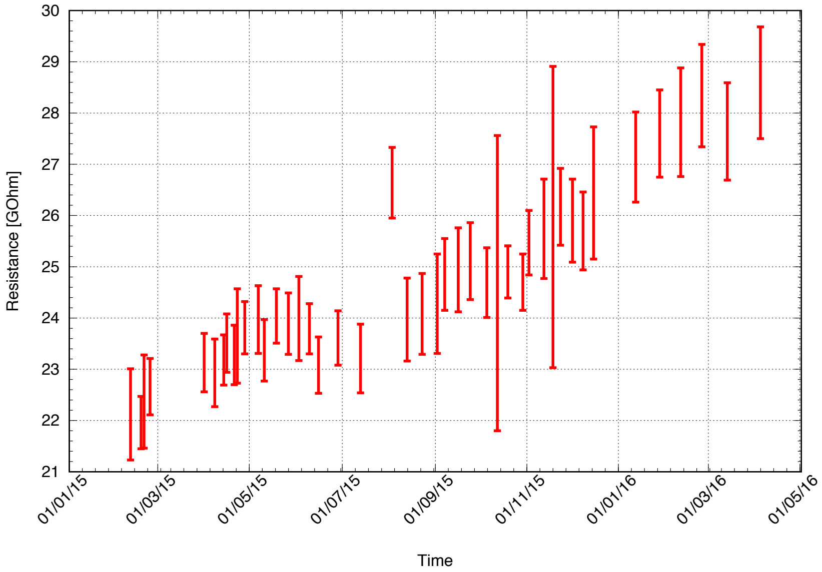

Figure 5.6: Time stability of resistance of a LBNL resistor stored at room temperature. A slow approx. linear increase of the resistance is observed.

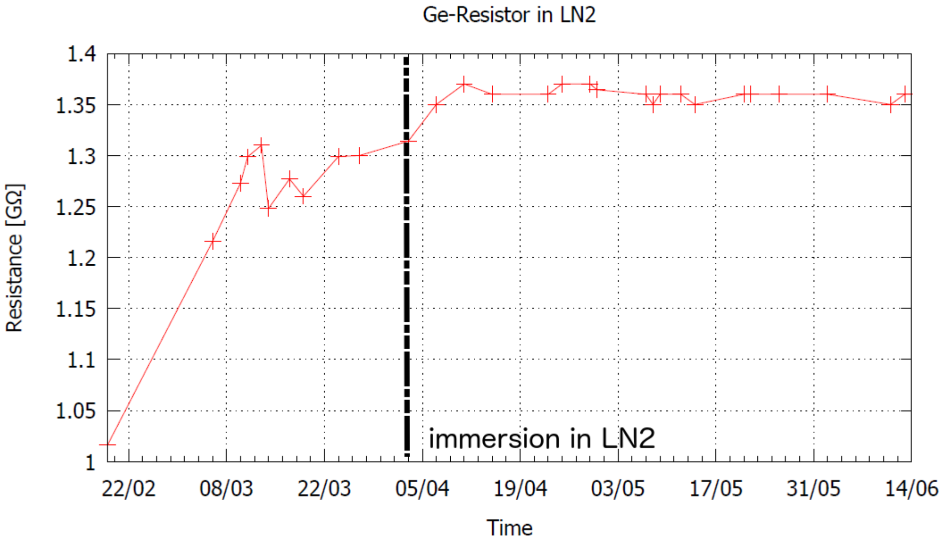

Figure 5.7: Time dependence of resistance of a TUM resistor with a LN2 storage applied (slashed vertical line).

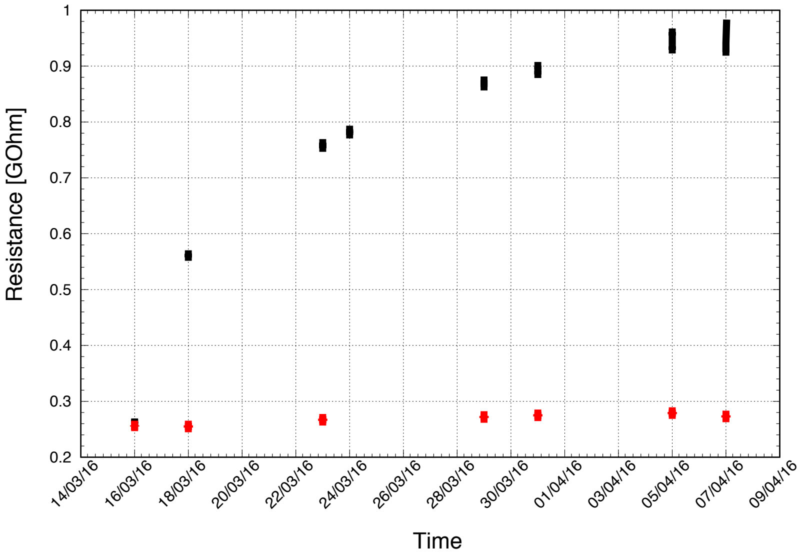

Figure 5.8: Comparison of time stability of two resistors. One was stored in a freezer between measurements (red). This one shows no change in resistance. Whereas the one stored in an oven changes fast in resistance (black).

that the transition between the initial fast increase and the slow one is happening on shorter time scales than observed before. From several months (see Figure 5.5) down to just one month. Further measurements are needed to verify this.

The fact that the cold storage stops the resistance increase could still be attributed to two mechanisms: Either slowing down of chemical reactions (e.g., oxidation) causing the resistance change or inhibiting the restructuring of the germanium atoms by not providing enough energy for the restructuring. A storage in vacuum did not result in a stable device. Therefore, the restructuring mechanism is strongly favoured to cause the increase in resistance over other explanations. Simple cold storage can thus stop the unwanted resistance increase.

5.2.4 Summary and outlook

Advantages and disadvantages of amorphous germanium as a feedback resistor material are:

- germanium is intrinsically radio-pure
- high resistivity results in little required material, small device size and simple geom-

etry and fabrication process

- much lower resistivity at RT leads to difficulties in pre-testing the VFE
- impact of environmental factors and fabrication process (e.g., oxygen, temperature, film structure) on resistance stability are complex and not fully understood but are under control

Amorphous thin film germanium resistors have been fabricated reliably with the correct resistance value. The instabilities observed are under control and can be prevented by a cold storage. The next step would be a resistor fabrication on an ultra-pure fused-silica (brandname Suprasil) substrate which is known to be very radio-pure [75] and subsequent screening, preferably by ICP-MS. In this way additional contaminations during fabrication can be estimated. An integration into existing VFE devices or newly designed ones is easily possible.

Chapter 6

Estimation of background due to the contacting technique

Monte-Carlo simulations were used to estimate the background contributions of possible contaminations due the contacting technique (i.e., metallization and bond wires). For this purpose the simulation framework MaGe [100] was used. Simulated were background contributions due to γs (^{228}Th & ^{214}Bi) and αs (^{210}Po). In Section 6.1 the simulation of the γ background is presented. In Section 6.2 the details of the α simulation are discussed.

6.1 Simulation of γ background

To estimate the background contribution of the contacting technique, two isotopes (^{208}Tl & ^{214}Bi) were simulated. In the next section (6.1.1) the simulated array geometry and the source positions are presented. For all simulated spectra an active volume anti-coincidence (AC) cut at 80 keV is applied as this cut is always applied on the background data in the region interest (see Sections 7.2 and 8.2). This means that only events where a single active volume has a recorded energy deposition, with a threshold of 80 keV, are accepted making a full utilization of the closed packed detector array.

6.1.1 Simulation geometry and source positions

As geometry an idealized and simplified array was simulated. The active volumes (detectors) are simulated as cylinders with 70 mm diameter and 30 mm length with an additional deadlayer of 1 mm on the top and bottom of each of the volumes. 56 active volumes are arranged in seven strings with eight detectors per string. Two detectors form a pair with 5 mm

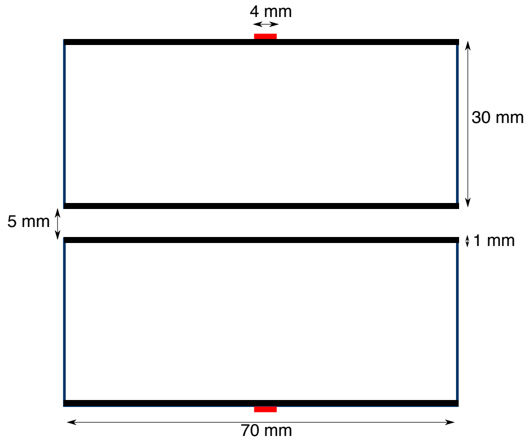

Figure 6.1: Geometry of a simulated BEGe pair with two source positions marked in red and the deadlayer in black.

spacing and four pairs with a spacing of 35 mm form a string. Six strings are symmetrically arranged around one central string. The complete array is immersed in liquid argon. The total mass of the germanium detector array is 36 kg. The contaminants (isotope decays) are simulated in 4 mm diameter circles, placed, radially centred, on top of the deadlayer such that in a pair the circles are not facing each other. This is an approximation since in reality half of the possible contaminants would be located on the thin p^+- electrode. βs from the ^{214}Bi decays could deposit additional energy in the active volume. By requiring the AC cut the influence of this approximation is small. Figure 6.1 shows a drawing of a simulated detector pair and the source positions. Due to the symmetry of this array it is sufficient to simulate only eight different source positions. The upper and lower half of the ideal array are identical, consequently source positions in only one half have been simulated. Each external string and its environment are also identical to the other external strings. Simulation of four source positions (Pos. 11 - 14) in one half of the central string and four positions (Pos. 21 - 24) in one half of one external string are thus sufficient to gain complete information about the background contribution due to the contaminations.

6.1.2 ^{208}Tl background contribution

^{208}Tl is a daughter isotope of ^{228}Th with two main lines, where in 85 % of the decays the high energy γ with 2615 keV is accompanied by one with 583 keV energy. This leads to a strong suppression by the anti-coincidence (AC) cut (see Table 6.1). In Figure 6.2 a representative spectrum, simulated with 1 million decays, before and after AC cut is

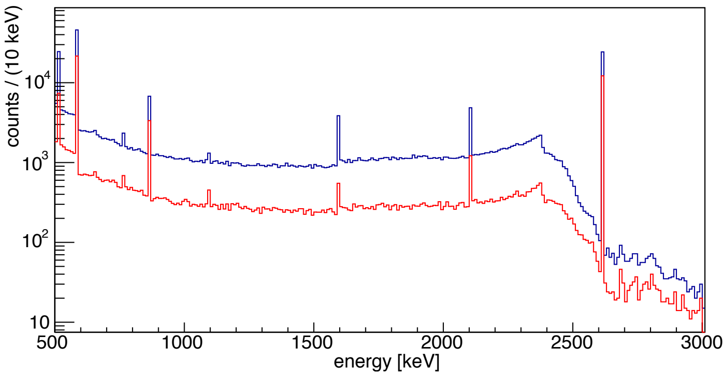

Figure 6.2: Simulated ^{208}Tl spectrum (at Pos14) before (blue) and after (red) AC cut applied.

position	events in ROI	events in ROI w/ AC	AC survival prob.	prob. in ROI
Pos21	4840	2783	58 %	2.8E-03
Pos22	9752	4514	46 %	4.5E-03
Pos23	9758	4637	48 %	4.6E-03
Pos24	16242	5559	34 %	5.6E-03
Pos11	8827	4650	53 %	4.7E-03
Pos12	16005	6084	38 %	6.1E-03
Pos13	16634	6257	38 %	6.3E-03
Pos14	23207	5840	25 %	5.8E-03
Weighted average			45 %	4.6E-3

Table 6.1: Simulation results for ^{208}Tl in the ROI ($Q_{\beta\beta}$ ±100 keV). The relative statistical uncertainties are on the order of 1 - 2 %.

shown. Events above 2615 keV are due to both γs depositing energy in one detector. This simulation was performed for eight different source positions (as described above), the survival probabilities after AC cut and the resulting interaction probabilities in the region of interest (ROI, $Q_{\beta\beta}$ ±100 keV) are reported in Table 6.1. The weighted average is calculated with number of occurrences of the different source positions. Pos. 21 - 24 occur 12 times whereas Pos. 11 - 14 occur two times. The average probability per decay for the 583 keV line to be detected is 1.1 % and for the 2615 keV line it is 0.8 %.

6.1.3 ^{214}Bi background contribution

^{214}Bi is a daughter isotope of ^{226}Ra in the ^{238}U chain. It has several high energetic γ-lines which can contribute to the background at $Q_{\beta\beta}$ via Compton scattering. Their energies and branching ratios are: 2119 keV (1.16 %), 2205 keV (4.9 %) and 2448 keV (1.5 %) as well

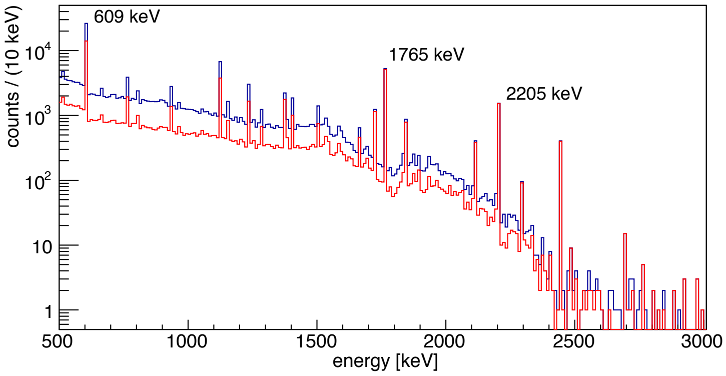

Figure 6.3: Simulated ^{214}Bi spectrum (at Pos14) before (blue) and after (red) AC cut applied.

position	events in ROI	events in ROI w/ AC	AC survival prob.	prob. in ROI
Pos21	487	358	74 %	3.6E-04
Pos22	1026	687	67 %	6.9E-04
Pos23	1076	687	64 %	6.9E-04
Pos24	1876	1112	59 %	1.1E-03
Pos11	940	626	67 %	6.3E-04
Pos12	1736	1080	62 %	1.1E-03
Pos13	1741	1036	60 %	1.0E-03
Pos14	2609	1395	54 %	1.4E-03
Weighted average			65 %	7.6E-4

Table 6.2: Simulation results for ^{214}Bi in the ROI ($Q_{\beta\beta}$ ±100 keV). The relative statistical uncertainties are on the order of 2 - 5 %.

as several higher energetic ones with very low intensity. For background studies the lower energy lines of 609 keV (45 %), 1120 keV (15 %) and 1765 keV (15 %) are of interest. In Figure 6.3 a representative simulated spectrum, again with 1 million decays, before and after AC cut, is shown.

This simulation was performed for eight different source positions (as described above), the survival probabilities after AC cut and the resulting interaction probabilities in the region of interest ($Q_{\beta\beta}$ ±100 keV) are reported in Table 6.2. The weighted average is calculated with number of occurrences of the different source positions. Pos. 21 - 24 occur 12 times whereas Pos. 11 - 14 occur two times. The average probability per decay for the 609 keV line to be detected is 0.7 %, for the 1765 keV line it is 0.2 % and for 2205 keV line it is 0.07 %.

component	^{228}Th activity [Bq/kg]	^{226}Ra activity [Bq/kg]	BI [cts/(keV·kg·yr)]
Balzers Al film (14 detectors)	0.3	0.5	2×10^{-6}
MaTecK Al film (26 detectors)	< 3E-3	< 1.6E-2	$< 7\times10^{-8}$
Bond wires (160)	0.07	0.05	1×10^{-6}
Total BI for contacting			$\approx 3\times10^{-6}$

Table 6.3: Background contribution of contacting. The BI is well below the requirement of 10^{-3} cts/(keV·kg·yr)for Phase II.

6.1.4 Expected background from the metallization and wire bonding

With the simulated interaction probabilities and a given specific activity of the used materials it is possible to calculate the background contribution expected from the metallization and the wire bonding. As an example a specific activity of 0.5 Bq/kg of ^{214}Bi (15770 decays/g·yr), $40\times40\,\mu$g of aluminium in the array and 42 kg of detector mass are assumed. A background index of

$$2\cdot10^{-6}\frac{\text{cts}}{\text{keV}\cdot\text{kg}\cdot\text{yr}} \tag{6.1}$$

is the result which is several orders of magnitude lower than the aimed for background index for Phase II of 10^{-3} cts/(keV·kg·yr). In Table 6.3 the background index induced by the total contacting solution (metallization and wire bonding) is presented. Two different aluminium qualities with differing radio-purity were used (see Table 4.1). Even though the Balzers material showed a much higher contamination its background contribution is much below any critical magnitude.

The background due to 1 mBq/kg of ^{26}Al and ^{22}Na each (see Section 4.1.2) can be roughly estimated by taking the simulation results of [83] with 13 mg of aluminium per detector and scaling them to the 90 μg used for the Phase II detectors. Even the most dangerous contamination (^{26}Al) would give a contribution of $\mathcal{O}(10^{-7})$ cts/(keV·kg·yr) which is negligible. The difference is that only a small part of the detector is metallized in contrast to assumptions in [83].

In this section only background from γs were investigated but α decays on the detector surface are potentially as dangerous. The possible background from these decays is discussed in the next section.

6.2 Simulation of α background

The detectors used in the GERDA experiment are partially shielded from αs by the thick (coaxial > 1 mm, BEGe $\simeq$ 1 mm) n^+- electrode (which is not active) covering most of the surface of the detector. The only region where α can enter the active detector volume is the p^+- electrode (< 600 nm thick) and the groove. Any modification or process (like the metallization and bonding) applied to this part can potentially contaminate it. Most dangerous for the background in the region of interest are the αs which lose part of their energy (degraded α) in the not-active region of the p^+- electrode (called deadlayer) and are thus reconstructed at an energy in the region of interest for $0\nu\beta\beta$.

6.2.1 Simulation geometry

In contrast to the simulation of the γs, the α induced background needs to be simulated only in one detector since the αs cannot deposit energy in more than one detector. Since the degradation of the energy depends strongly on the thickness of the deadlayer this is the most critical parameter for a realistic simulation. As described in [62,66] for Phase I these simulations were already performed in more detail for coaxial detectors. A comparison with Phase I data showed that a homogeneously thick deadlayer is not a good assumption. For the BEGe detectors such study was not performed due to the limited statistics in Phase I. As a consequence in this work a range of different deadlayer thicknesses were simulated and a range of background contributions is given as a result. Figure 6.4 presents the geometry used for the simulation. In this simulation αs are emitted isotropically and consequently only half of the simulated decays enter the detector.

6.2.2 Simulations of a ^{210}Po contamination with varying deadlayer thicknesses

From previous studies [62,66] it is known that the main α contamination stems from ^{210}Po which is an isotope of the ^{222}Rn chain with a Q-value of 5.41 MeV and a half life of 138 d.

Figure 6.4: Geometry of a simulated detector with the contamination position marked in red and the deadlayer in grey.

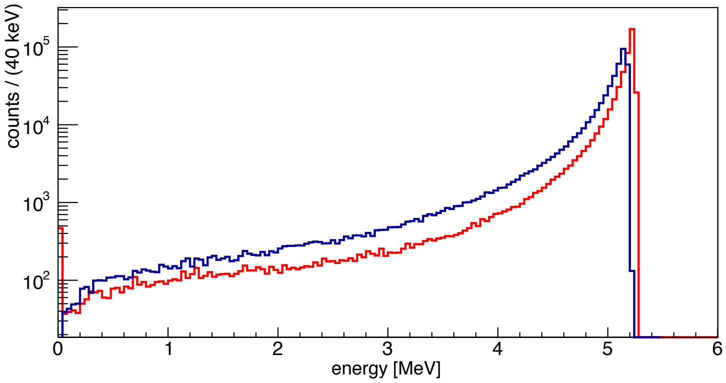

Figure 6.5: Simulated ^{210}Po spectra with 1 million decays on a detector with 300 nm (red curve) and 600 nm (blue curve) deadlayer. The exponentially decreasing low energy tail is well visible. For 300 nm more events are recorded in the peak whereas for 600 nm more degraded αs are visible.

DL thickness	probability in ROI	probability in peak (4.8 - 5.3 MeV)
300 nm	1.4E-3	0.44
400 nm	1.7E-3	0.42
500 nm	2.1E-3	0.39
600 nm	2.5E-3	0.37

Table 6.4: Probabilities for α events in different energy regions with 1 million events simulated each. The statistical uncertainties are thus lower than 1E-4.

As will be shown in Sections 7.2 and 8.2.1, this contamination is indeed dominant. Simulations were performed with the ^{210}Po decaying directly on top a deadlayer with thicknesses of 300, 400, 500 and 600 nm, respectively. In Figure 6.5 two resulting spectra with 300 nm and 600 nm deadlayer are shown.

The main features of the spectra are the peak structure at ca. 5.3 MeV, close to the Q-value of the decay, and the exponentially decreasing tail towards lower energies. The events with highest energies stem from α which enter the active volume by the shortest path length (in this case 500 nm) through the deadlayer. Events with lower reconstructed energy cross into the active volume at an angle and thus traverse more than the minimal 500 nm losing more energy in the process. From the different simulations it is possible to extract the probabilities of an event in the region of interest (1.8 - 2.2 MeV) per ^{210}Po decay. Furthermore the probability of an energy deposition in the peak (4.8 - 5.3 MeV) can be determined.

In Table 6.4 these probabilities for different deadlayer thicknesses are presented. In the range of the deadlayers simulated, a thicker deadlayer leads to less event in the peak and more in the region of interest, making such a configuration potentially more dangerous for the GERDA experiment. A calculation of the resulting background index in combination with data is discussed in Section 8.2.1.

Chapter 7

Commissioning the GERDA Phase II array

In this chapter an overview of the conducted commissioning runs with the new Phase II array including LAr veto, new detector holders, upgraded front-end electronics and new detectors (BEGe) is given. In Section 7.1 the upgrade works are described with focus on the detector related items, furthermore the array configurations used in the different runs and their performances are presented. Subsequently in Section 7.2 a preliminary background analysis is discussed with special attention on possible contaminations related to the metallization & bonding.

7.1 Hardware commissioning

As described in Section 2.4 the lock infrastructure was enlarged to house the LAr veto system and the larger detector array prior to the commissioning runs (for a description see Section 2.4). A major task was the so-called detector integration, "merging" the individual diodes into an array of functioning radiation detectors. As a result of the commissioning changes in the hardware configuration (e.g. in the detector holders) were made. These are described in Section 7.1.2.

7.1.1 Detector integration

Integration into a complete detector array consists of several sequential tasks which are:

Detector assembly

- equipping a silicon plate with a signal and a HV flex cable
- mounting two BEGe diodes in a pair holder or single coax diodes in single holders
- wire bonding HV electrode and signal electrode directly to the respective flex cable (two bonded connections each)
- cleaning diode groove from dust particles with methanol
- transferring mounted diodes to GERDA glove box around lock infrastructure

String assembly

- assembling diodes in strings (with eight BEGe per string or three coaxial per string)
- mounting each string on suspension system
- connecting signal cables to front-end electronics and HV flex cables to HV coaxial cables
- installing transparent shrouds around each string against ^{42}K ions, progenitors of ^{42}Ar.

Figure 7.1 shows a sequence of selected steps and the final detector array. Except for attaching the signal and HV flex cables on the silicon plates all tasks are done in a nitrogen flushed glove box to avoid contaminations and surface leakage currents due to exposure to humidity and oxygen (see Section 2.2.1).

7.1.2 Detector array performance during commissioning

First commissioning ("Run50")

The commissioning of the Phase II detector array started in summer 2015 when 28 detectors (23 BEGe and 5 coaxial) were mounted in five strings. Three detectors could not be used at all and had to be switched off. One had a broken electronics channel, one was shorted to ground due to a broken bond and one had a broken HV flex cable. Furthermore several (6) detectors could not be put to operational voltage since they showed high leakage current. A last detector induced signals for other channels while at operational voltage. In total only 15 detectors of 28 immersed were used for spectroscopy with a total mass of 12.3 kg and a livetime of 32.1 days (27/07/15 - 07/09/15). After this run the broken

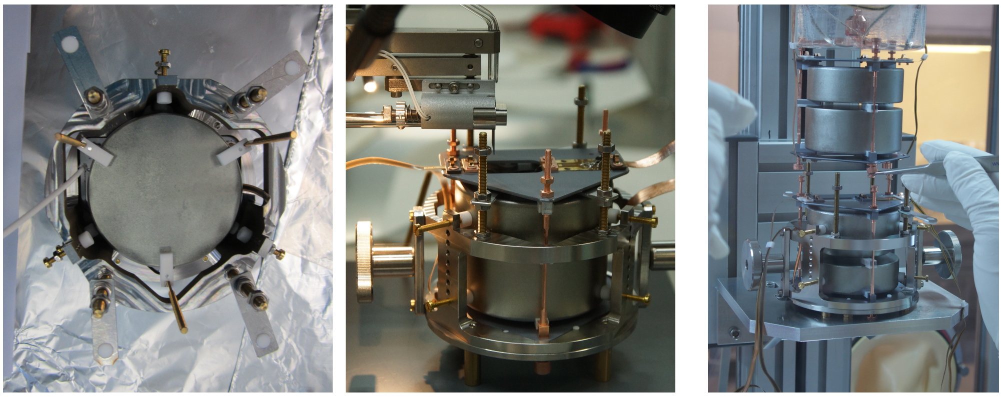

(a) BEGe diode mounted in holder. **(b)** Wire bonding a pair of assembled BEGe diodes. **(c)** Assembly of detector pairs into string.

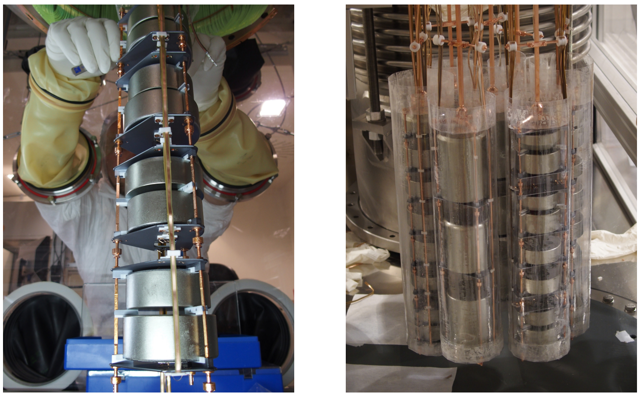

(d) Completed string fixed to suspension system **(e)** Complete detector array with transparent shrouds

Figure 7.1: Selection of detector and array integration steps.

components were repaired and a second run was started. In addition detectors showing excessive leakage current were sent to the producer and repaired. For the following run these detectors were not available. Table 7.1 gives an overview of the used detectors for each commissioning run including the achieved energy resolution during ^{228}Th calibrations.

Second commissioning ("Run51")

Prior to the run a test immersion incident happened (LAr veto blocked detector array) and this resulted in less detectors mounted and used than in the previous run. 12 (eight BEGe and 4 coaxial) were mounted in three strings and immersed and this time no detector was found unconnected. Still two detectors could not be put to the operational voltage and were used for anti-coincidence purposes only. Nevertheless the ratio of 10/12 working detectors

Detector ID	Run 50 FWHM [keV] Gauss	 ZAC	Run 51 FWHM [keV] Gauss	 ZAC	Run 52 FWHM [keV] Gauss
00A	3.41	3.08	-	-	3.42
00B	7.47	4.61	-	-	4.64
00C	-	-	2.97	-	-
00D	2.82	2.77	2.97	2.88	3.07
02A	2.94/AC	2.7/AC	-	-	3.07
02B	3.20	2.95	-	-	3.36
02C	2.83	2.75	-	-	3.05
02D	-	-	-	-	3.31
32A	2.91	2.86	-	-	3.20
32B	2.88	2.83	-	-	2.97
32C	off	off	-	-	2.93
32D	AC	AC	-	-	3.28
35A	7.88/AC	5.39/AC	6.39/AC	3.39/AC	-
35B	3.05	3.01	-	-	3.26
35C	2.71	2.58	2.67	2.58	2.64
61A	off	off	-	-	3.42
61B	2.94	2.97	-	-	2.82
61C	3.22	3.09	-	-	9.67/AC
76C	2.72	2.67	2.77	2.83	3.03
79B	-	-	-	-	3.55
79C	3.26	3.23	3.85	3.33	3.29
89A	AC	AC	-	-	-
89C	off	off	-	-	2.88
89D	3.03	2.97	3.48	3.50	3.00
91A	-	-	-	-	3.43
91B	3.01/AC	2.84/AC	3.06	3.05	-
ANG1	AC	AC	-	-	3.37
ANG2	AC	AC	AC	AC	AC
ANG5	4.04	3.65	4.59	4.25	4.75
RG1	3.98/AC	3.60/AC	6.16	3.86	5.20
RG2	9.44/AC	5.35/AC	4.02	3.91	4.86
GTF45	-	-	-	-	3.73

Table 7.1: All detectors used in the three commissioning runs with their respective energy resolution during ^{228}Th calibration at 2.615 MeV. The statistical uncertainty is ca. 2%. "Gauss" indicates gaussian filtering and "ZAC" an optimised filtering algorithm (Zero-Area Cusp see [93]) filtering low-frequency noise. "AC" shows that detector was used only for the anti-coincidence cut due to instabilities or its operation below operational voltage due to leakage current. "off" means a non-working detector or electronic channel. "-" shows a detector was not used at all in the particular run. In Run 52 no ZAC optimization was performed. Values from [101].

indicated a much better performance than in Run 50. 13 kg of detector mass were used for 25 days (30/09/15 - 29/10/15).

Third commissioning ("Run52")

A total of 28 detectors were immersed in this run and 26 could be used for spectroscopy since two channels showed electronic instabilities. Consequently this was the run with highest (absolute and relative) number of working channels. Not all strings were equipped with transparent shrouds since some of them were found broken after the last run and could not be repaired. Only nine BEGe and one coaxial detector were equipped with the shrouds. The missing shrouds meant a much higher β-background from ^{42}K decays in the remaining channels. For the spectral analysis only the shielded detectors were used.

Changes of hardware as result of commissioning

During the three commissioning runs two bonds were found to be broken (only one being problematic for the detector), one after Run 50 and one after the test immersion prior to Run 51. A too strong pulling on the (directly bonded) flex cables was identified as the possible cause. The routing procedure of the flex cables was modified to not pull on the cables too much. After this modification no more broken bonds were observed. In all commissioning runs together a total of 760 bonds were immersed and only two bond wires broke which is a fraction of 0.3%.

During the commissioning runs it became clear that several detectors could not be put to operational voltage due to excessive leakage currents. These were mostly upward facing diodes where particles could congregate in the groove. In total 13 BEGe diodes had to be sent back to the manufacturer for repair and were in addition equipped with a passivation layer for more robustness (see Section 2.2.1 and Appendix B). The holder design was partially changed such that most of the upward facing diodes would now face downwards. Diodes were now mounted in single holders. After these modifications were implemented following Run 51, the fraction of detectors working at operational voltage increased substantially.

7.2 Analysis of commissioning run data

In this section the background spectra, acquired during the three commissioning runs, are discussed. The spectra are shown for BEGe (Figure 7.2) and coaxial detectors (Figure 7.3).

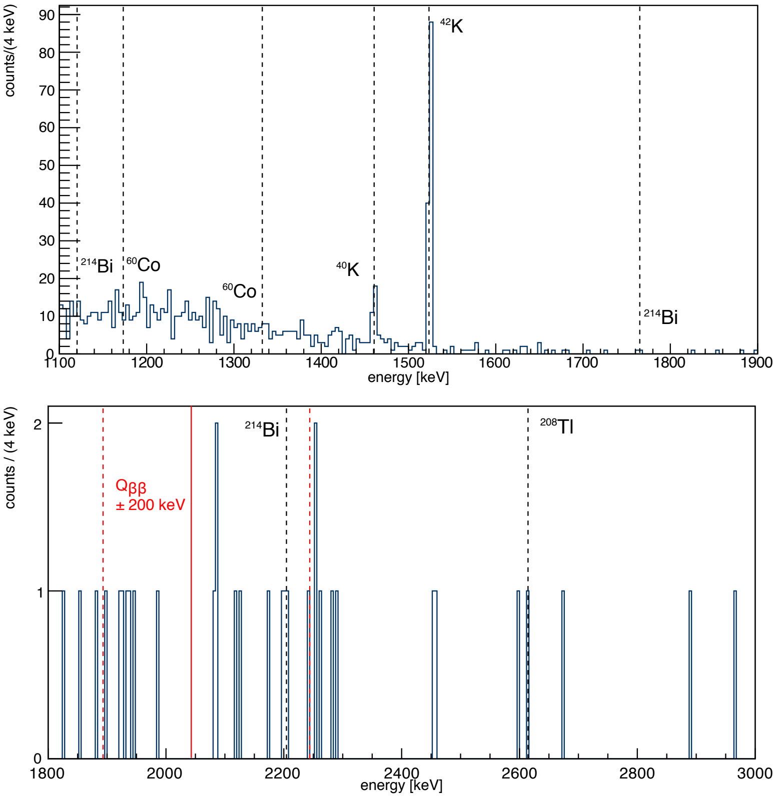

Figure 7.2: BEGe background spectrum with an exposure 0.84 + 0.35 +0.35 =1.54 kg·yr after muon and anti-coincidence cut. Relevant γ lines are indicated as well as $Q_{\beta\beta}$.

The muon veto and the detector anti-coincidence, as well as the usual quality cuts to reject non-physical events (see [102]) are applied beforehand. The window of 1100 - 1900 keV shows several γ lines with the 1525 keV line from ^{42}K decays and the 1461 keV line from decays of ^{40}K being the most prominent. The continuum visible between 1100 and 1500 keV decreases towards higher energies and originates from $2\nu\beta\beta$ decays and from Compton scattering of the ^{40}K and ^{42}K γs. The window of 1800 - 3000 keV shows the region of interest (ca. 200 keV around $Q_{\beta\beta}$) as well as the higher energy part where the ^{208}Tl line would be located at 2615 keV. In general the spectra are similar to the ones of GERDA Phase I and no new significant features are visible. A more quantitative analysis of the γ-lines present is given in Table 7.2. This analysis uses the same models (two Poisson distributions, signal and background resulting in one posterior distribution) and a Bayesian approach as described in [103]. Significant γ count rates are found at 1525 keV (^{42}K),

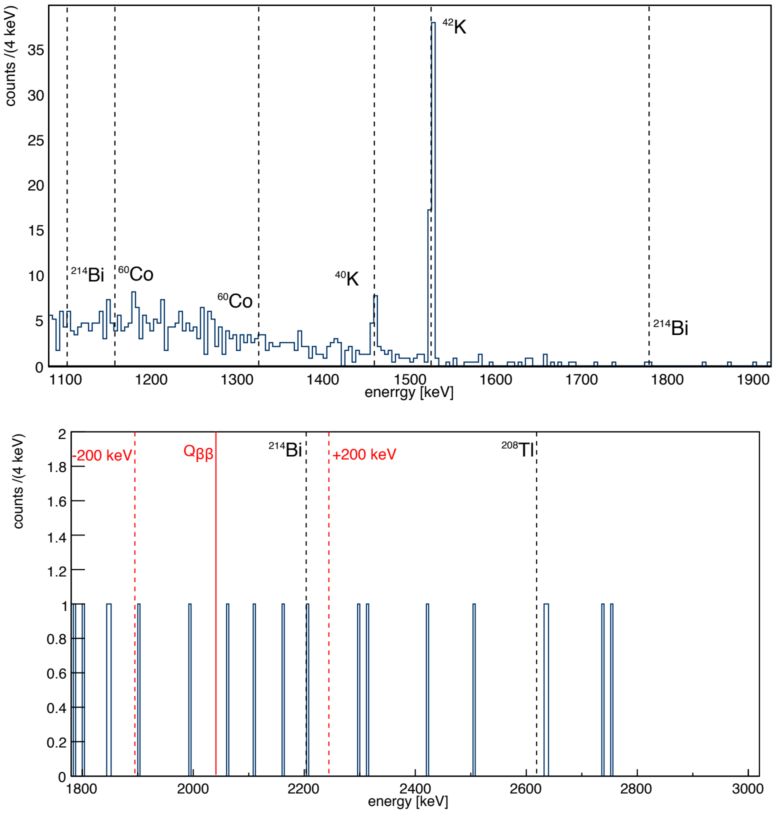

Figure 7.3: Coaxial detector background spectrum with an exposure 0.24 +0.49 +0.05 = 0.78 kg·yr after muon and anti-coincidence cut. Relevant γ lines are indicated as well as $Q_{\beta\beta}$.

1461 keV (^{40}K), 1120 keV (^{214}Bi) and 2205 (^{214}Bi). The uncertainties are high due to the low statistics, with a total exposure of 2.3 kg·yr and prevent a more precise analysis at this moment. A significant higher count rate than in Phase I is observed in the 1525 keV line. A possible explanation is the stronger attraction of ^{42}K ions (progenitors of ^{42}Ar) due to less electrical shielding of the detectors and the HV cables (see Section 8.2). The transparent mini-shrouds form a barrier against these ions but of course does not shield against γs. Regardless of the cause this γ does not constitute a source of background since it only accompanies the β ($E_0 = 3525$ keV) which in contrast has a high enough energy to be relevant as a background source if the decay happens on the surface of a detector (which probability is suppressed by the mini-shroud).

In conclusion, no unexpected high γ-activity related to the contacting technique has been observed with this small exposure data set.

		BEGe (1.54 kg·yr)		Coaxial (0.78 kg·yr)	
isotope	energy [keV]	tot/bkg [cts]	rate [cts/kg·yr]	tot/bkg [cts]	rate [cts/kg·yr]
^{40}K	1460.8	37/13	$15.5^{+4.6}_{-4.8}$	19/1	$22.2^{+6.2}_{-5.8}$
^{42}K	1524.7	131/6	$80.9^{+7.7}_{-7.7}$	72/6	$83.7^{+12.1}_{-11.0}$
^{60}Co	1173.2	48/49	< 10.3	28/28	< 12.5
	1332.5	31/26	< 10.5	10/15	< 7.7
^{214}Bi	609.3	94/88	< 17.1	41/48	< 15.4
	1120.3	49/36	$8.1^{+5.8}_{-5.1}$	27/25	< 17.2
	1764.5	2/0	< 3.1	0/0	< 3.0
	2204.5	3/0	$1.5^{+1.4}_{-1.0}$	1/0	< 4.5
^{208}Tl	583.2	105/100	< 17.5	42/49	< 15.6
	2614.5	1/1	< 2.1	0/0	< 3.0

Table 7.2: Table of γ-lines relevant for GERDA as measured during the commissioning runs of GERDA Phase II. “tot” is counted in a 16 keV window centered on the given decay energy. “bkg” is counted in two 8 keV regions adjacent (lower & higher) to the “tot” window. For the rates the global mode and the 68 % smallest C.I. are given, or in case where this contains 0 the 90 % quantile is reported as a limit.

7.2.1 Alpha induced high energy events

A possible contamination of the detectors during the metallization or bonding process can be checked best by an analysis of α induced events. In contrast to most possible background sources (e.g. the holder parts or flex cables) the Al thin films are located directly on the detector surface. As described in [62] αs can deposit energy in the detector active volume only if they penetrate through the thin p^+- electrode or the groove (the separation region between signal and HV electrode). The nearly one millimeter thick n^+- electrode effectively shields from αs on this surface. Consequently the thin Al film deposited on the p^+- electrode could be a source of α contamination. As presented in Section 2.3.1 and [62] in Phase I the dominant α emitting isotope was ^{210}Po with small contributions from other ^{226}Ra sub-chain isotopes.

In Figure 7.4 the high energy background spectra (summed over all three commissioning runs) of coaxial and BEGe detectors are shown. In the high energy region of the background spectrum (> 3.6 MeV) only α induced events are present since γ events have maximum energy of 2.6 MeV (^{208}Tl) and βs an energy of 3.5 MeV (endpoint of ^{42}K). These spectra show very similar features as the corresponding spectra from Phase I [62].

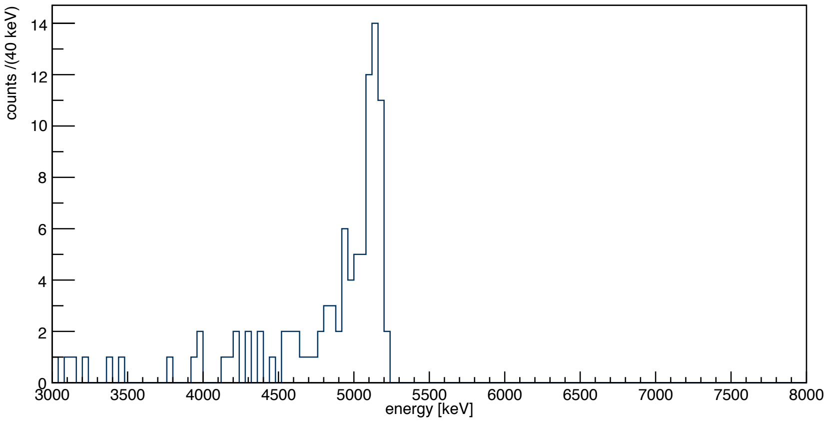

(a) BEGe detectors with 2.0 kg·yr exposure and 1049 detector · days

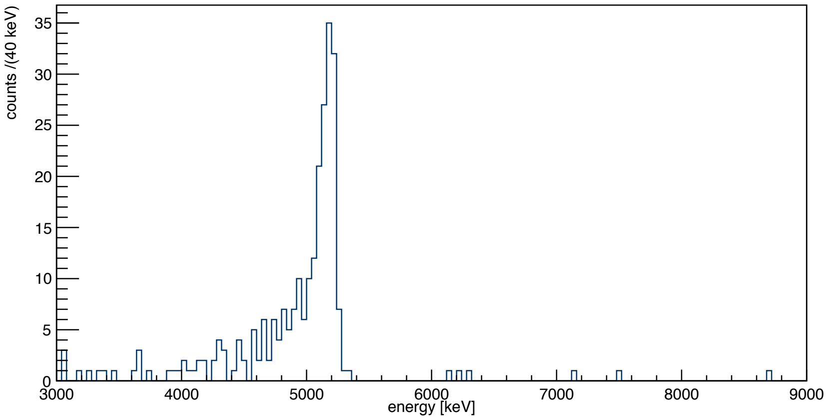

(b) Coaxial detectors with 1.6 kg·yr exposure and 209 detector · days

Figure 7.4: High energy event spectra of coaxial and BEGe detectors summed over all three commissioning runs.

The few events above 5.3 MeV (seen only in the coaxial detectors) originate most likely from the ^{222}Rn chain whereas the events below 5.3 MeV stem predominantly directly from ^{210}Po. It is easily seen that coaxial detectors show more α events than BEGe. The hypothesis is that the number of α events per time scales with the sensitive surface. This surface is ca. 10 x larger for coaxial diodes than for BEGe diodes due to the bore hole. In Table 7.3 the number of αs (events > 4 MeV) for the different runs and detector types is reported. Normalized to the livetime and the number of active detectors (detector · days) the rate comparison shows a factor of ∼12 difference between coaxial and BEGe detectors which supports this hypothesis.

A question of interest is the origin of the α contamination. Two main ways are pos-

	Run 50	Run 51	Run 52
Livetime [d]	32.1	25.6	20.0
# BEGe	14	7	21
# Coaxial	1	3	5
α in BEGe	33	17	37
α in Coaxial	31	66	143
α in BEGe / det. / day	$0.07^{+0.01}_{-0.01}$	$0.09^{+0.03}_{-0.02}$	$0.09^{+0.02}_{-0.01}$
α in Coaxial / det. / day	$0.97^{+0.18}_{-0.17}$	$0.85^{+0.12}_{-0.10}$	$1.43^{+0.13}_{-0.12}$
Mean α rate in BEGe		0.08 ± 0.01	
Mean α rate in Coaxial		1.15 ± 0.07	

Table 7.3: Overview of α counts and rates for the three commissioning runs with number (#) of detectors active and number of α measured in the different detector types. The overall rate is weighted by livetime and number of detectors (detector · days). All uncertainties are poissonian.

sible. If the majority of α emitting isotopes are brought to the surface during production and/or the metallization process the α rate should remain constant over the different runs except for an exponentially decrease of ^{210}Po with $\tau = 138\,\mathrm{d}$. Due to the short uninterrupted measurement time this decrease is not seen. If on the other hand the amount of handling of the diodes during (re-)mounting or (re-)bonding would play a dominant role in the contamination, differences in the rates between the runs might be seen. In Table 7.4 the α rates of detectors used in all three runs are reported. Except for ANG5 (in Run 51) all diodes show a compatible rate among the three considered runs. Since prior Run 51 an incident happened and the detector preparation in terms of handling were untypical thus a higher contamination cannot be excluded. The investigated detectors and runs make the handling contamination hypothesis seem less likely.

Diode	cts	rate/d Run 50	cts	rate/d Run 51	cts	rate/d Run 52
ANG5	31	$0.97^{+0.18}_{-0.17}$	40	$1.56^{+0.28}_{-0.22}$	16	$0.79^{+0.24}_{-0.17}$
RG2	-	-	11	$0.61^{+0.20}_{-0.17}$	6	$0.31^{+0.14}_{-0.11}$
35C(pass)	0	$0^{+0.04}_{-0.0}$	2	$0.08^{+0.07}_{-0.04}$	0	$0^{+0.06}_{-0.0}$
00D(pass)	2	$0.06^{+0.06}_{-0.03}$	1	$0.04^{+0.06}_{-0.03}$	1	$0.05^{+0.08}_{-0.04}$
89D	8	$0.25^{+0.11}_{-0.07}$	5	$0.20^{+0.11}_{-0.07}$	4	$0.20^{+0.12}_{-0.09}$
79C	2	$0.06^{+0.06}_{-0.03}$	4	$0.16^{+0.09}_{-0.07}$	3	$0.15^{+0.11}_{-0.07}$
76C	3	$0.10^{+0.06}_{-0.05}$	2	$0.08^{+0.07}_{-0.04}$	1	$0.05^{+0.08}_{-0.04}$

Table 7.4: α rates in different detectors in the commissioning runs. The rates do not differ significantly between the different runs, except for ANG5 in Run 51.

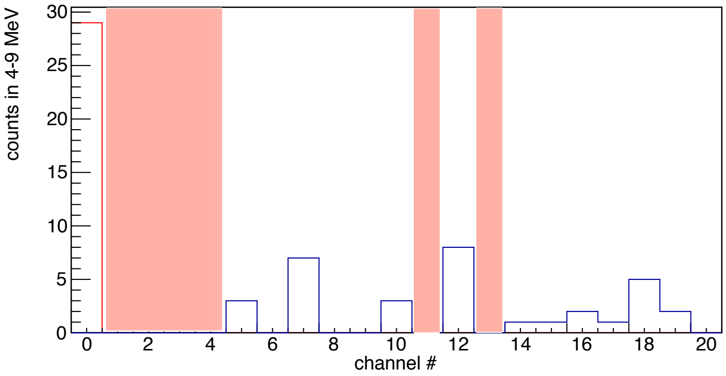

(**a**) Run 50

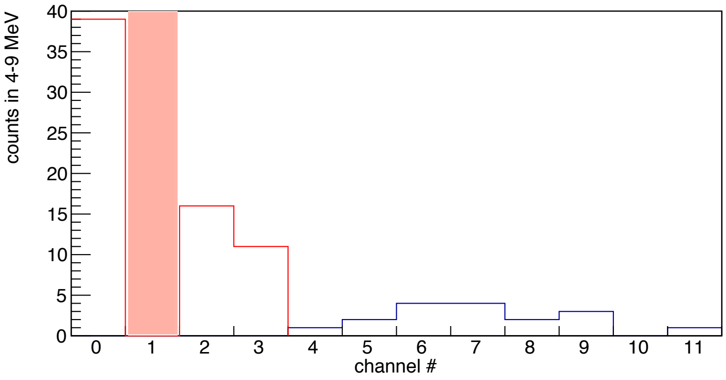

(**b**) Run 51

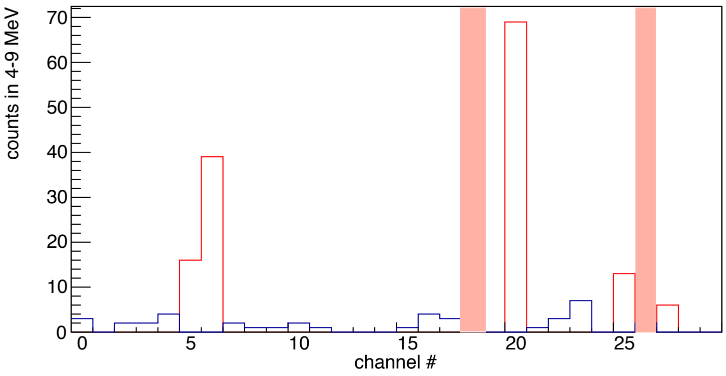

(**c**) Run 52

Figure 7.5: Distribution of high energy events (αs) in different channels during the three commissioning runs. Not working channels are marked with red bars. Coax channels have red histograms, BEGe channels blue. A significantly higher number of αs is visible in coaxial channels in all three runs. The channel - detector mapping can be found in Appendix C

Furthermore the α "contamination" is not very uniformly distributed among the individual detectors. As shown in Figure 7.5 the variation between detectors of the same type is substantial. A possible explanation for this might be different or additional production steps done with the diodes at the manufacturer. As mentioned in Section 7.1.2 a subset of diodes had to be repaired after they developed too high leakage current prior and during the commissioning runs. This subset had to be equipped with a passivation layer on a part of the α sensitive surface (the groove). These detectors underwent a further production step and the question is if this influenced the α background. A comparison of the passivated and the non-passivated detectors (only of BEGe type) was done in Figure 7.6. The his-

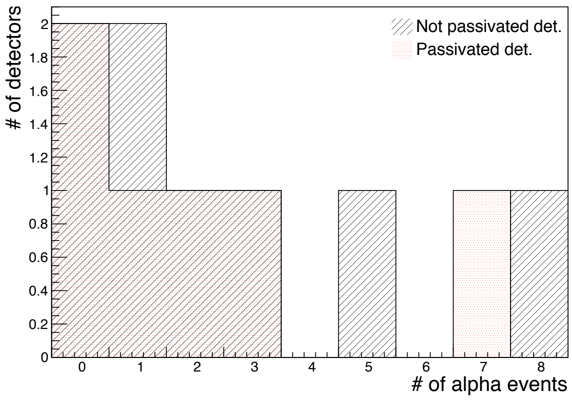

(a) Run 50

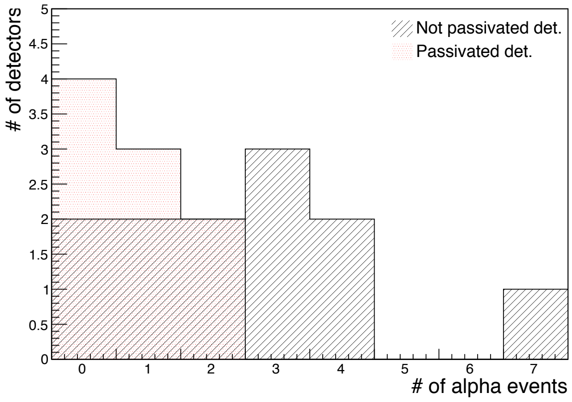

(b) Run 52

Figure 7.6: Comparison of α count distributions between passivated and non-passivated detectors in Run 50 and 52. The number of α events in individual detectors (x-axis) and the occurrence (number of detectors, y-axis) is shown. A small difference in the distributions is observed. Thus there is an indication that passivated detectors do have smaller visible α contamination.

togram shows the occurrence (how many detectors see 0,1,.. α events) versus the number of events in individual detectors. Here only two runs (50 and 52) are shown since in Run 51 the number of BEGe detectors (seven) was too low for a meaningful comparison. A difference between the two distributions is observable especially in Run 52 (with highest number of detectors, 21). There is an indication that passivated detectors have smaller α count rate. A possible explanation would be that the passivation layer is acting as a dead-layer and shields the αs from the active volume. But since the thickness is just ca. 100 nm a complete stopping or even a significant energy loss are not possible for 5.3 MeV α. An explanation is thus still missing for the observed behaviour.

In summary there is no indication that the Al film constitutes a dominant source of α background since the variations between types and individual detectors are very large and the metallization, being the same on every detector, should not introduce such variations.

In earlier investigations (see [103, 104]) the possibility to remove α events in BEGe detectors via pulse-shape discrimination (PSD) was studied and proven. Since αs can deposit energy only very close to the p^+- electrode the trajectory of the charge carrier cloud is distinct from other trajectories leading to a different pulse shape. A clear separation between the (assumed to be) αs and other events is visible in Figure 7.7, although the PSD method was not yet optimized. On one hand this shows that the origin of the α events is indeed the p^+- electrode or the groove and on the other hand it allows to efficiently cut any α events which might appear in the region of interest.

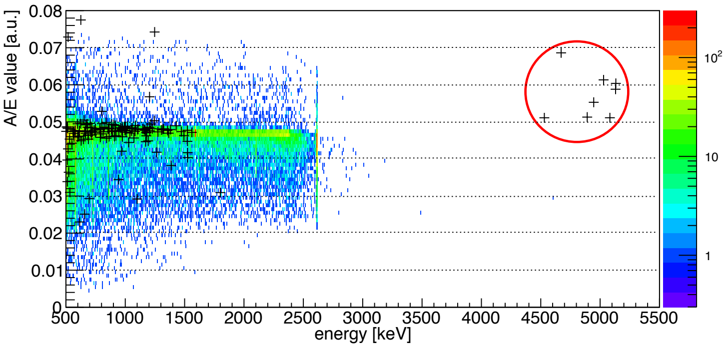

Figure 7.7: Event distributions for the pulse shape parameter A/E in dependence of energy in BEGe detector 89D in Run 50. Black crosses are events from the background measurement whereas coloured squares are from a prior calibration with a ^{228}Th source. The band visible in both distributions just below A/E = 0.05 is called the single-site band (see [68, 104]) in which the $\beta\beta$ events are expected. The high energy events (> 4 MeV) in the background measurement lie significantly above this band as expected from dedicated measurements (see [103]).

Chapter 8

First data from GERDA Phase II

In December 2015 all 40 detectors planned for use in GERDA Phase II were mounted into strings, equipped with transparent mini-shrouds and immersed in the cryostat by the integration team. Figure 8.1 shows the detector array before the lock was closed and its subsequent immersion. 30 BEGe with 20 kg, seven enriched coaxial (15 kg) and three natural coaxial (7 kg) detectors were deployed. A total exposure of 3.3 kg·yr (approx. one month of data taking) was used for this first analysis. For all analyses shown here the usual quality, muon veto and detector anti-coincidence cuts were applied (see Section 7.2). An overview background spectrum, as released by the GERDA collaboration at the time of writing, taken by all enriched detectors in the energy region between 200 - 1800 keV is presented in Figure 8.2.

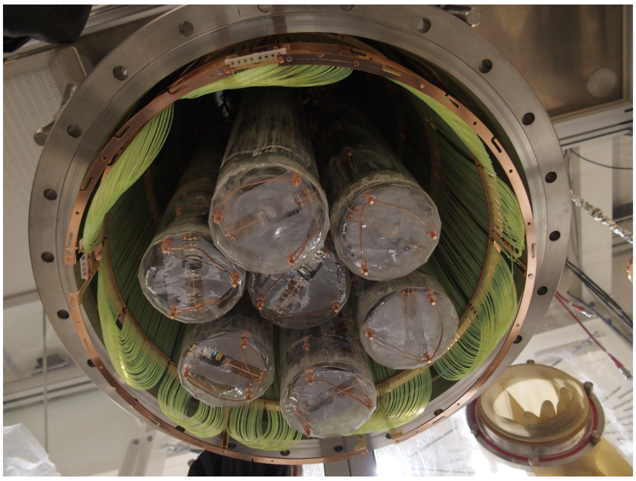

Figure 8.1: The full 40 detector GERDA array before closing the lock shown from below.

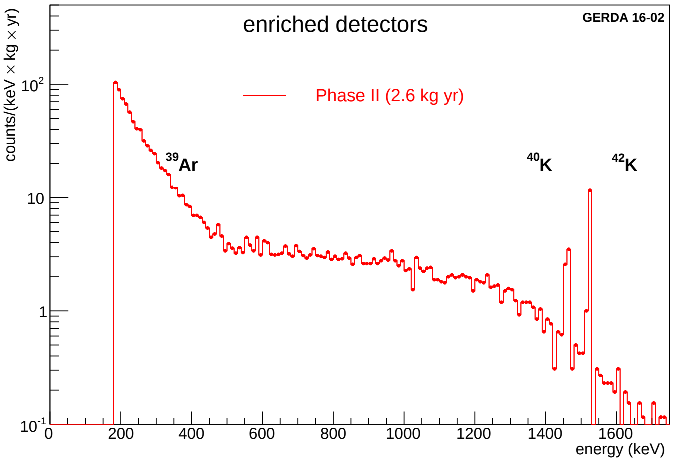

Figure 8.2: Background spectrum taken by all enriched detectors at the start of Phase II. The continuum of the ^{39}Ar β decay is well visible as well as the two γ-lines from ^{40}K and ^{42}K.

Data set	FWHM ZAC [keV] BEGe	FWHM ZAC [keV] coaxial
Phase I	$2.8^{+0.1}_{-0.1}$	$4.3^{+0.4}_{-0.3}$
Phase II (run 56)	$3.2^{+1.2}_{-0.4}$	$3.7^{+0.3}_{-0.2}$

Table 8.1: Comparison of mean energy resolution at 2.6 MeV during Phase I [93] and start of Phase II [105] for BEGe and coaxial detectors.

8.1 Performance of the detector array

After the immersion all 40 detectors could be put to operational voltage and no faulty electric connections (bonds, cables) occurred. Hence all detectors are usable for data taking. The energy resolution during ^{228}Th calibrations for the start of Phase II and, for comparison, in Phase I is reported in Table 8.1. For the coaxial detectors a significant improvement in Phase II is seen. This can be attributed to a much improved electrical connection of the diode to the high voltage line via the metallization and the bonding (see Section 2.6.2 and [64]). Other remaining noise contributions are removed effectively by the ZAC filter (see [93]). Reasons for the worse mean energy resolution of the BEGe detectors in Phase II with respect to Phase I are not clear at the moment but under investigation.

8.2 Spectral analysis of first physics data

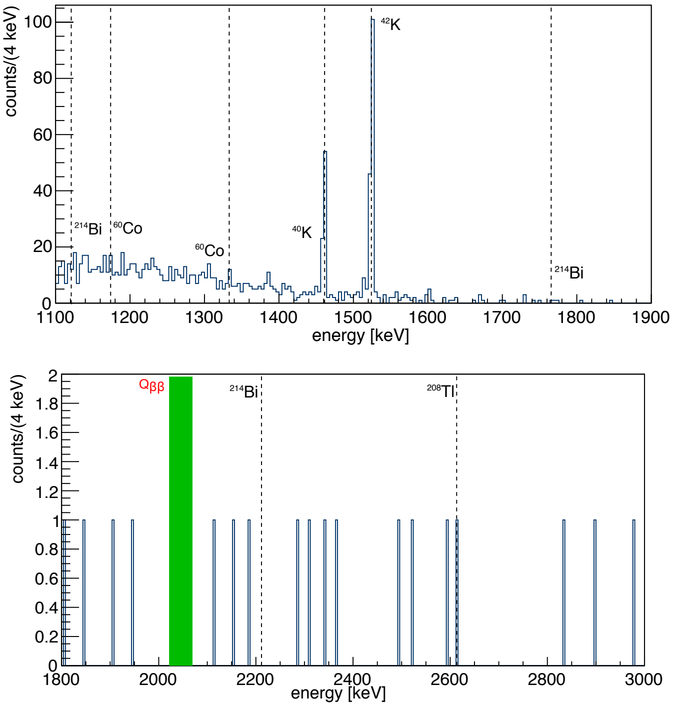

Figure 8.3: BEGe background spectrum after muon and anti-coincidence cut with an exposure of 1.6 kg·yr . Relevant γ lines are indicated as well as $Q_{\beta\beta}$ and the 50 keV blinded region.

Figures 8.3 and 8.4 show the background spectra from 1100 - 3000 keV for BEGe and coaxial detectors respectively. As expected the ^{42}K line is most prominent. Second in strength and stronger than in Phase I or the commissioning runs is the ^{40}K line. γ-lines with lower rates cannot be unambiguously identified yet due to the limited statistics although there are indications for low energy ^{214}Bi lines. As in Phase I and the commissioning the continuum between 400 - 1400 keV is dominated by $2\nu\beta\beta$. Table 8.2 gives a quantitative overview of the relevant γ-lines for BEGe, enriched coaxial and natural coaxial detectors. It is obvious that the latter record a significantly higher γ-line count rate. A possible reason is their position in the array. Since they are located in the central string, their field of view for close-by contaminations (holders, cables from other strings) is much larger.

In Figure 8.5 the γ-line rates for Phase I, commissioning and the start of Phase II are compared for BEGe and enriched coaxial detectors. With respect to Phase I and the commissioning runs the count rate in the ^{40}K line increased significantly. Though the

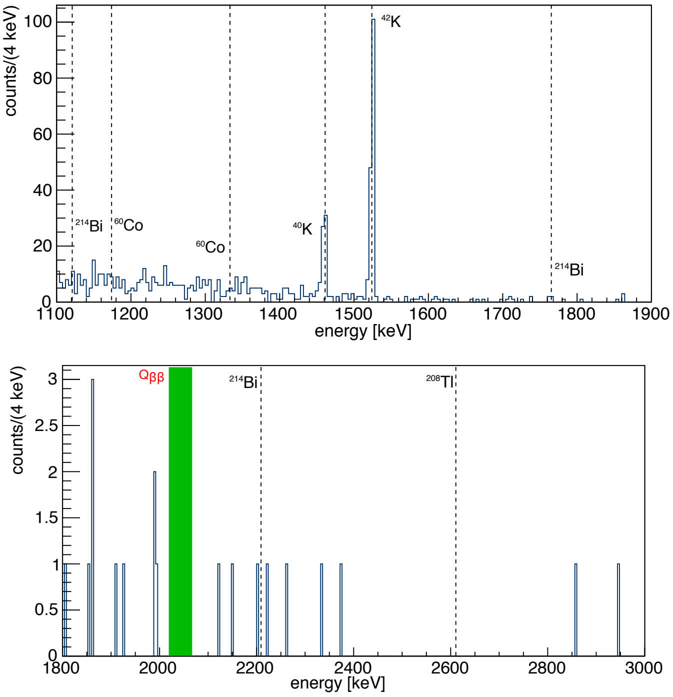

Figure 8.4: Coaxial detector background spectrum after muon and anti-coincidence cut with an exposure of 1 kg·yr . Relevant γ-lines are indicated as well as $Q_{\beta\beta}$ and the 50 keV blinded region.

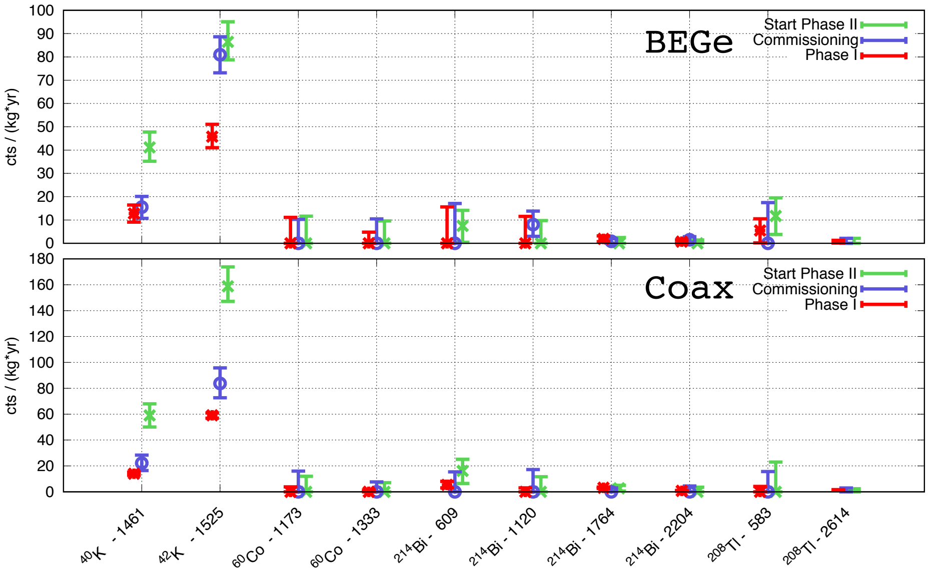

Figure 8.5: Overview of γ-lines in Phase I, commissioning and very first physics runs of Phase II.

		BEGe (1.62 kg·yr)		enrCoaxial (0.97 kg·yr)		natCoaxial (0.72 kg·yr)	
isotope	energy [keV]	tot/bkg [cts]	rate [cts/kg·yr]	tot/bkg [cts]	rate [cts/kg·yr]	tot/bkg [cts]	rate [cts/kg·yr]
^{40}K	1460.8	84/16	41^{+7}_{-6}	67/9	59^{+9}_{-9}	75/7	92^{+15}_{-11}
^{42}K	1524.7	157/15	86^{+9}_{-8}	159/3	159^{+15}_{-12}	104/7	133^{+15}_{-14}
^{60}Co	1173.2	58/56	< 12	34/39	< 12	16/18	< 12
	1332.5	32/28	< 10	16/23	< 7	20/9	15^{+7}_{-8}
^{214}Bi	609.3	119/107	$7.5^{+6.7}_{-7.1}$	57/42	16^{+9}_{-10}	20/17	< 17
	1120.3	52/54	< 10	30/33	< 12	24/15	12^{+8}_{-8}
	1764.5	2/2	< 2	4/1	$2.7^{+2.3}_{-2.1}$	3/0	$3.1^{+3.2}_{-2.1}$
	2204.5	0/0	< 1	1/0	< 4	2/0	$1.9^{+2.4}_{-1.7}$
^{208}Tl	583.2	115/96	12^{+8}_{-8}	60/53	< 23	14/23	< 9
	2614.5	1/0	< 2	0/0	< 2	0/0	< 3

Table 8.2: Table of γ-lines relevant for GERDA as measured during the first physics runs of GERDA Phase II. "tot" is counted in a 16 keV window centered on the given decay energy. "bkg" is counted in two 8 keV regions adjacent (lower & higher) to the "tot" window. For the rates the global mode and the 68 % smallest C.I. are given, or in case where this contains 0 the 90 % quantile is reported as a limit.

origin of this increase is not known at the moment this is not a major problem since the ^{40}K decay is not a background at $Q_{\beta\beta}$.

γ-line from ^{42}K decay

The count rates for ^{42}K are systematically higher for Phase II commissioning as well as for the analysed Phase II physics runs. As already mentioned in Section 7.2 this might be due to a higher geometrical detection efficiency. A possible mechanism would be that ^{42}K ions (from the ^{42}Ar decay) are attracted to the detectors by the bias voltage generated electric field. In Phase I this electric field was shielded by the copper mini-shrouds and by copper shielding around the HV cables, in Phase II the nylon shrouds do not shield the electric field and the ions could accumulate on the outside of the shroud (just 1- 2 cm away from the detectors), and the unshielded HV cables, and decay under the emission of a γ and a β. In itself this γ does not constitute a background at $Q_{\beta\beta}$, and the β is highly attenuated or stopped in LAr before it can deposit energy in the detector. The background induced by ^{42}K ions decaying inside the mini-shrouds has to be studied separately by pulse-shape analysis (see [62, 68]).

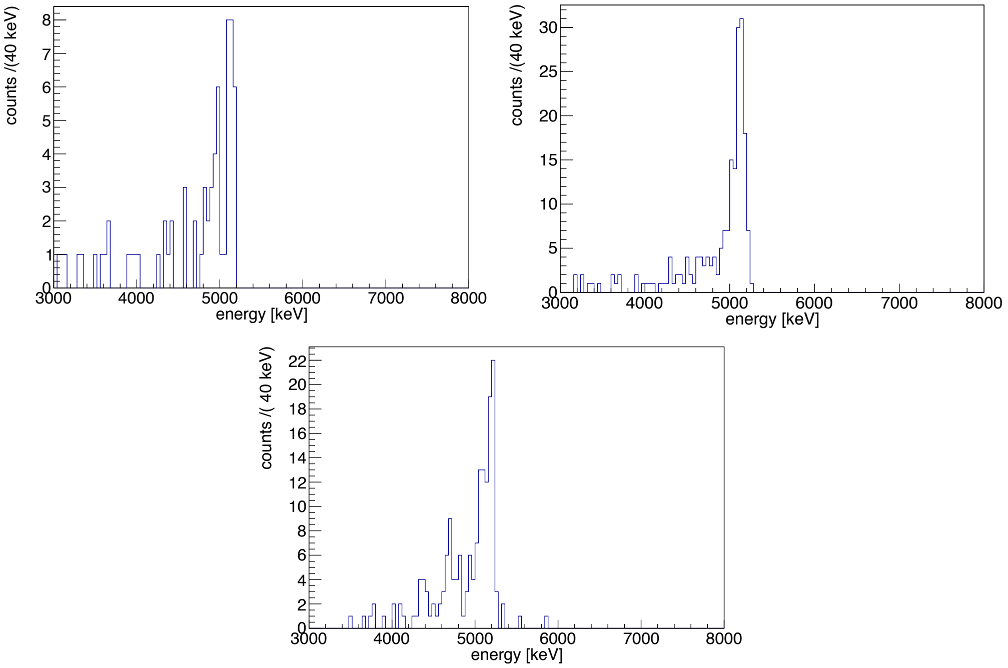

Figure 8.6: High energy (alpha) spectrum of BEGe, enriched coaxial and natural coaxial detectors respectively.

8.2.1 α count rate and contribution to background at $Q_{\beta\beta}$

As described in Section 7.2.1 high energy events (> 4 MeV) are with high certainty to due to α decays on the p^+- electrode or the groove. A bulk contamination would show a different spectral shape as well as a prompt-delayed event structure and is excluded with strong limits in [106]. Figure 8.6 shows the high energy spectra for BEGe, enriched and natural coaxial detectors.

Table 8.3 reports the high energy event rates during the commissioning runs and the physics run for the different detectors types. The count rates are in good agreement. Figure 8.7 shows that there is, especially between the different coaxial detectors, a large (order of magnitude) variation in the α count rate. This supports the idea that the contamination is not introduced by a specific process all detectors are subjected to and that the contamination does happen randomly. In Table 8.4 α rates for detectors used in all commissioning runs and physic runs are compared. One coaxial detectors shows a significantly lower count rate (ANG 5), whereas the BEGe detectors (except 89D) show a low but comparable rate. The decrease could be explained by the time elapsed since the last major handling either at the manufacturer site or in the much cleaner environment of the GERDA experiment.

	Run 50 - 52	Run 53 - 56
Livetime [d]	77.7	34.8
# BEGe	7 - 21	24 - 29
# Coaxial	1 - 5	3 - 7
# nat. Coaxial	-	3
α in BEGe	87	55
α in Coaxial	240	191
α in nat. Coaxial	-	153
α in BEGe / det. / day	$0.08^{+0.01}_{-0.01}$	$0.06^{+0.01}_{-0.01}$
α in Coaxial / det. / day	$1.15^{+0.07}_{-0.07}$	$1.14^{+0.08}_{-0.08}$
α in nat Coaxial / det. / day	-	$1.47^{+0.13}_{-0.11}$

Table 8.3: Overview of α counts and rates during the commissioning runs and during the first physics runs with number of detectors active (#) and number of α measured in the different detector types. The overall rate is weighted by livetime and number of detectors (detector · days). The uncertainties are given at the 68 % probability level.

Diode	cts	rate/d Run 50 - 52	cts	rate/d Run 53 - 56
ANG5	87	$1.13^{+0.12}_{-0.12}$	7	$0.45^{+0.19}_{-0.15}$
RG2	17	$0.38^{+0.10}_{-0.09}$	9	$0.57^{+0.21}_{-0.17}$
35C(pass)	2	$0.02^{+0.03}_{-0.01}$	1	$0.03^{+0.04}_{-0.02}$
00D(pass)	4	$0.05^{+0.03}_{-0.02}$	1	$0.03^{+0.04}_{-0.02}$
89D	17	$0.22^{+0.06}_{-0.05}$	3	$0.09^{+0.06}_{-0.05}$
76C	6	$0.08^{+0.04}_{-0.03}$	0	$0^{+0.03}_{-0.0}$

Table 8.4: α rates in different detectors in the commissioning runs and in the physics runs. For BEGe (except 89D) the rates do not differ significantly between commissioning and physics data taking. For ANG5 and 89D a decrease is seen.

Between the middle of first commissioning run where ANG 5 was used (Run50) and the middle of the analyzed physics runs (Run53 - 56) ca. 150 days have passed. Comparing the count rate of ANG 5 in Run50 ($\sim 1^{+0.2}_{-0.2}$) and the count rate in the physics runs ($\sim 0.5^{+0.2}_{-0.2}$) an approximate factor of two is found. The half life of ^{210}Po is 138 d which is in rough agreement with the time elapsed. For 89D the same behaviour can be seen.

In the commissioning data there is a hint that BEGe detectors with passivation layer have a smaller α count rate. The same investigation was performed for the physics data and is presented in Figure 8.8. Although the statistic is still small (19 detectors in this analysis) a similar difference in distributions as in the commissioning data is observable. As described in Section 7.2.1 the reason for this behaviour is not understood since e.g., the thickness of the passivation layer is not large enough to completely shield from the αs.

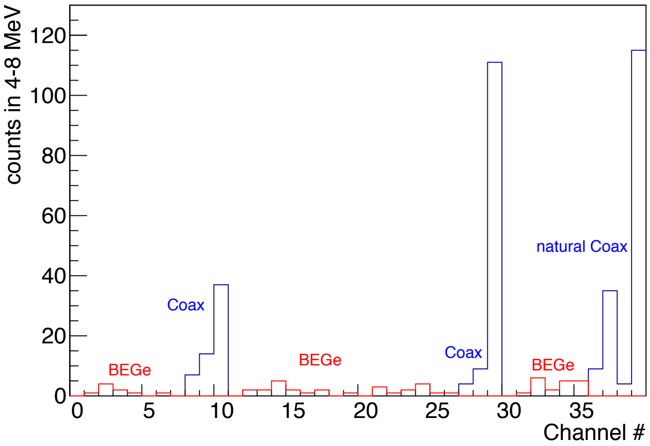

Figure 8.7: Distribution of high energy events (αs) in different channels/detectors during the first physics runs. Coaxial channels are in blue histograms, BEGe channels red. For channel mapping to individual detectors see Appendix C. A significant difference between BEGe and coaxial is visible as well as a large variation among the coaxial detectors.

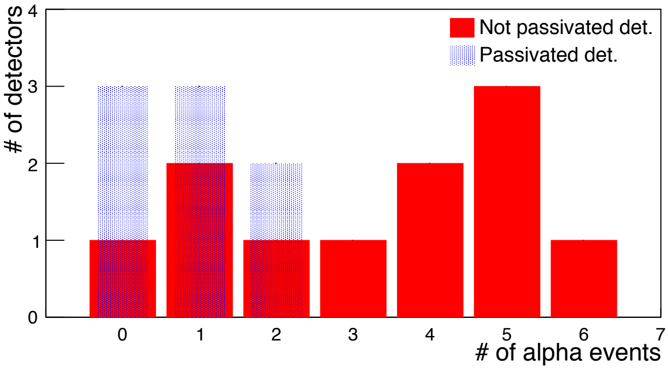

Figure 8.8: Comparison of α count distributions between passivated and non-passivated detectors in during the first physics runs. The number of α events in individual detectors (x-axis) and the occurrence (number of detectors, y-axis) is shown. A difference in the distributions is observed.

In the next section the possible background contribution of the observed α contamination is discussed.

Events in region of interest from ^{210}Po

In Section 6.2 the probability of a ^{210}Po α decay on the p^{+}- electrode to appear in the region of interest ($Q_{\beta\beta}\pm200$ keV) was simulated and found to be between 0.14 - 0.25 % according

Data set	Probability $Q_{\beta\beta}\pm 400\,\mathrm{keV}$	Probability peak	Counts in peak BEGe	Coaxial	BI [10^{-3} cts/(keV·kg·yr)] BEGe	Coaxial
Commissioning	0.14 - 0.25 %	37 - 43 %	67	108	0.3 - 0.6	0.5 - 1.1
Physics	0.14 - 0.25 %	37 - 43 %	42	146	0.2 - 0.4	1.2 - 2.5
Physics w/o ANG4	0.14 - 0.25 %	37 - 43 %	42	57	0.2 - 0.4	0.6 - 1.3

Table 8.5: ^{210}Po α counts in the peak and resulting background index for commissioning and first physics data.

to the deadlayer thickness assumed (the exact thickness is not known, see Section 6.2 and [62, 66]). Since the true value of α decays is unknown, the number of events in the peak-region (4.8-5.3 MeV) can be used as a proxy for comparison. From the simulations the ratio between peak events and the region of interest events can be extracted. In Table 8.5 the values from simulations and measurements are shown as well as the resulting background index for coaxial and BEGe detectors for both the commissioning and the physics data taking. For the physics data taking the background contribution from ^{210}Po α decays for the BEGe detectors is found to be lower than 10^{-3} cts/(keV·kg·yr) whereas for the coaxial detectors it is on the order of 10^{-3} cts/(keV·kg·yr). If the exceptionally α contaminated detector ANG 4 (ch 29) is not considered, the background index drops by a factor of two. In Phase I the event rate of ^{210}Po reduced exponentially according to the short half life of 138 d. Hints for this behaviour are already seen (see Table 8.4). Thus the impact on the background in the region of interest will decrease over time. In addition it was shown in [68, 103] that this kind of event can be well discriminated by pulse shape analysis. More dangerous are possible contributions from the ^{226}Ra chain isotopes with higher energies than α from ^{210}Po. In the current physics data set (enriched detectors only) only one such event was found. A quantitative analysis of the background contribution of such high energy αs is not possible at the moment. The very high energy events can used to set a limit on the ^{228}Th and ^{226}Ra contamination of the metallization which will presented in the next section.

8.2.2 Limit on the α activity originating from the metallization

The aluminium used for making the metallization was screened only via the ICP-MS method which is sensitive to ^{238}U and ^{232}Th but not directly to the relevant isotopes ^{226}Ra and ^{228}Th. As presented before (Section 2.6.1) to quantify the amount of ^{226}Ra and ^{228}Th secular equilibrium must be assumed. With the acquired data a limit on the ^{226}Ra and ^{228}Th activity can be set. This is performed by looking for high energy events above the

^{210}Po peak (5.3 MeV) since ^{226}Ra and ^{228}Th have in total seven shortlived daughter isotopes (i.e., ^{218}Po, ^{214}Po in case of ^{226}Ra [1] and ^{224}Ra, ^{220}Rn, ^{216}Po, ^{212}Bi, ^{212}Po in case of ^{228}Th) which decay under the emission of an α with a much higher Q-value than ^{210}Po. In the combined BEGe dataset of commissioning and physics runs (1952 detector $\cdot$ days corresponding to 3.6 kg·yr) only one such very high energy event has been recorded. The metallization on the α sensitive surface has a mass of 20 μg per detector. A 50% detection efficiency per each of the several isotope decays is assumed for geometrical reasons. The 90 % limit on the total activity is calculated to be

$$A(\mathrm{Bq/kg}) < 1.4\,\mathrm{Bq/kg} \quad 90\,\%\ \mathrm{C.I.}. \tag{8.1}$$

In Table 6.3 the ^{226}Ra and ^{228}Th activities of the different aluminium qualities used, calculated from ICP-MS measurements, were given. The total high energy α activity ($>$ 5.3 MeV) of the less radio pure material expected from the ^{226}Ra-subchain is 1.1 Bq/kg. This is calculated by ^{226}Ra activity (0.55 Bq/kg) $\times$ number of shortlived high energetic isotopes, in this case two. From the ^{228}Th-subchain it is 1.4 Bq/kg (0.27 Bq/kg $\times$ 5). The combined activity (2.5 Bq/kg) is lower than the limit extracted from the data. A significantly higher contamination of the aluminium with ^{226}Ra and ^{228}Th than inferred from ICP-MS measurements (broken secular equilibrium) can be excluded. The entire activity limit calculation of course assumes that the observed single high energy event originates from the metallization. In Phase I the BEGe data set (with an exposure of 1.8 kg·yr, ca. 50% of the current data set) included three such events without any metallization. Dissolved radon and its daughters in the liquid argon can produce these high energy events and is potentially more dangerous for the background in the region of interest as shown in [66]. The limit set is thus very conservative with respect to a possible metallization contamination and there is no indication that the metallization introduces any measurable background.

---

[1] ^{222}Rn has a Q-value too close (0.2 MeV) to the one of ^{210}Po.

Chapter 9

Summary and outlook

The aim of this thesis was the development and implementation of a novel contacting technique for HPGe detectors in the context of the ultra-low background experiment GERDA. This contacting solution was successfully implemented and is currently being used in Phase II of the GERDA experiment. First data from the detector array was analyzed with focus on possible contaminations introduced by the contacting technique. Thanks also to the contributions of this work, the current Phase II will have the sensitivity to probe the neutrinoless double beta ($0\nu\beta\beta$) decay up to half life values of 10^{26} yr.

The neutrinoless double beta decay is a lepton number violating process and if observed would prove the Majorana nature of the neutrino. It is only observable in isotopes where the single beta decay is forbidden. Current limits on the half life are in the 10^{25} yr range. The expected signal rates are thus extremely low making ultra-low background experiments necessary. One sensitive approach is to use high purity germanium (HPGe) detectors, isotopically enriched in the $0\nu\beta\beta$-isotope ^{76}Ge. The GERDA experiment uses bare HPGe detectors immersed in liquid argon for cooling and shielding against external radiation. Special attention has to be paid to the radio-purity of structures close to the detectors, e.g., detector holders and cables.

In the successfully completed GERDA Phase I an unexpected high ^{228}Th and ^{214}Bi related background had been found motivating a redesign of the detector holder and other structures in the detector array. A change of the detector contacting technique was called for to allow for the extensive use of ultra radio-pure, but mechanically unfavorable, materials, e.g., silicon, in the detector holder structure. The favoured method was wire bonding which prior to this work had not been commonly used on large volume germanium diode detectors. This method consists of the metallization processing of already produced HPGe detectors and of the actual wire bonding process for the electrical connection.

Wire bonding is a well established contacting technique in the semiconductor industry and for (research) silicon detectors (e.g., vertex trackers) but is unusual for HPGe detectors. The main task of this thesis was to develop and implement a robust wire bonding process (including the metallization) that fulfils the GERDA specific requirements. These are the survival of bond connections during handling and mounting of the detectors as well as during repeated thermal cycling in cryogenic liquids. The use of low background materials and processes to meet the strict background requirements of GERDA is obligatory. In addition, the sensitive detector signal electrode must not be damaged by the metallization and the subsequent bonding. Finally, the bonding process itself has to be performed in a glove box filled with gaseous nitrogen, restricting the access and usage of the bonding machine. The wire bonding process itself was designed in the following way. Ultrasonic bonding was used to bond 25 μm thick AlSi1% wire to a pure aluminium metallization, directly applied on both of the detector electrodes. The second bond was made on flexible cables connecting the detector to the HV supply and the front-end electronics. The process was characterized according to industry standards, e.g., visual inspection and pull strength tests. The detector metallization presented a well bondable substrate (bond pad), see below. In contrast, the flexible cables, which are under strict radio purity constraints, proved to be less bondable. Several different designs were tested and a compromize between radio purity and bonding strength had to be made.

For a successful wire bonding the detector electrodes needed to be partly metallized to provide a well bondable substrate (bond pad), an ohmic contact and a protection layer for the sensitive signal electrode. In addition, the metallization has to fulfil the following requirements: good adhesion to the underlying doped germanium and radio-purity. The metallization process was designed in such a way that it could be easily integrated into the existing production process of the high purity germanium detectors at the manufacturer Canberra Semiconductor NV. The metallization is provided as a thin film produced in a high-vacuum evaporation machine. For a first charaterization of these films in terms of adhesion under thermal cycling and bonding as well as ohmic behaviour high purity germanium samples doped either with boron or lithium were used. After promising results a small but fully functional detector was metallized, bonded and tested for its spectroscopic performance. Several normal scale prototype detectors were metallized at the manufacturer according to the defined process protocol. This protocol included an etch of the rough lithium doped surface, an in-situ ion sputter cleaning followed by the application of the thin film and a standard diode current-voltage measurement as an acceptance test.

The such processed prototype detectors were extensively used in the so-called “detector integration tests” where the handling and mounting as well as the front-end electronics and the operation of the entire assembly was tested and refined. After the successful testing all 40 GERDA detectors underwent the metallization process where special attention was paid to a short exposure above ground to avoid cosmogenic activation of the detectors.

In addition to the detector related work, first steps towards the in-house fabrication of ultra-low background electronic components were performed. To improve the energy resolution of the detector array, a closer positioned front-end electronics is desired, reducing stray capacitances, pick-up noise and cross-talk. High radio-purity electronic components are essential for this approach. One important component is the so-called feedback resistor since the commercial availability of radio-pure devices is limited. Amorphous germanium is known to be a good candidate material for a production of such a device. High resistance ($> 500\,\mathrm{M\Omega}$), ohmic, amorphous, thin films were successfully produced in-house at TUM. However, an increase of resistance over time was observed for all produced resistors. Similar resistors provided by another group exhibited a similar behaviour. Different treatments and storage conditions were tested to prevent this change of resistance. The likely cause of the increase is a restructuring of the Ge atoms within the film. A storage at temperatures of -15°C have been found to mitigate the increase. Future work would include a resistor fabrication on ultra radio-pure quartz substrates.

The commissioning of the GERDA Phase II detector array started in July 2015. Preparatory works included the “integration” of the individual germanium diodes into a detector holder together with the flexible cables where then the wire bond connection was applied. Later, the detectors were assembled in the array structure. All works were carried out in the frame of the so-called “detector integration team”. Three commissioning runs were performed with different number of detectors and configurations used. In the course of these runs some detectors (facing upwards) were found that could not be put to the operational voltage due to excessive leakage currents. The detector holder design was changed such that no more detectors would face with the “groove” upwards. This design change increased the fraction of working detectors per immersion significantly to $\sim$100 %. A second item concerned the way the flexible cables were routed to the front-end electronics and the HV supply line. Before the change a significant pull force was applied on the cable. This pull force was in a few cases too high for the small mass and radio-pure cable fixation causing movement and subsequent bond failure. This occurred two times before the routing procedure was modified. After this modification no more broken bonds were observed with a statistics of approx. 400 bonds immersed in liquid argon.

After the successful commissioning, the full GERDA detector array was assembled and in December 2015 immersed in liquid argon for the first Phase II physics data taking. 30 BEGe type detectors with a total mass of 20 kg and seven coaxial detectors with 15 kg, all made from germanium enriched in ^{76}Ge, were deployed. In addition three natural coaxial detectors with mass of 7 kg are used.

The contacting performance during the commissioning and the start of physics data taking was excellent. During the last test immersions of the assembled detector array only 0.3 % of the bonds were found to be broken. In the final immersion no faulty electrical connection occurred signifying the robustness of the developed bonding process. All detectors deployed were in working condition. The energy resolution during calibration measurements of the coaxial detectors is much improved with respect to Phase I (from 4.3 keV at the 2.6 MeV line down to 3.7 keV). This is attributed to a better electrical connection of the HV supply to the detectors via the bond contact. For the BEGe detectors a worsening of the resolution is observed (from 2.8 keV to 3.2 keV) whose origin is unclear at the moment. The requirement of robustness and reliability was clearly met.

In order to estimate the background induced by the contacting technique in the region of interest (ROI) around $Q_{\beta\beta}$ several Monte-Carlo simulations were performed. The MAGE framework was used to simulate an idealized detector array and different source positions. Two γ-decaying isotopes of the ^{238}U and ^{232}Th chains (^{214}Bi and ^{208}Tl) are most dangerous in terms of background. Both were simulated with high statistics and the probability to observe an event in the ROI was extracted before and after an detector anti-coincidence cut was applied. The line strengths of important γ-lines were also determined. Assuming the extracted probabilities and the material activities known from screening measurements, the total γ background due to the contacting technique was estimated to be 3×10^{-6} cts/(keV·kg·yr). In addition, a simulation of a ^{210}Po contamination was performed. It was known from Phase I that ^{210}Po represents a non-negligible surface contamination on the HPGe detectors. A contribution to the background at $Q_{\beta\beta}$ by the high energy α ($\sim$ 5.3 MeV) is possible since during the traversing of a thin non-active (dead) layer the α can lose a substantial amount of energy (“degrade”). The probability for an degraded α to deposit energy in the ROI increases with increasing thickness of the deadlayer. The simulation results were later used in conjunction with data to estimate the impact of the ^{210}Po contamination on the background.

An analysis of the acquired data (commissioning and physics runs) was performed with focus on the γ-lines of ^{40}K, ^{42}K, ^{60}Co, ^{214}Bi and ^{208}Tl and α induced high energy events. With the limited exposure (6.6 kg·yr) significant count rates were found at 583 keV

(^{208}Tl), 609 keV (^{214}Bi), 1525 keV (^{42}K), 1461 keV (^{40}K), and 2205 (^{214}Bi). The total spectrum showed no new features (lines) compared to Phase I. The strength of the ^{40}K line increased with respect to Phase I. This is an indication for an additional contamination but this line does not pose a background at $Q_{\beta\beta}$. A higher count rate of the 1525 keV line with respect to Phase I, possibly due to a different electrical field configuration, was measured as well. Also this line is not a background at $Q_{\beta\beta}$[1]. The high energy α events were identified to originate, almost exclusively, from ^{210}Po as observed in Phase I. The contamination varied significantly among the individual detectors and between the two detector types with coaxial detectors showing a factor of $\sim$ 10 more αs than the BEGe type detectors. This can be explained by the $\sim$ 10 times larger α sensitive surface of the coaxial detectors. The BEGe detectors exhibited a difference between passivated (less α) and non-passivated detectors (more α). The origin of this observation is not clear at the moment. A comparison of commissioning and physics data showed that the averaged α rates stayed approximately the same where a few detectors showed a smaller α rate in the physics data and a few, newly introduced, showed a higher rate.

Among the coaxial detectors one newly introduced detector (ANG 4) is responsible for more than half of the recorded α events in the physics data. The background contribution of the observed ^{210}Po decays can be estimated by a comparison to the degraded α simulations mentioned above. For the BEGe detectors this is estimated to be much below 10^{-3} cts/(keV·kg·yr) which will be further improved by an application of an efficient pulse-shape discrimination cut. For the coaxial detectors the background contribution is estimated to be 0.6 - 2.5 $\cdot$ 10^{-3} cts/(keV·kg·yr) depending on the actual deadlayer thickness and if ANG 4 is considered or not. Since the ^{210}Po has a half life of 138 d the contribution is expected to decrease. An indication for this is seen as discussed briefly above. In addition, also for the coaxial detectors a pulse-shape cut, although less efficient, will be applied. A surface contamination with other daughter isotopes from the ^{238}U and ^{232}Th chain was not observed with the current data set. A limit on the combined ^{226}Ra and ^{228}Th (plus daughter isotopes) contamination in the used metallization material was calculated. A significantly higher contamination of the aluminium with ^{226}Ra and ^{228}Th than inferred from ICP-MS measurements (broken secular equilibrium) can be excluded. In conclusion, the observed randomness of the amount of contamination shows that there is no indication that the additional processing and material required for the bond contacting introduced any further contamination on the surface of the detectors.

The developed and tested contacting technique has been successfully applied to all 40

---

[1] The β of this decay is well shielded by a foil surrounding the detectors.

GERDA detectors. These are used in Phase II which is currently taking data. Depending on the exact background index and composition the GERDA Phase II will reach a sensitivity of $\mathcal{O}(10^{26})$ yr in approximately three years of live time, making it one of the most sensitive experiments to date. A possible upgrade would feature 200 kg of detector mass, which corresponds to 200 - 300 individual detectors. The necessary “mass” production of detectors is not influenced by the metallization processing since the amount of additional processing steps and time is not significant (few hours) with respect to the total production. If some production steps are required to be performed underground, to avoid cosmic exposure, the metallization process can easily be transferred since no dangerous materials (e.g., flammable gases) are used. The background introduced by the contacting is on the order of 10^{-6} cts/(keV·kg·yr), at least two orders of magnitude lower than required. 6N aluminium, with radio-purity limits from screening, brings negligible background ($< 10^{-7}$ cts/(keV·kg·yr)) and was already partly used as metallization. An effort has to be made to develop and test radio-pure cables which present a better bondable substrate. An alternative would be the separation of second bond pad and cable, allowing an individual optimization of both parts. The presented contacting technique with wire bonds is very well suited for the use in a next generation ^{76}Ge experiment where hundreds of individual detectors would be deployed.

Appendix A

Screening results

Table A.1 presents the ICP-MS screening results of the two aluminium qualities used and the used bond wire procured from the tpt company. Table A.2 shows a comparison of achieved limits between the ICP-MS measurement and a γ-spectroscopy measurement at TUM. Thanks to A. Lazzaro for performing the spectroscopy. Especially for ^{226}Ra the limits are comparable which excludes a significantly broken secular equilibrium. This comparison measurement is unfortunately not possible for the bondwire since the amount of material is minuscule. A roll of 100m has a mass of just 0.13 g. Afterwards the wire would be not usable anymore.

Material	^{232}Th conc. $[10^{-9}$ g/g]	^{238}U conc. $[10^{-9}$ g/g]	^{228}Th act. [mBq/kg]	^{226}Ra act. [mBq/kg]	activity per detector
MaTecK 6N	< 0.5	< 1	< 2.7	< 16	< 380 pBq
Balzers 4N	50	35	270	550	33 nBq
tpt bond wire	13.5	3.5	73	54	7 nBq

Table A.1: ICP-MS results and calculated activities per kg and per detector for two different aluminium qualities (4N and 6N) and tpt 25μAlSi1% bond wire. The material masses are 40 μg and 50 μg respectively. Relative uncertainties are approx. 30 % and limits are 95 %C.L. [84].

Method	^{228}Th act. [mBq/kg]	^{232}Th conc. [10^{-9} g/g]	^{226}Ra act. [mBq/kg]	^{226}Ra conc. [10^{-9} g/g]	^{238}U conc. [10^{-9} g/g]
ICP-MS	2.7	0.5	16	1	1
γ-ray	44	10	20	1.6	81

Table A.2: Comparison ICP-MS (at LNGS) and γ-ray screening of MaTecK 6N material at TUM UGL (GEM detector) with 75 g sample mass and 340 h measurement time. All limits.

Appendix B

Detector logistics during metallization processing and transport to LNGS

All 30 enriched BEGe detectors were produced and tested in vacuum cryostat with a passivation layer applied. Five were deployed in GERDA while the others were stored underground in the HADES facility close to the manufacturer site. From the collaboration it was wished that all detectors would have the passivation layer removed as those had been found to bring operational problems in liquid argon [64]. The time slot chosen for this was the metallization processing. This processing included, as described in detail in Chapter 4, the removal of the passivation layer, subsequent metallization, a final groove etch and an acceptance leakage current test in LN_2. As found before by the manufacturer, it was not guaranteed that without the passivation layer the detector would work immediately. Sometimes more than one etching of the groove was required regardless if the diodes was metallized before or not. In Table B.1 the approximate above ground exposure times and the number of etchings for each BEGe detector are presented as well as the metallization material quality used. The exposure of the transport to LNGS is not included. Immediately before and during the commissioning runs a significant number of already accepted detectors showed high leakage currents. The reason for this is unclear. A reprocessing at the manufacturer was necessary. This included etching of groove and in three cases cases new doping (implantation) of the signal electrode. As the manufacturer was not able to reliably provide unpassivated detectors at that time, a passivation layer was admitted for the repaired detectors. This is indicated with “pass” in Table B.1. Exposures of this repair are not included in the table and are of the order 40 - 48 h, including the transport from LNGS to the manufacturer and back (ca. 32 h). In the pathogenic case of 00C 60 h exposure accumulated due to several needed reprocessings. The logistics key numbers for the metallization of the coaxial (enriched and natural) detectors are given in Tables B.2 and B.3, again without transport times to and from LNGS. Also here in some cases a new implantation and/or passivation layer were needed for acceptable leakage current. Since the exposure requirements of the natural detectors are less strict less effort was made to minimize the exposure.

Table B.1: Key numbers of BEGe detector logistics for metallization processing.

Detector ID	00A	00B	00C	00D	02A	02B	02C	02D	32A	32B	32C
Exposure [h]	14	7	16	14	8	16	7	15	16	8	20
# Etches	1	1	2	1	1	1	1	2	1	1	2
Aluminium	6N	4N	6N	4N	6N	6N	4N	6N	6N	6N	6N
Comments	pass	pass	pass,imp.	pass	pass	-	-	pass	-	-	-

Detector ID	32D	35A	35B	35C	61A	61B	61C	76B	76C	79B	79C
Exposure [h]	20	16	20	20	16	16	11	8	18	18	7
# Etches	1	1	1	1	1	2	2	1		2	1
Aluminium	6N	6N	6N	6N	6N	6N	4N	4N	4N	4N	4N
Comments	-	-	-	pass	pass	pass	-	pass	pass	-	-

Detector ID	89A	89B	89C	89D	91A	91B	91C	91D
Exposure[h]	22	8	8	7	13	10	18	7
# Etches	1	1	1	1	2	1	2	1
Aluminium	4N	6N	4N	4N	4N	6N	6N	4N
Comments	-	-	pass,imp.	-	-	-	pass,imp.	-

Table B.2: Key numbers of enriched coaxial detector logistics for metallization processing.

Detector ID	ANG 1	ANG 2	ANG 3	ANG 4	ANG 5	RG 1	RG 2
Exposure [h]	15	24	31	24	8	15	15
# Etches	1	2	5	3	1	1	2
Comments	-	pass	pass, new imp.	pass, new imp.	-	-	-

Table B.3: Key numbers of natural coaxial detector logistics for metallization processing.

Detector ID	GTF 32	GTF 45	GTF 112
Exposure [h]	80	40	23
# Etches	5	0	1
Comments	pass, new imp.	-	pass, new imp.

Appendix C

Setup of detector array during commissioning runs and physics runs

FADC Channel	0	1	2	3	4	5	6	NA	NA
Detector ID	ANG 5	RG 1	ANG 2	RG 2	02A	32B	32A	32C	61A
Status	OK	AC	AC	OK	AC	OK	OK	not conn.	not conn.
FADC Channel	NA	7	8	9	10	11	12	13	14
Detector ID	89C	00B	61B	35C	76C	35A	89D	91B	79C
Status	not conn.	OK	OK	OK	OK	OK	OK	AC	OK
FADC Channel	15	16	17	18	19	20	21	22	23
Detector ID	61C	00D	00A	02C	02B	35B	89A	32D	ANG1
Status	OK	OK	OK	OK	OK	OK	AC	AC	AC

Table C.1: Channel mapping of Run 50.

FADC Channel	0	1	2	3	4	5
Detector ID	ANG 5	RG 1	ANG 2	RG 2	35C	76C
Status	OK	OK	AC	OK	OK	OK
FADC Channel	6	7	8	9	10	11
Detector ID	35A	89D	91B	79C	61C	00D
Status	OK	OK	OK	OK	AC	OK

Table C.2: Channel mapping of Run 51.

FADC Channel	0	1	2	3	4	5	6	7	8	9
Detector ID	91A	35B	02D	02B	00B	ANG 5	RG 1	02A	32B	32A
Status	OK	OK	OK	OK	OK	OK	OK	OK	OK	OK

FADC Channel	10	11	12	13	14	15	16	17	18	19
Detector ID	32C	61A	89C	61B	35C	76C	89D	79C	61C	00D
Status	OK	OK	OK	OK	OK	OK	OK	OK	AC	OK

FADC Channel	20	21	22	23	24	25	26	27		
Detector ID	GTF45	00A	02C	79B	32D	ANG 1	ANG 2	RG 2		
Status	OK	OK	OK	OK	OK	OK	AC	OK		

Table C.3: Channel mapping of Run 52.

FADC Channel	0	1	2	3	4	5	6	7	8	9
Detector ID	91A	35B	02B	00B	61A	89B	02D	91C	ANG5	RG1
Status	OK	OK	OK	OK	OK	OK	OK	OK	OK	OK

FADC Channel	10	11	12	13	14	15	16	17	18	19
Detector ID	ANG3	02A	32B	32A	32C	89C	61C	76B	00C	35C
Status	OK	OK	OK	OK	OK	OK	OK	OK	OK	OK

FADC Channel	20	21	22	23	24	25	26	27	28	29
Detector ID	76C	89D	00D	79C	35A	91B	61B	ANG2	RG2	ANG4
Status	OK	OK	OK	OK	OK	OK	OK	OK	OK	OK

FADC Channel	30	31	32	33	34	35	36	37	38	39
Detector ID	00A	02C	79B	91D	32D	89A	ANG1	GTF112	GTF32	GTF45
Status	OK	OK	OK	OK	OK	OK	OK	OK	OK	OK

Table C.4: Channel mapping of Physics data taking.

Bibliography

[1] W. Pauli, *Dear radioactive ladies and gentlemen*, Phys. Today **31**, 27 (1978)

[2] C. L. Cowan, et al., *Detection of the free neutrino: A Confirmation*, Science **124**, 103 (1956)

[3] Y. Fukuda, et al., Super-Kamiokande Collaboration, *Evidence for Oscillation of Atmospheric Neutrinos*, Phys. Rev. Lett. **81**, 1562, URL `http://link.aps.org/doi/10.1103/PhysRevLett.81.1562` (1998)

[4] Q. R. Ahmad, et al., SNO Collaboration, *Direct Evidence for Neutrino Flavor Transformation from Neutral-Current Interactions in the Sudbury Neutrino Observatory*, Phys. Rev. Lett. **89**, 011301, URL `http://link.aps.org/doi/10.1103/PhysRevLett.89.011301` (2002)

[5] L. M. O. von Baeyer, O. Hahn, *Magnetische Spektren der Beta-Strahlen des Radiums*, Phys. Zeit. **12**, 1099 (1911)

[6] E. Fermi, *Versuch einer Theorie der β-Strahlen.*, Zeitschrift f. Phys. A (1934)

[7] G. Danby, et al., *Observation of High-Energy Neutrino Reactions and the Existence of Two Kinds of Neutrinos*, Phys. Rev. Lett. **9**, 36 (1962)

[8] DONUT collaboration, *Observation of tau neutrino interactions*, Physics Letters B **504**, 218 (2001)

[9] K. Nakamura, et al., Particle Data Group, *Review of particle physics*, J. Phys. **G37**, 075021 (2010)

[10] K. N. Abazajian, et al., *Light Sterile Neutrinos: A White Paper* (2012)

[11] R. Adhikari, et al., *A White Paper on keV Sterile Neutrino Dark Matter* (2016)

[12] J. Bahcall, et al., *Solar models, neutrino experiments, and helioseismology*, Rev. Mod. Phys. **60**, 297 (1988)

[13] R. Davis, Jr., et al., *Search for neutrinos from the sun*, Phys. Rev. Lett. **20**, 1205 (1968)

[14] P. Anselmann, et al., *Solar neutrinos observed by GALLEX at Gran Sasso*, Physics Letters B **285**, 376 (1992)

[15] K. Eguchi, et al., KamLAND Collaboration, *First Results from KamLAND: Evidence for Reactor Antineutrino Disappearance*, Phys. Rev. Lett. **90**, 021802 (2003)

[16] E. Aliu, et al., The K2K Collaboration, *Evidence for Muon Neutrino Oscillation in an Accelerator-Based Experiment*, Phys. Rev. Lett. **94**, 081802 (2005)

[17] N. Agafonova, et al., *Evidence for ν_μ ν_τ appearance in the CNGS neutrino beam with the OPERA experiment*, Physical Review D **89**, 051102 (2014)

[18] M. Gonzalez-Garcia, et al., *Updated fit to three neutrino mixing: status of leptonic CP violation*, Journal of High Energy Physics **2014**, 52, URL `http://dx.doi.org/10.1007/JHEP11%282014%29052` (2014)

[19] E. Akhmedov, et al., *Paradoxes of neutrino oscillations*, Physics of Atomic Nuclei **72**, 1363, URL `http://dx.doi.org/10.1134/S1063778809080122` (2009)

[20] S. Mikheyev, et al., *Resonance enhancment of oscillations in matter and solar neutrino spectroscopy*, Soviet Journal of Nuclear Physics **42**, 913 (1985)

[21] Y.-F. Li, et al., *Unambiguous determination of the neutrino mass hierarchy using reactor neutrinos*, Phys. Rev. D **88**, 013008, URL `http://link.aps.org/doi/10.1103/PhysRevD.88.013008` (2013)

[22] C. Kraus, et al., *Final results from phase II of the Mainz neutrino mass search in tritium β decay*, Eur. Phys. J. C **40**, 447, URL `doi:10.1140/epjc/s2005-02139-7` (2005)

[23] V. N. Aseev, et al., *Upper limit on the electron antineutrino mass from the Troitsk experiment*, Phys. Rev. D **84**, 112003, URL `http://link.aps.org/doi/10.1103/PhysRevD.84.112003` (2011)

[24] J. Angrik, et al., *KATRIN design report* (2004), fZKA-7090

[25] A. J. Cuesta, et al., *Neutrino mass limits: robust information from the power spectrum of galaxy surveys* URL `arxiv.org/abs/1511.05983` (2015)

[26] E. Majorana, *Symmetric theory of the electron and positron*, Nuovo Cimento **14**, 171 (1937)

[27] S. M. Bilenky, *Neutrinoless double beta-decay*, Phys. Part. Nucl. **41**, 690 (2010)

[28] S. M. Bilenky, et al., *Neutrinoless double-beta decay: A probe of physics beyond the Standard Model*, URL `http://arxiv.org/abs/1411.4791v1` (2015)

[29] M. Goeppert-Mayer, *Double Beta-Disintegration*, Phys. Rev. **48**, 512, URL `http://link.aps.org/doi/10.1103/PhysRev.48.512` (1935)

[30] S. R. Elliott, et al., *Direct evidence for two-neutrino double-beta decay in* ^{82}Se, Phys. Rev. Lett. **59**, 2020, URL `http://link.aps.org/doi/10.1103/PhysRevLett.59.2020` (1987)

[31] B. Schwingenheuer, *Status and prospects of searches for neutrinoless double beta decay*, Ann. Phys. (Berlin) **525**, 269 (2013)

[32] J. Beringer, et al., Particle Data Group, *Review of Particle Physics*, Phys. Rev. D **86**, 010001, URL `http://link.aps.org/doi/10.1103/PhysRevD.86.010001` (2012)

[33] J. Schechter, et al., *Neutrinoless double-β decay in SU(2)$\times$U(1) theories*, Phys. Rev. D **25**, 2951, URL `http://link.aps.org/doi/10.1103/PhysRevD.25.2951` (1982)

[34] G. Racah, *Sulla Simmetria Tra Particelle e Antiparticelle*, Il Nuovo Cimento **14**, 322, URL `http://dx.doi.org/10.1007/BF02961321` (1937)

[35] W. H. Furry, *On Transition Probabilities in Double Beta-Disintegration*, Phys. Rev. **56**, 1184 (1939)

[36] M. Doi, et al., *Double Beta Decay and Majorana Neutrino*, Progress of Theoretical Physics Supplement **83**, 1, URL `http://ptps.oxfordjournals.org/content/83/1.abstract` (1985)

[37] J. Engel, *Uncertainties in nuclear matrix elements for neutrinoless double-beta decay*, Journal of Physics G: Nuclear and Particle Physics **42**, 034017, URL `http://stacks.iop.org/0954-3899/42/i=3/a=034017` (2015)

[38] A. Giuliani, et al., *Neutrinoless Double-Beta Decay*, Adv.High Energy Phys. **2012**, 857016 (2012)

[39] K. H. Ackermann, et al., GERDA, *The GERDA experiment for the search of* $0\nu\beta\beta$ *decay in* ^{76}*Ge*, Eur. Phys. J. **C73**, 2330 (2013)

[40] J. J. Gomez-Cadenas, et al., *The Search for neutrinoless double beta decay*, Riv. Nuovo Cim. **35**, 29 (2012)

[41] R. Arnold, et al., NEMO-3 Collaboration, *Results of the search for neutrinoless double-*β *decay in* ^{100}Mo *with the NEMO-3 experiment*, Phys. Rev. D **92**, 072011, URL `http://link.aps.org/doi/10.1103/PhysRevD.92.072011` (2015)

[42] M. Auger, et al., EXO Collaboration, *Search for Neutrinoless Double-Beta Decay in* ^{136}Xe *with EXO-200*, Phys. Rev. Lett. **109**, 032505, URL `http://link.aps.org/doi/10.1103/PhysRevLett.109.032505` (2012)

[43] EXO collaboration, *Search for Majorana neutrinos with the first two years of EXO-200 data*, Nature **510**, 229, URL `http://dx.doi.org/10.1038/nature13432` (2014)

[44] J. Martin-Albo, et al., NEXT, *Sensitivity of NEXT-100 to neutrinoless double beta decay* (2015)

[45] K. Asakura, et al., *Results from KamLAND-Zen*, AIP Conference Proceedings **1666**, 170003, URL `http://scitation.aip.org/content/aip/proceeding/aipcp/10.1063/1.4915593` (2015)

[46] S. Andringa, et al., SNO+, *Current Status and Future Prospects of the SNO+ Experiment*, Adv. High Energy Phys. (2016)

[47] D. R. Artusa, et al., *Searching for Neutrinoless Double-Beta Decay of* ^{130}*Te with CUORE*, Advances in High Energy Physics (2015)

[48] K. Alfonso, et al., CUORE Collaboration, *Search for Neutrinoless Double-Beta Decay of* ^{130}Te *with CUORE-0*, Phys. Rev. Lett. **115**, 102502, URL `http://link.aps.org/doi/10.1103/PhysRevLett.115.102502` (2015)

[49] M. Vignati, *LUCIFER: Scintillating bolometers for the search of Neutrinoless Double Beta Decay*, Nuclear Physics B - Proceedings Supplements **229–232**, 495 , URL `http://www.sciencedirect.com/science/article/pii/S0920563212003490` (2012), neutrino 2010

[50] F. A. Danevich, et al., *Status of LUMINEU program to search for neutrinoless double beta decay of 100Mo with cryogenic ZnMoO4 scintillating bolometers*, AIP Conference Proceedings **1686**, 020007, URL `http://scitation.aip.org/content/aip/proceeding/aipcp/10.1063/1.4934896` (2015)

[51] N. D. Khanbekov, *AMoRE: Collaboration for searches for the neutrinoless double-beta decay of the isotope of 100Mo with the aid of 40Ca100MoO4 as a cryogenic scintillation detector*, Physics of Atomic Nuclei **76**, 1086, URL `http://dx.doi.org/10.1134/S1063778813090093` (2013)

[52] F. Alessandria, et al., *Validation of techniques to mitigate copper surface contamination in CUORE*, Astroparticle Physics **45**, 13 , URL `http://www.sciencedirect.com/science/article/pii/S0927650513000443` (2013)

[53] M. Willers, et al., *Neganov-Luke amplified cryogenic light detectors for the background discrimination in neutrinoless double beta decay search with TeO 2 bolometers*, Journal of Instrumentation **10**, P03003, URL `http://stacks.iop.org/1748-0221/10/i=03/a=P03003` (2015)

[54] H. Klapdor-Kleingrothaus, et al., *Latest results from the HEIDELBERG-MOSCOW double beta decay experiment*, Eur. Phys. J. A **12**, 147, URL `http://dx.doi.org/10.1007/s100500170022` (2001)

[55] H. V. Klapdor-Kleingrothaus, et al., *Evidence for Neutrinoless Double Beta Decay*, Mod. Phys. Lett. **A16**, 2409 (2001)

[56] H. Klapdor-Kleingrothaus, et al., *Search for neutrinoless double beta decay with enriched 76Ge in Gran Sasso 1990-2003*, Physics Letters B **586**, 198 , URL `http://www.sciencedirect.com/science/article/pii/S0370269304003235` (2004)

[57] C. E. Aalseth, et al., *Comment on 'Evidence for Neutrinoless Double Beta Decay'*, Mod. Phys. Lett. **A17**, 1475 (2002)

[58] N. Abgrall, et al., *The* MAJORANA DEMONSTRATOR *Neutrinoless Double-Beta Decay Experiment*, Advances in High Energy Physics (2014)

[59] M. Green, et al., *The* MAJORANA DEMONSTRATOR *for $0\nu\beta\beta$: Current Status and Future Plans*, Physics Procedia **61**, 232 , URL `http://www.sciencedirect.com/science/article/pii/S1875389214006518` (2015), 13th International Conference on Topics in Astroparticle and Underground Physics, TAUP 2013

[60] G. Heusser, *Low-Radioactivity Background Techniques*, Annual Review of Nuclear and Particle Science **45**, 543, URL `http://dx.doi.org/10.1146/annurev.ns.45.120195.002551` (1995)

[61] I. Abt, et al., *A New Ge^{76} Double Beta Decay Experiment at LNGS: Letter of Intent* (2004)

[62] M. Agostini, et al., GERDA, *The background in the* $0\nu\beta\beta$ *experiment GERDA*, Eur. Phys. J. **C74**, 2764 (2014)

[63] G. F. Knoll, *Radiation detection and measurement*, John Wiley & Sons (2010)

[64] M. Barnabé-Heider, *Performance and stability tests of bare high purity germanium detectors in liquid argon for the GERDA experiment*, Ph.D. thesis, Uinversität Heidelberg, URL `http://archiv.ub.uni-heidelberg.de/volltextserver/volltexte/2009/9551` (2009)

[65] G. N. Martin, et al., *Surface passivation of high purity germanium detectors using amorphous hydrogenated silicon films* URL `http://www.dtic.mil/cgi-bin/GetTRDoc?AD=ADA516274` (2008)

[66] N. Becerici-Schmidt, *Results on Neutrinoless Double Beta Decay Search in* GERDA*: Background Modeling and Limit Setting*, Ph.D. thesis, MPI Physics, Munich and TU Munich (2014)

[67] M. Agostini, et al., Gerda Collaboration, *Results on Neutrinoless Double-β Decay of Ge-76 from Phase I of the* GERDA *Experiment*, Phys. Rev. Lett. **111**, 122503, URL `http://publish.aps.org/abstract/prl/v111/p122503` (2013)

[68] M. Agostini, et al., *Pulse shape discrimination for* GERDA *Phase I data*, Eur. Phys. J. **C 73**, 2583 (2013)

[69] P. N. Luke, et al., *Low capacitance large volume shaped-field germanium detector*, IEEE Transactions on Nuclear Science **36**, 926 (1989)

[70] Z. He, *Review of the Shockley–Ramo theorem and its application in semiconductor gamma-ray detectors*, Nuclear Instruments and Methods in Physics Research Section A: Accelerators, Spectrometers, Detectors and Associated Equipment **463**, 250 , URL `http://www.sciencedirect.com/science/article/pii/S0168900201002236` (2001)

[71] M. Agostini, et al., *Production, characterization and operation of^{76}Ge enriched BEGe detectors in GERDA*, The European Physical Journal C **75**, 1, URL `http://dx.doi.org/10.1140/epjc/s10052-014-3253-0` (2015)

[72] D. Budjáš, et al., *Pulse shape discrimination studies with a Broad-Energy Germanium detector for signal identification and background suppression in the GERDA double beta decay experiment*, Journal of Instrumentation **4**, P10007, URL `http://stacks.iop.org/1748-0221/4/i=10/a=P10007` (2009)

[73] M. Agostini, et al., *Characterization of a broad energy germanium detector and application to neutrinoless double beta decay search in 76 Ge*, Journal of Instrumentation **6**, P04005, URL `http://stacks.iop.org/1748-0221/6/i=04/a=P04005` (2011)

[74] D. Budjáš, et al., *Isotopically modified Ge detectors for GERDA: from production to operation*, Journal of Instrumentation **8**, P04018, URL `http://stacks.iop.org/1748-0221/8/i=04/a=P04018` (2013)

[75] T. Goldbrunner, *Messung niedrigster Aktivitäten für das solare Neutrinoexperiment BOREXINO*, Ph.D. thesis, Technische Unversität München (1997)

[76] G. Harman, *WIRE BONDING IN MICROELECTRONICS*, McGraw-Hill Education, 3rd edition, URL `https://books.google.de/books?id=rAmJbSQ7BmEC` (2009)

[77] W. van Driel, et al., *Reliability of wirebonds in micro-electronic packages*, Microelectronics International **25**, 15, URL `http://dx.doi.org/10.1108/13565360810875967` (2008)

[78] I. Lum, et al., *Footprint study of ultrasonic wedge-bonding with aluminum wire on copper substrate*, Journal of Electronic Materials **35**, 433, URL `http://dx.doi.org/10.1007/BF02690530` (2006)

[79] B. Langenecker, *Effects of Ultrasound on Deformation Characteristics of Metals*, IEEE Trans. Sonics Ultrasonics **SU 13**, 1 (1966)

[80] R. Mindlin, *Compliance of Elastic Bodies in Contact*, ASME Trans. J. Appl. Mech. **16**, 259 (1949)

[81] US Department of Defense, *Test method standard 883J*, URL `http://www.dscc.dla.mil/downloads/milspec/docs/mil-std-883/std883.pdf` (2015)

[82] Z. Lai, et al., *The Nordic Electronics Packaging Guideline Chapter A2*, URL `http://extra.ivf.se/ngl/` (2000)

[83] B. Majorovits, et al., *Aluminum as a source of background in low background experiments*, Nuclear Instruments and Methods in Physics Research Section A: Accelerators, Spectrometers, Detectors and Associated Equipment **647**, 39 , URL `http://www.sciencedirect.com/science/article/pii/S0168900211009533` (2011)

[84] S. Nisi, et al., *Comparison of inductively coupled mass spectrometry and ultra low-level gamma-ray spectroscopy for ultra low background material selection*, Applied Radiation and Isotopes **67**, 828 , URL `http://www.sciencedirect.com/science/article/pii/S0969804309000475` (2009), 5th International Conference on Radionuclide Metrology - Low-Level Radioactivity Measurement Techniques ICRM-LLRMT'08

[85] C. Deshpandey, et al., *II-2 - Evaporation Processes*, in J. L. V. KERN (editor), *Thin Film Processes*, 79 – 132, Academic Press, San Diego, URL `http://www.sciencedirect.com/science/article/pii/B9780080524214500071` (1991)

[86] R. F. Bunshah, *Handbook of deposition technologies for films and coatings*, Materials science and process technology series, Noyes, Westwood, NJ, 2nd edition (1994)

[87] G. McGuire, *Semiconductor Materials and Process Technology Handbook*, William Andrew Publishing/Noyes, URL `http://app.knovel.com/hotlink/toc/id:kpSMPTH001/semiconductor-materials/semiconductor-materials` (1988)

[88] Ionbeam Scientific, URL `http://www.ionbeam.co.uk/ion_beam_pre-cleaning.php` (2016)

[89] L. Cassina, et al., *GeFRO: A New Charge Sensitive Amplifier Design for Wide Bandwidth and Closed-Loop Stability Over Long Distances*, Nuclear Science, IEEE Transactions on **61**, 1259 (2014)

[90] S. Riboldi, et al., *Improvement of the "CC2" charge sensitive preamplifier for the GERDA phase II experiment*, in *Proceedings, 2012 IEEE Nuclear Science Symposium and Medical Imaging Conference (NSS/MIC 2012): Anaheim, California, USA, October 29-November 3, 2012*, 782–785 (2012)

[91] S. Riboldi, Private Communication (2016)

[92] C. Cattadori, *Selected Topics on FE Electronics for the GERDA Phase II Ge detector readout*, Presentation at LRT 2015, URL `https://www.npl.washington.edu/indico/getFile.py/access?contribId=20&sessionId=2&resId=0&materialId=slides&confId=5` (2015)

[93] M. Agostini, et al., *Improvement of the energy resolution via an optimized digital signal processing in GERDA Phase I*, The Eur. Phys. J. C 255 **75**, URL `http://dx.doi.org/10.1140/epjc/s10052-015-3409-6` (2015)

[94] P. Barton, et al., *Low-noise low-mass front end electronics for low-background physics experiments using germanium detectors*, in *Nuclear Science Symposium and Medical Imaging Conference (NSS/MIC), 2011 IEEE*, 1976–1979 (2011)

[95] A. H. Clark, *Electrical and Optical Properties of Amorphous Germanium*, Phys. Rev. **154**, 750, URL `http://link.aps.org/doi/10.1103/PhysRev.154.750` (1967)

[96] C. Feldman, et al., *Amorphous Semiconductors*, APL Technical Digest **7** (1968)

[97] K. L. Chopra, et al., *Structural, Electrical, and Optical Properties of Amorphous Germanium Films*, Phys. Rev. B **1**, 2545, URL `http://link.aps.org/doi/10.1103/PhysRevB.1.2545` (1970)

[98] H. R. Kaufman, et al., *Ion source design for industrial applications*, AIAA Journal **20**, 745 (1982)

[99] M. Keller, *Development of ultra-low background electronic components for the neutrinoless double beta decay experiment* GERDA, Master's thesis, Technische Universität München (2014)

[100] M. Boswell, et al., *MaGe-a Geant4-Based Monte Carlo Application Framework for Low-Background Germanium Experiments*, IEEE Transactions on Nuclear Science **58**, 1212 (2011)

[101] V. D'Andrea, et al., *Energy resolution of commissioning*, gERDA collaboration meeting presentations (2015)

[102] P. Zavarise, et al., *Off-line data quality monitoring for the GERDA experiment*, Journal of Physics: Conference Series **375**, 042028, URL `http://stacks.iop.org/1742-6596/375/i=4/a=042028` (2012)

[103] M. Agostini, *Signal and background studies for the search of neutrinoless double beta decay in* GERDA, Ph.D. thesis, Technische Unversität München, URL `http://www.mpi-hd.mpg.de/ge76/public/2013/phd2013_matteoAgostini.pdf` (2013)

[104] D. Budjas, et al., *Pulse shape discrimination studies with a Broad-Energy Germanium detector for signal identification and background suppression in the* GERDA *double β decay experiment*, J. Instrum. **4**, p10007 (2009)

[105] M. Agostini, et al., *Progress report to the LNGS scientific committee* (2016)

[106] M. Agostini, et al., *Limits on uranium and thorium bulk content in GERDA Phase I detectors*, in preparation (2016)

Danksagungen

Many people were directly or less directly involved that I could start and finish this thesis. First of all I would like to thank my supervisor Prof. Stefan Schönert who got me working in the field of $0\nu\beta\beta$ and gave me the interesting, and sometimes daunting task, to work directly with and on these very expensive items. Personally, I did not break one of them! I also would like to thank Dr. Bela Majorovits for being, from the start, very interested in and supportive of the possibility to bond directly on the detectors. In the beginning (and also later), I got a lot of advice about metallization and bonding from the cryo group (especially Sabine Roth, Mike Willers and Achim Gütlein) at TUM. For all things analytical and coding I owe a lot to Matteo Agostini, Andrea Lazzaro and Andi Zöller. Der E15 Werkstatt danke ich dafür, dass sie viele last-minute Teile schnell und rechtzeitig fertig machten, wenn ich mal wieder schnell nach Olen oder ans Gran Sasso musste. Thanks to all the E15 chair for a great time! The entire detector mounting and testing was of course a big team effort, so thanks to the whole integration team, especially Konstantin Gusev. Driving million euro detectors around Belgium was fun with Christoph Wiesinger. My girlfriend Andrea Wüst I want to thank for patience and love when I was once again called on a short notice to come/go to LNGS or Olen.